Modelling Photospheric Magnetoconvection

Sean Mark Blanchflower

Trinity College, Cambridge

Dissertation submitted for the degree of

Doctor of Philosophy

at the

University of Cambridge

December, 1999

Modelling Photospheric Magnetoconvection

Sean Blanchflower

Recent observations of the solar photosphere have shown a wide range of magnetic phenomena; plages, faculae, pores, flares, and sunspots all owe their existence to the turbulent solar magnetic field. Any understanding of this our local star will include a full comprehension of the behaviour of a conducting fluid in the presence of a magnetic field.

My studies have concentrated on an investigation of magnetoconvection in two and three spatial dimensions. I began with fully compressible two-dimensional convection, exposing the full range of convective patterns that may be obtained through varying the field strength, diffusivities, and box size. A key observation was that if the aspect ratio of the experimental domain is too narrow then the solution may not be representative of the choice of parameters. Further study looked at how solutions were altered by changing the imposed boundary conditions and through imposing a range of temperature and magnetic boundary conditions.

The discovery of a new convective pattern consisting of a single large wavelength plume motivated further studies. In this 'flux-separated' state, flow is confined to an essentially field-free region whilst the remainder of the box contains strong, almost vertical magnetic field in which all convection is suppressed. Further experiments in a simplified model allowed an extra class of solutions to be found. A crucial new symmetry breaking gave rise to a fundamental single roll solution (a *convecton*), as opposed to the usual pair of rolls. Attempts were made to derive related 'low-order' models, simple enough to allow detailed analysis of the mechanisms that permit localization.

Finally, the extension to three spatial dimensions was made, and dynamic isolated patterns were located, with important consequences for studies of localized solutions and solar observations.

Preface

All of the work described in this dissertation is believed to be original, and the work is entirely my own except where explicit reference is made to other authors.

S Blanchflower

Acknowledgements

The daunting task of forming and undertaking a project whilst a research student is impossible without the experience and knowledge of the supervisor. First of all I must therefore express my gratitude to Professor Nigel Weiss for his constant guidance and incomparable insight. It has been a privilege to work along side him throughout my three years and I can only hope that this dissertation is a fitting testament to his efforts. My thanks also go to Alastair Rucklidge for invaluable assistance with technical matters and to Mike Proctor for a wide range of helpful suggestions. As ever, my many computing difficulties were patiently resolved with the help of Derek Brownjohn and Paul Bolchover.

The dissertation was typeset using several TEX macros written by Alastair Rucklidge, and many of the key figures were produced using the graphics and drawing packages IDL. I am grateful to the Department of Applied Mathematics and Theoretical Physics and to Trinity College, Cambridge for financial assistance in attending conferences. And finally, none of this would have been possible without the funding that I have received from PPARC.

Table of Contents

To all the people who have made my time in Cambridge so enjoyable

Chapter 1.

Introduction

The Sun is a mass of fiery stone, a little larger than Greece.

Anaxagoras 434 BC

Magnetic fields play an enormous role in all areas of astrophysics. There are very few aspects of our ever expanding subject that can safely neglect the effects of magnetism in one form or another, be it small scale - as in models of the geodynamo - or galactic - in studies of the largest quasars. It is generally believed that most stars possess a magnetic field of some size, a claim supported by the studies of Wilson (1978). In particular, in late-type stars such as our Sun the outer regions are fully convective, due to the ionization of hydrogen, and there is an important interaction between the field and the convective transport that gives rise to various magnetic phenomena. It is only on the Sun that the details of such activity may be resolved.

The study of these phenomena began primarily in the 17th Century when the newly invented telescope allowed Fabricius, Scheiner and Galileo to make detailed observations of sunspots. Later investigations of sunspot data led Schwabe to propose the existence of the eleven year solar cycle in 1843, but the modern era of solar physics began with Hale's confirmation in 1908 that sunspots contain a strong magnetic field. Although the existence of a solar magnetic field had been conjectured previously, this discovery of the first extra-terrestrial magnetic field effectively created the new science of magnetoconvection. Since then, the increases in telescope power and refined techniques have led to countless important observational discoveries.

§1.1. Magnetic features of the photosphere

The Sun's magnetic field is believed to be generated by dynamo action at the base of the convection zone. At the surface, this magnetic field is seen in various forms. In the photosphere, the strongest fields are found in pores and sunspots. Pores are dark regions with diameters between 2 and 7Mm and fields of around $2000G$ that are formed when sufficient magnetic flux accumulates in one region of the photosphere. If the total flux exceeds a critical value of around 7TWb then the pore develops a penumbra and becomes a sunspot. In actual fact spots can exist even when the total magnetic field drops to only 2TWb (Rucklidge *et al.* 1995).

In a sunspot the magnetic field inhibits upward convection leading to an apparently darker region of between 3.6Mm and 20Mm in diameter. Spots consist of a well defined central region, or umbra, which is fairly uniformly dark, and a surrounding penumbra with characteristic filamentary features (Figure 1-1). The umbra contains a strong vertical field of up to $3000G$ which remains practically uniform. Umbral features include *light bridges*, which are lanes of bright material that span the umbra and may last for several days. These are areas of reduced field strength and vigorous convection resisting the pressure of the surrounding umbral magnetic field. Granules within a bridge have been shown to be associated with upward motion, and to vary in a manner consistent with oscillatory convection (Rimmele 1997). High resolution observations show that umbrae also contain convective features in the form of *umbral dots* (Danielson 1964). These small spots with brightness comparable to that of the photosphere are observed in all sunspots, although many of the larger spots contain regions (dark nuclei) in which umbral dots are not seen. Recent observations (Sobotka 1997; Sobotka, Brandt & Simon 1997a,b) demonstrate that these features bear no characteristic diameter or lifetime, and that their number increases with decreasing size. A typical dot has diameter 300km and is visible for around 14 minutes, though some last for over 2 hours. They are associated with magnetic fields that are up to 20% smaller than the surrounding umbra, and drift slowly inwards. A distinction is made between such *central* umbral dots and *peripheral* umbral dots which are bright features that have encroached into the umbra from the surrounding penumbra (Sobotka *et al.* 1995).

Elsewhere in the photosphere, magnetograms show that fields are not distributed smoothly but form an irregular pattern of discrete magnetic elements, or flux tubes, that accumulate at nodes between neighbouring granules. This pattern, seen most effectively in the CH G-band, is called the *magnetic network* and extends over the whole solar disk. Typical magnetic elements have diameters up to $1000km$ and fields of around $1 - 2kG$ (Muller 1994).

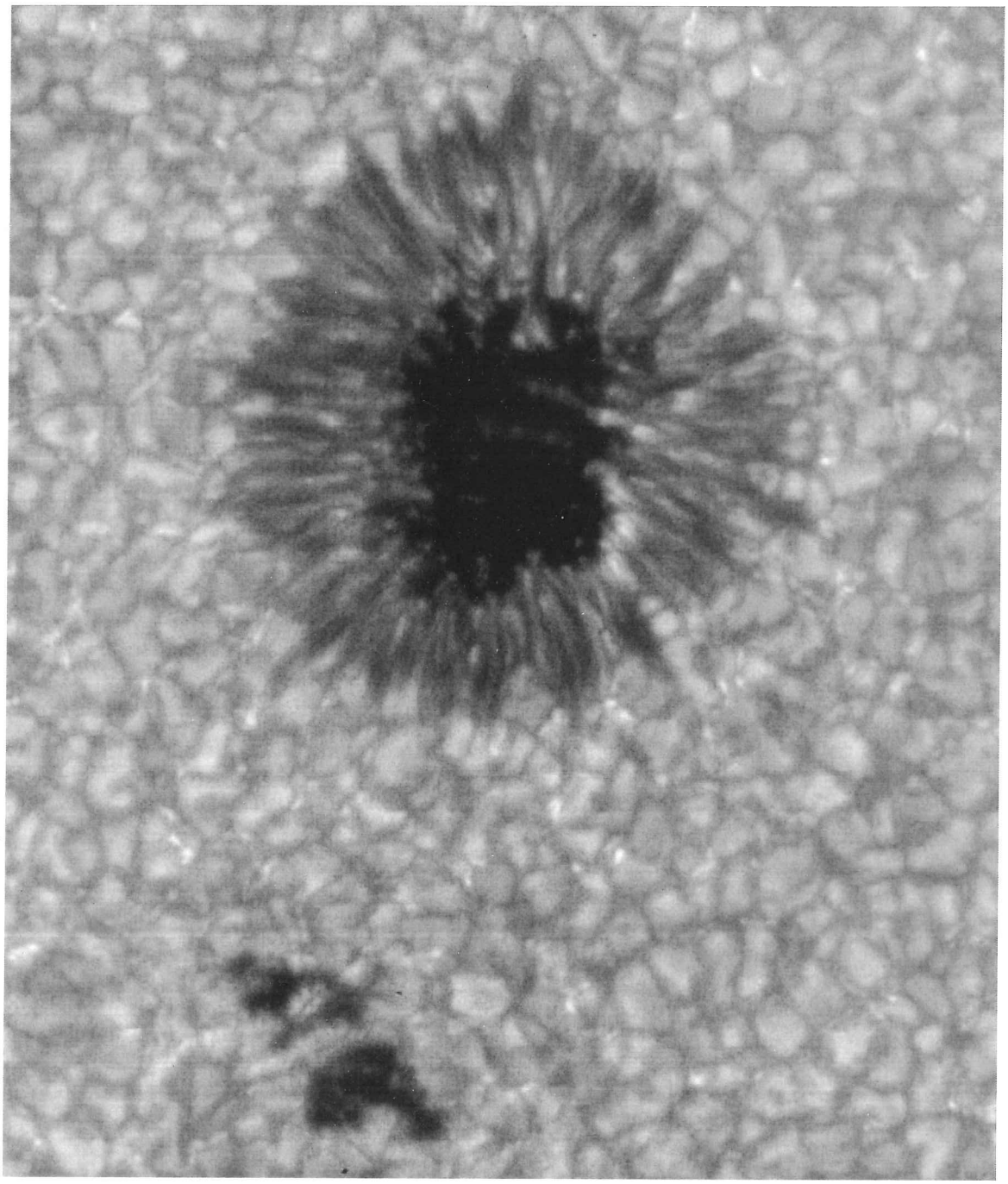

Figure 1-1. *A sunspot showing a clearly defined umbra and penumbra. Also shown is solar granulation and, towards the bottom of the frame, several pores. (Brandt, Simon, Scharmer, & Shine; Kiepenheuer/ Uppsala/ Lockheed)*

When seen in CaII K emission, much of the sun appears to be covered in bright strips or *plages*. These are regions where photospheric magnetic fields extend into the overlying chromosphere. They are characterized by abnormal granulation, and correspond to convection on a smaller horizontal scale.

§1.2. *Magnetoconvection*

In the early part of this century, remarkable advances in observations of solar magnetic phenomena gave the motivation for theoretical studies of magnetohydrodynamics. The subject effectively began with the celebrated correspondence between Thomas Cowling and Ludwig Biermann in the 1930s, when they first discussed the inhibition of convection in sunspots. In the 1940s, further advances were made by Alfvén and Walén, but attempts to create theoretical models of magnetoconvection have their origins with Chandrasekhar (1961) and his treatment of the linear Boussinesq equations. The bifurcation structure has been studied in great detail using weakly nonlinear theory (Veronis 1959; Jones *et al.* 1990), but advances beyond the initial bifurcations required numerical experiments. Investigations into the nonlinear regime began with further use of Boussinesq magnetoconvection (Proctor and Weiss 1982; Cattaneo 1994). Some three-dimensional studies of the anelastic approximation were carried out (Nordlund 1984), but the dramatic increase in computing power has allowed investigations to concentrate on fully compressible convection both in two and three spatial dimensions.

Within the attempts to model the interaction of convection and magnetic fields in the solar photosphere there are two very different styles of research. The first method attempts to simulate the stellar atmosphere in as much detail as possible, pioneered by Nordlund (1984). Effects such as ionization and radiative transport are included, and such investigations have proved extremely successful in modelling photospheric behaviour such as the formation of the magnetic network (Nordlund & Stein 1989), or the evolution of single flux elements (Steiner *et al.* 1996, 1998). The second approach is to construct more idealized models and to follow the effects of varying important parameters in order to isolate certain physical processes. In this way investigations have revealed which types of behaviour may be obtained in particular frameworks, first in a two-dimensional geometry (Hurlburt & Toomre 1988, Weiss *et al.* 1990) and later in three dimensions (Weiss *et al.* 1996). It is this second method that we follow here.

However, these idealized models have so far failed to show various types of behaviour that are observed in the solar photosphere, such as the range of scales of convection observed in umbral dots. It is possible that this disparity is caused

When seen in CaII K emission, much of the sun appears to be covered in bright strips or *plages*. These are regions where photospheric magnetic fields extend into the overlying chromosphere. They are characterized by abnormal granulation, and correspond to convection on a smaller horizontal scale.

§1.2. *Magnetoconvection*

In the early part of this century, remarkable advances in observations of solar magnetic phenomena gave the motivation for theoretical studies of magnetohydrodynamics. The subject effectively began with the celebrated correspondence between Thomas Cowling and Ludwig Biermann in the 1930s, when they first discussed the inhibition of convection in sunspots. In the 1940s, further advances were made by Alfvén and Walén, but attempts to create theoretical models of magnetoconvection have their origins with Chandrasekhar (1961) and his treatment of the linear Boussinesq equations. The bifurcation structure has been studied in great detail using weakly nonlinear theory (Veronis 1959; Jones *et al.* 1990), but advances beyond the initial bifurcations required numerical experiments. Investigations into the nonlinear regime began with further use of Boussinesq magnetoconvection (Proctor and Weiss 1982; Cattaneo 1994). Some three-dimensional studies of the anelastic approximation were carried out (Nordlund 1984), but the dramatic increase in computing power has allowed investigations to concentrate on fully compressible convection both in two and three spatial dimensions.

Within the attempts to model the interaction of convection and magnetic fields in the solar photosphere there are two very different styles of research. The first method attempts to simulate the stellar atmosphere in as much detail as possible, pioneered by Nordlund (1984). Effects such as ionization and radiative transport are included, and such investigations have proved extremely successful in modelling photospheric behaviour such as the formation of the magnetic network (Nordlund & Stein 1989), or the evolution of single flux elements (Steiner *et al.* 1996, 1998). The second approach is to construct more idealized models and to follow the effects of varying important parameters in order to isolate certain physical processes. In this way investigations have revealed which types of behaviour may be obtained in particular frameworks, first in a two-dimensional geometry (Hurlburt & Toomre 1988, Weiss *et al.* 1990) and later in three dimensions (Weiss *et al.* 1996). It is this second method that we follow here.

However, these idealized models have so far failed to show various types of behaviour that are observed in the solar photosphere, such as the range of scales of convection observed in umbral dots. It is possible that this disparity is caused

by the restrictive nature of the model. It has been shown (Weiss *et al.* 1996) that the pattern of convection may be changed dramatically if the width of the computational box is too small, and that a wider box may be required to allow the true behaviour to occur. Similarly, in such idealized models the temperature is held fixed and the magnetic field is constrained to be vertical on both the lower and upper boundaries. These and other boundary conditions are clearly unphysical and it is important to investigate the effects that more realistic boundary conditions would have, to assist in validating the many assumptions of previous studies in this area.

In order to do this, a systematic investigation is needed in which many different key parameters are varied. This requires a large number of numerical experiments to be performed and is thus computationally expensive. The use of three spatial dimensions is thus rendered impossible and calculations are restricted to two dimensions.

The aim of my dissertation is to gain an understanding of the different effects and processes that lead to the different types of observed behaviour and the nature of the bifurcations that cause them. Moreover it is vital to know exactly how restrictive such idealized models are. I thus investigate several points:

- What effect does the size of the computational box (the aspect ratio, λ) have on the resulting flow?
- How wide should the computational domain be to obtain flow that is fully representative of the chosen parameter values?
- What patterns of convection may be obtained for different values of the magnetic field strength?
- How is the flow altered by including some of the effects of radiative transfer and allowing the surface temperature to vary?
- What effect does matching the field to a force-free (or perhaps potential) field have?

§1.2.1. *Isolated states*

In some spatially extended systems the experimental region may be divided into two distinct domains; an isolated pattern occurs in a small region of the spatially homogeneous system, whilst the remainder usually contains an approximation to the trivial or basic state. Such localized solutions are associated with bistability. Stable examples of such localized states have been seen in a variety of physical and

theoretical frameworks (Riecke 1998). Particular study has been given to convection in binary-fluid mixtures in which isolated regions of travelling waves have been observed both experimentally (Niemela *et al.* 1991) and theoretically (Thual & Fauve 1988). Similarly, solitary waves have been found in such diverse areas as cellular flames (Bayliss *et al.* 1994), optical fibres (Mollenauer *et al.* 1980) and chemical reactions (Rotermund *et al.* 1991). More recently, pairs of isolated vortices have been seen in Taylor-Couette flow (Groisman & Steinberg 1997), and in trays of small ball-bearings single standing waves ('oscillons') may be observed when vertical oscillation of the system induces the Faraday instability (Umbanhowar *et al.* 1996). The phenomenon has also been investigated using low order amplitude equations and isolated structures have been found in cases such as Swift-Hohenberg and reaction-diffusion systems (Sakaguchi & Brand 1998, Or-Guil *et al.* 1998). In each of the above examples it is believed that a necessary though certainly not sufficient condition for localization is the bistability of the trivial and nonlinear states. There are examples of isolated waves in which the bifurcation to the extended waves is supercritical, for example in nematic electroconvection (Dennin *et al.* 1998, Riecke & Granzow 1998), but these form a separate topic of study. There are also surprisingly few examples of such localized states being observed in two or three dimensions, as opposed to the usual single spatial dimension.

For the case of magnetoconvection isolated states occur as the result of flux expulsion (Weiss 1966). This tends to create regions in which the magnetic field is separated from the fluid flow, and under certain circumstances isolated convective states have been observed (Blanchflower *et al.* 1998, Galloway & Weiss 1981, Weiss 1981).

Weiss (1981) considered a two-dimensional rectangular box under the Boussinesq approximation. The flow of a conducting fluid was modelled in the presence of a vertical magnetic field. A mirror symmetry was imposed upon the system with the effect that all solutions were symmetric under the actions of the group Z_2, reflections in a single plane. Galloway & Weiss (1981) considered a similar system, and examined behaviour in boxes with aspect ratio ≤ 4, again with an imposed mirror symmetry on the system. Both located states in which a small convective cell was able to remove all flux and collect it into a region at its edges in accordance with the effects of flux expulsion.

In Chapter 2 I present the results of my studies of a fully-compressible conducting fluid in the presence of a vertical magnetic field. I discuss how the solutions depend on the width of the computational domain, and show that in wide boxes (an aspect ratio greater than approximately 4) a new type of behaviour is seen. A

single large convective plume is formed which occupies about half of the box, this region containing essentially no magnetic field. The remainder of the box consists of strong vertical magnetic field, strong enough that it suppresses all convection within that region. This new 'flux-separated' state raises many new questions, and following on from these results I attempt to discover the nature of such states, and under what circumstances the flow is able to create two such different regimes.

Due to the complicated nature of the full nonlinear equations of compressible magnetoconvection, any attempt to analyse a particular phenomenon should first consider a system in which many of the less essential aspects have been simplified. In Chapter 3 I thus derive a new model in which the modes are truncated in the vertical direction. This reduction in complexity allows the full range of convective patterns to be studied in much greater detail, and many such flux-separated states are located. In addition, a fundamental new type of convection is found. As with other such flux-separated states the majority of the box remains in the basic state of strong, almost vertical magnetic field in which all convection is suppressed; however, a small region is formed in which the flow is able to expel virtually all the flux, creating an isolated island consisting of a single narrow convective roll (a 'convecton'). This state can exist in a box of arbitrary width, or several of them may coexist independently of one another, scattered across the box. A similar solution is then reproduced for the case of fully-resolved Boussinesq magnetoconvection. This is the first time such an isolated state has been observed. Unlike the cases listed above in which isolated states were found either experimentally or in carefully chosen models, here such a state is located numerically for the full physical partial differential equations of magnetohydrodynamics.

However, even the system of five partial differential equations derived in Chapter 3 is too complicated to examine analytically. With this in mind, Chapter 4 reports attempts to reduce the order of the system even further by deriving a overly simplified set of equations from the full equations of magnetohydrodynamics. In this way, both a Swift-Hohenberg (Swift & Hohenberg 1977) and an asymptotically correct model are examined and preliminary results are presented.

The discovery of a range of localized solutions in two-dimensional magnetoconvection raises the important question of whether such states could be found with the addition of the third spatial dimension, and indeed what forms they would take. In Chapter 5 the equations of mhd are again truncated vertically, and solved in wide boxes under a variety of circumstances. Various different isolated states are found, with preference given to a spherical analogue to the convecton, which both pulses and rotates. Such a solution has important implications for studies of the

solar photosphere, particularly with respect to umbral dots – small, isolated bright features observed in the region of high magnetic field strength in the centre of the majority of sunspots.

Chapter 2.

Compressible Magnetoconvection

Many previous studies have investigated compressible magnetoconvection in an idealized rectangular box heated from below (Hurlburt & Toomre 1988; Weiss *et al.* 1990; Weiss *et al.* 1996). In order to concentrate on the basic patterns that are obtained under certain circumstances, these studies used comparatively unphysical boundary conditions: the temperature was held fixed and the magnetic field was constrained to be vertical at the surface and base, and experiments were conducted in fairly narrow boxes. In this chapter, I investigate the restrictions that these conditions place on the system by conducting a thorough study of the range of convective patterns that may be obtained in two-dimensional compressible magnetoconvection. Many of the results are also presented in Blanchflower, Rucklidge & Weiss (1998).

§2.1. *The model problem*

I follow the basic configuration that has already been used in both two-dimensional (Hurlburt & Toomre 1988; Weiss *et al.* 1990) and three-dimensional (Weiss *et al.* 1996) investigations. Accordingly, I use cartesian co-ordinates with the z-axis pointing downwards, and assume that the velocity $\mathbf{u}$ and the magnetic field $\mathbf{B}$ are two-dimensional, lying in the (x, z)-plane, and are independent of y. Consider a perfect monatomic gas occupying the rectangular region $\{0 \leq x \leq \lambda;\ z_0 \leq z \leq z_0 + 1\}$, where the coordinates have been scaled by the depth of the layer, d. The gas is electrically conducting and contains a magnetic field with a mean flux density corresponding to a uniform vertical field $\mathbf{B_0}$.

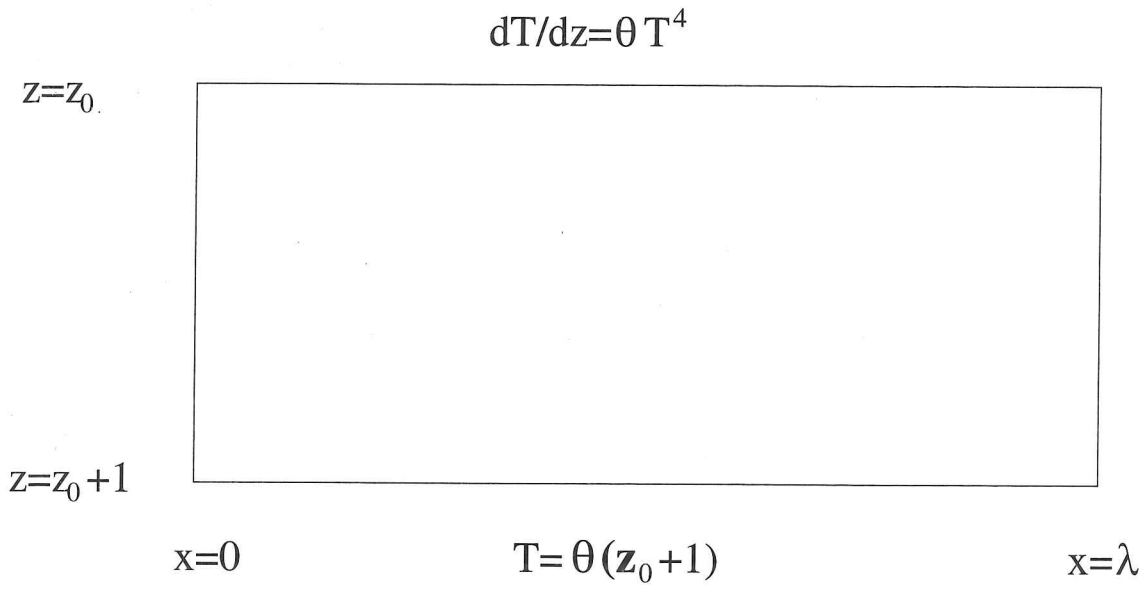

Figure 2-1. *The model problem, showing the computational box and the thermal boundary conditions.*

§2.1.1. The background atmosphere

In the absence of any motion there is a uniformly stratified equilibrium solution corresponding to a polytrope with index m, for which the temperature T and the density ρ are given by $T = \theta z$ and $\rho = (\theta z)^m$, where $\theta = 1/z_0$. The superadiabatic gradient is given by

$$(\nabla - \nabla_{ad}) = \frac{1}{(m+1)} - \frac{\gamma - 1}{\gamma}, \tag{2.1}$$

where $\gamma = 5/3$, the ratio of specific heats. This stratification is superadiabatic if $m < 1/(\gamma - 1)$.

Again following the formalism of Weiss *et al.* (1990), the thermal conductivity K, the electrical conductivity $(\mu_0 \eta)^{-1}$, the shear viscosity μ, the magnetic permeability μ_0, and the heat capacity c_p are all held constant. Thus the magnetic diffusivity η is also constant but both the thermal diffusivity $\kappa = K/c_p\rho$ and the viscous diffusivity $\nu = \mu/\rho$ vary as ρ^{-1} and thus with depth. The Prandtl number $\sigma \equiv \nu/\kappa$ remains constant but the ratio of magnetic to thermal diffusivities $\zeta(z) \equiv \eta/\kappa = \zeta_0 \rho(z)$.

§2.1.2. The equations of magnetoconvection

The equations are cast into dimensionless form, scaling time by the reduced acoustic travel time $1/\sqrt{\mathcal{R}\Delta T}$, and introducing the dimensionless thermal conductivity $\bar{K}$, and the square of the ratio of the Alfvén speed to the reduced sound speed F, where

$$\bar{K} = K/c_p \rho_0 d\sqrt{\mathcal{R}\Delta T}\ ,\ F = B_0^2/(\mu_0 \rho_0 \mathcal{R}\Delta T). \tag{2.2}$$

The equations of magnetoconvection are thus as follows

$$P = \rho T, \quad \frac{\partial \rho}{\partial t} = -\nabla \cdot (\rho \mathbf{u}), \tag{2.3}$$

$$\nabla \cdot \mathbf{B} = 0, \quad \frac{\partial \mathbf{B}}{\partial t} = \nabla \times (\mathbf{u} \times \mathbf{B} - \zeta_0 \bar{K} \nabla \times \mathbf{B}), \tag{2.4}$$

$$\frac{\partial}{\partial t}(\rho \mathbf{u}) = -\nabla \cdot (\rho \mathbf{u}\mathbf{u} - F\mathbf{B}\mathbf{B}) - \nabla(P + \tfrac{1}{2}F|\mathbf{B}|^2) + (m+1)\rho \hat{\mathbf{z}} + \nabla \cdot \tau, \tag{2.5}$$

$$\frac{\partial T}{\partial t} = -\mathbf{u} \cdot \nabla T - (\gamma - 1) T \nabla \cdot \mathbf{u} + \frac{\gamma \bar{K}}{\rho} \nabla^2 T + \frac{(\gamma - 1)\bar{K}}{\rho} \left(\frac{\tau \cdot \tau}{2\sigma} + F\zeta_0 |\nabla \times \mathbf{B}|^2 \right), \tag{2.6}$$

in the region $\{0 \le x \le \lambda;\ z_0 \le z \le z_0 + 1\}$. Here $\mathbf{u}$ is the velocity and the viscous stress tensor is defined by

$$\tau_{ij} = \sigma \bar{K} \left(\frac{\partial u_i}{\partial x_j} + \frac{\partial u_j}{\partial x_i} - \frac{2}{3} \delta_{ij} \frac{\partial u_k}{\partial x_k} \right). \tag{2.7}$$

§2.1.3. Boundary conditions

The above equations are to be solved subject to appropriate boundary conditions. The lateral boundaries are straightforward: all quantities are constrained to be periodic in x with period λ, so that $T(0, z, t) = T(\lambda, z, t)$ etc. At the top and bottom of the layer there are assumed to be impermeable but slippery boundaries, on which both the normal component of the velocity and the tangential component of the viscous stress both vanish. Thus

$$u_z = \partial u_x / \partial z = 0 \quad \text{at } z = z_0,\ z_0 + 1. \tag{2.8}$$

The standard idealized boundary conditions for $\mathbf{B}$ and T require the magnetic field to be vertical and the temperature to remain constant, so that

$$B_x = \partial B_z / \partial z = 0, \quad T = z_0 + 1 \quad \text{at } z = z_0 + 1, \tag{2.9}$$

and

$$B_x = \partial B_z / \partial z = 0, \quad T = z_0 \quad \text{at } z = z_0. \tag{2.10}$$

A more realistic alternative is to match the field at the upper boundary to a potential field in the half-space $z < z_0$. If the field components are expanded in Fourier series as

$$\begin{aligned} B_x(x,z,t) &= \sum_{-M}^{M} \hat{B}_{x,m}(z,t) \exp(2\pi i m x/\lambda), \\ B_z(x,z,t) &= \sum_{-M}^{M} \hat{B}_{z,m}(z,t) \exp(2\pi i m x/\lambda), \end{aligned} \tag{2.11}$$

with $\hat{B}_{x,-m} = \hat{B}^*_{x,m}$, $\hat{B}_{z,-m} = \hat{B}^*_{z,m}$, $\hat{B}_{x,0} = 0$, $\hat{B}_{z,0} = 1$, then

$$\hat{B}_{x,m}(z_0,t) = \mathrm{i}(m/|m|)\hat{B}_{z,m}(z_0,t) \qquad (m \neq 0) \tag{2.12}$$

and, since $\mathbf{B}$ is solenoidal,

$$\frac{\partial \hat{B}_{z,m}}{\partial z} = -\frac{2\pi \mathrm{i} m}{\lambda}\hat{B}_{x,m} = \frac{2\pi m^2}{\lambda |m|}\hat{B}_{z,m} \qquad (m \neq 0) \tag{2.13}$$

at $z = z_0$.

It is also appropriate to relax the thermal constraints by allowing a variable temperature $T(x, z_0, t)$ on the upper boundary. This may be achieved by matching the heat conducted to the boundary to black-body radiation from the surface so that, in dimensional terms, $K\partial T/\partial z = \bar{\sigma}T^4$, where K is the (uniform) thermal conductivity and $\bar{\sigma}$ is Stefan's constant. In our formulation, the ratio $\bar{\sigma}/K$ is determined by requiring that the static polytropic atmosphere should be in thermal equilibrium, whence it follows that

$$\partial T/\partial z = \theta T^{\,4} \quad \text{at } z = z_0. \tag{2.14}$$

The numerical experiments described in §2.2 and §2.3 below were all carried out with the 'realistic' boundary conditions (2.12)–(2.14) at the upper boundary, while retaining the idealized boundary conditions (2.9) at the base of the layer. In §2.4 however, these results are compared to solutions obtained using different combinations of the boundary conditions.

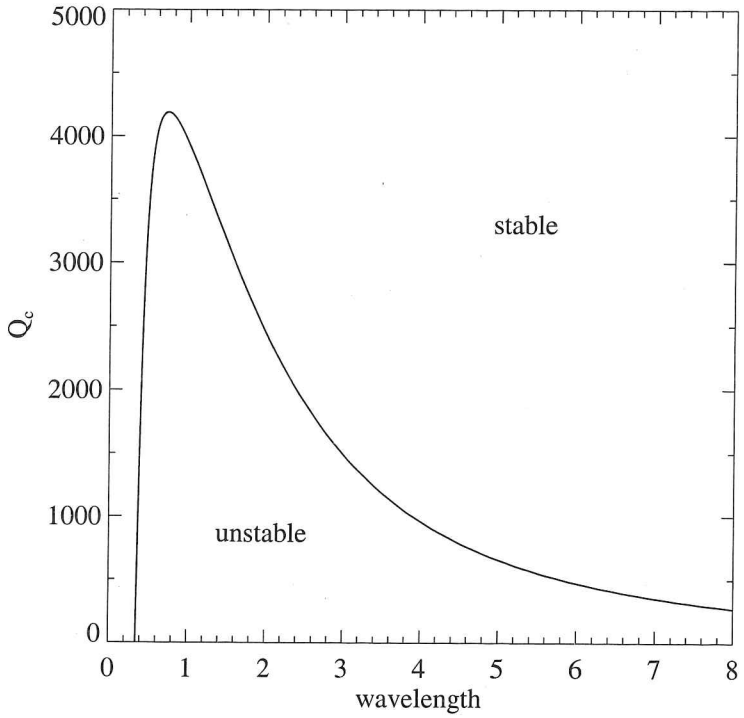

Figure 2-2. *Linear stability: the critical Chandrasekhar number Q_c as a function of the wavelength $\bar{\lambda}$. $\hat{R} = 100\,000$. From Blanchflower et al. (1998).*

§2.1.4. The model framework

For the calculations in this thesis I adopt the standard 'deep layer' model with the polytropic reference atmosphere that has been used in various previous studies (Hurlburt, Toomre & Massaguer 1984; Hurlburt & Toomre 1988; Weiss *et al.* 1990, 1996; Cattaneo *et al.* 1991; Brummell, Hurlburt & Toomre 1996) and setting $m = 1$, $\theta = 10$ (so that the density and the temperature increase by a factor of 11 across the layer) and $\gamma = \frac{5}{3}$, as for a monatomic gas. In addition, the Prandtl number (ratio of viscous to thermal diffusivity) is held fixed at $\sigma = 1$. The ratio ζ of the magnetic to thermal diffusivity is a crucial parameter, as it determines whether convection sets in at an oscillatory or a stationary bifurcation when $Q \gg 1$. Although $\zeta \ll 1$ is appropriate in the photosphere of cool stars, the ionization of hydrogen increases the opacity and reduces the thermal diffusivity, so that $\zeta > 1$ at depths below 2000 km in the Sun. Since $\zeta \propto \rho$ in our model (with both the thermal and electrical conductivities constant) and $\rho(z)$ increases with depth in our reference atmosphere, the corresponding value of the diffusivity ratio $\zeta(z) = \zeta_0 \rho(z)$. To mimic the variation of density in the Sun I set $\zeta_0 = 0.2$, so that $0.2 \leq \zeta(z) \leq 2.2$ and the value at the midpoint is $\hat{\zeta} = \zeta(z_0 + \frac{1}{2}) = 1.2$.

Throughout this study I employ two important dimensionless parameters.

Firstly the Rayleigh number

$$R(z) \equiv (m+1)^2(\nabla - \nabla_{ad})\frac{z^{2m-1}}{\sigma \bar{K}^2 {z_0}^{2m}} \tag{2.15}$$

which measures the superadiabatic temperature gradient. It is standardly referred to by its midpoint value $\hat{R} = R(z_0 + \frac{1}{2})$. Throughout this chapter the Rayleigh number is held fixed at $\hat{R} = 100\,000$ (cf. Weiss *et al.* 1996). Secondly the strength of the imposed magnetic field may be measured by either the Chandrasekhar number,

$$Q \equiv F/\sigma\zeta_0\bar{K}^2 = \frac{5}{24}F\hat{R}, \tag{2.16}$$

or $\beta(z)$, the ratio of the gas pressure to the magnetic pressure in the reference atmosphere. With these parameter values, $\beta(z) = 5\times10^6(z^2/12Q)$ and its midpoint value $\hat{\beta} = \beta(z_0+\frac{1}{2}) = 1.5\times10^5/Q$. I shall only consider a regime in which $Q \leq 5000$ or $\hat{\beta} \geq 30$, thus limiting the effects of compressibility.

§2.1.5. Linear theory

For the general compressible case, used here, linear theory is too complicated to give a detailed analysis. For a full treatment of linear theory for fully compressible magnetoconvection see Cattaneo (1984).

It may be shown that, in the absence of any magnetic field, the reference atmosphere will be stable to perturbations with wavelength $\bar{\lambda}$ if $\bar{\lambda}$ is either very large or very small. Therefore, for fixed R, convective instability occurs only for $\lambda_1 < \bar{\lambda} < \lambda_2$, where λ_1 and λ_2 are constants that may be determined numerically. When Q is very large, convection will be completely suppressed, but as Q is reduced there will be a critical value $Q_c(\bar{\lambda})$, for $\lambda_1 < \bar{\lambda} < \lambda_2$, at which the atmosphere becomes unstable. For the choice of parameters given in §2.1.4, instability will set in at a supercritical pitchfork bifurcation, followed by steady overturning convection. Figure 2-2 shows Q_c as a function of $\bar{\lambda}$ for the linearized equations with the idealized boundary conditions (2.8)–(2.10); however, I believe that replacing (2.10) by the 'realistic' boundary conditions (2.12)–(2.14) has only a small stabilizing effect. With our values, $\lambda_1 \approx 0.35$ and $\lambda_2 \approx 45$, and from the figure we see that Q_c attains its maximum value ($Q_c \approx 4200$) for $\bar{\lambda} = \bar{\lambda}_c \approx 0.72$. Note, however, that a box with aspect ratio λ only allows discrete wavelengths λ/n, $(n = 1, 2, ...)$, corresponding to n pairs of rolls and that for large λ one might expect to find $n \approx \lambda/\bar{\lambda}_c$.

§2.1.6. *Numerical methods*

Fully nonlinear solutions have to be obtained numerically. I use a two-dimensional version of the three-dimensional code described by Matthews *et al.* (1995; see also Weiss *et al.* 1996), which is related to codes developed for other non-magnetic problems (Cattaneo *et al.* 1991; Brummell, Cattaneo & Toomre 1995; Brummell *et al.* 1996). This code uses a pseudo-spectral method in the x-direction, coupled with fourth-order finite differences in the z-direction. Thus boundary conditions (2.12) and (2.13) for the magnetic field can readily be satisfied. Timestepping is by a second-order Adams-Bashforth scheme, limited by the Courant condition and its diffusive analogue (in practice the timestep is invariably limited by horizontal thermal diffusion). For $\lambda = 6$, sufficient accuracy is typically obtained with 32 mesh intervals in the z-direction and 256 points in the x-direction. Such 2D computations can readily be carried out on workstations, whereas the corresponding 3D calculations require a massively parallel machine.

§2.2. *Varying the aspect ratio*

The results of any numerical experiment depend critically on the choice of boundary conditions. In my runs, I impose periodicity in the lateral direction, so the solution depends on the aspect ratio, λ. In this section, I show that the width of the box can have a profound effect on the resulting flow. To do this, I first fix the values of all the physical parameters, setting $\hat{R} = 100\,000$ and taking a particular value for Q, and hence for the strength of the magnetic field. As already stated, the idealized boundary conditions (2.9) are imposed at the base of the box, where the magnetic field is held vertical and the temperature is fixed, but introduce the 'realistic' conditions (2.12)–(2.13) at the top, where the field is matched continuously to an external potential field and energy is lost by radiation.

With weak fields ($Q \leq 200$), behaviour is effectively kinematic, while strong fields ($Q \geq 2000$) allow only steady convection to occur. A value of Q is required that allows different types of dynamically interesting behaviour, and hence $Q = 700$ is chosen. The results of runs for $\frac{1}{3} \leq \lambda \leq 16$ are summarized in Table 2.1 which gives the number n of cells in the box, the rms velocity $u_{\rm rms} = \sqrt{\langle\langle\langle|\mathbf{u}|^2\rangle_x\rangle_z\rangle_t}$, the normalized mean surface temperature $\bar{T}$ and the normalized energy transport $\overline{T^4}$, where

$$\bar{T} = \langle\langle\theta T(x, z_0, t)\rangle_x\rangle_t \quad \text{and} \quad \overline{T^4} = \langle\langle[\theta T(x, z_0, t)]^4\rangle_x\rangle_t, \tag{2.17}$$

and the average maximum field strength $B_{\rm max} = \langle\max|\mathbf{B}|\rangle_t$ (where the initial uniform field strength is unity).

λ	*pattern*	n	$u_{\rm rms}$	$\bar{T}$	$\overline{T^4}$	$B_{\rm max}$
$\frac{1}{3}$	*no convection*	0	–	1.000	1.000	1.0
$\frac{1}{2}$	*steady convection*	1	0.16	1.050	1.215	3.7
$\frac{2}{3}$	*travelling wave*	1	0.37	1.079	1.363	7.5
1	*travelling wave*	1	0.45	1.097	1.465	14.6
$\frac{4}{3}$	*travelling wave*	1	0.50	1.091	1.435	14.7
2	*travelling wave*	2	0.45	1.098	1.470	15.4
$\frac{8}{3}$	*aperiodic oscillation*	3	0.44	1.098	1.468	17.1
4	*transitional*	4	0.46	1.095	1.454	18.3
6	*flux separation*	1	0.68	1.092	1.445	24.0
8	*flux separation*	1	0.80	1.093	1.449	25.9
16	*flux separation*	2	0.71	1.093	1.448	27.5

Table 2.1. *Varying the aspect ratio, λ, for a fixed field strength ($Q = 700$). Quantities given are: the pattern of convection; the number of cells in the box, n; the rms velocity, $u_{\rm rms}$; the normalized mean surface temperature, $\bar{T}$; the normalized energy transport, $\overline{T^4}$; and the maximum field strength, $B_{\rm max}$, as the box size is varied.*

§2.2.1. Weak convection in narrow boxes ($\lambda \leq 2$)

From Figure 2-2 it is anticipated that convection will be completely suppressed for $\lambda < 0.4$. Indeed, initial perturbations soon die away when $\lambda = \frac{1}{3}$, but with $\lambda = \frac{1}{2}$ the weakly convecting steady solution that is shown in Figure 2-3(a) is obtained. Here the pattern is symmetric about vertical planes through the centres of the plumes. As expected, the rising hot plume expands and the highest velocities are in the narrow sinking plumes. The field lines are weakly distorted and flux is concentrated in the regions of converging flow.

Reflection symmetry is broken in a bifurcation at $\lambda \approx 0.6$, which gives rise to travelling waves. Figure 2-3(b) shows such a solution for $\lambda = 1$. The plumes drift leftward without change of form but are markedly asymmetric, being tilted by the streaming flow. The magnetic field is weakened by expansion in the rising plume, but there are stronger flux concentrations where the horizontal in-flows meet. When $\lambda = 2$ the box is wide enough to accommodate two pairs of plumes, and the waves

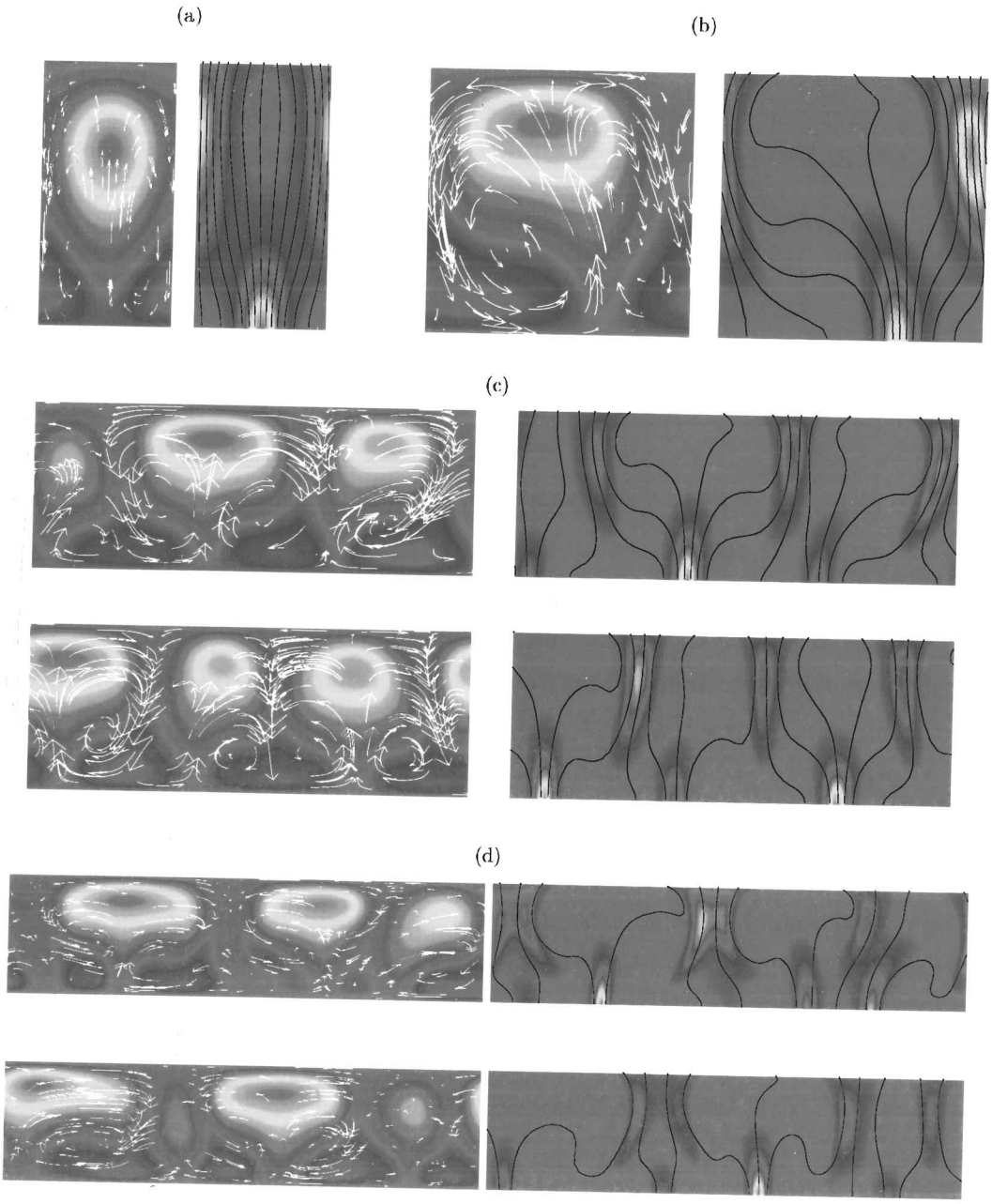

Figure 2-3. *The effects of increasing the aspect ratio λ for a fixed field strength ($Q = 700$): (a) shows $\lambda = \frac{1}{2}$, (b) $\lambda = 1$, (c) $\lambda = \frac{8}{3}$, (d) $\lambda = 4$. In each pair of images the left panel shows the relative temperature fluctuations, with velocity arrows, and the right panel gives the field strength $|\mathbf{B}|^2$ with field lines. In each case, red is the highest value and violet the lowest.*

have become weakly modulated, so that they oscillate aperiodically as they drift.

An advantage of using the radiative temperature boundary condition (2.14) rather than holding the surface temperature constant (2.10) is that the temperature, $T(x, z_0, t)$, on the upper surface is easily displayed. In this way a qualitative idea of the full time-dependent behaviour may be seen instantly. For example Figure 2-4(a) clearly shows that the solution for $\lambda = \frac{1}{2}$ is steady, whereas $\lambda = \frac{2}{3}$ in Figure 2-4(b) gives a travelling wave.

§2.2.2. Spatially modulated oscillations in medium-sized boxes ($\frac{8}{3} \leq \lambda \leq 4$)

Once $\lambda > 2$ the solutions are no longer severely constrained by the width of the box, and can pick a length scale that is close to the preferred wavelength, $\bar{\lambda}_c$, for linear instability. Convection consequently becomes much more vigorous. When $\lambda = \frac{8}{3}$ the box contains three rising plumes that oscillate chaotically and much more vigorously than was the case for $\lambda = 2$ as is demonstrated in Figure 2-5(a),(b). Images at opposite phases of a spatially modulated oscillation are displayed in Figure 2-3(c). Apart from a slow drift to one side, the positions of the plumes at the base of the layer (where $\zeta > 1$) are virtually unaltered, whereas there are large changes in velocity at the top (where $\zeta < 1$) as adjacent plumes alternate in strength. This pattern of behaviour is characteristic of convection in strong fields.

Results for the run with $\lambda = 4$ are initially similar to those for $\lambda = \frac{8}{3}$, except that there are now four plumes that oscillate chaotically. However, there is a slow secular change as a particular plume grows in size and oscillates less, while the other plumes contract accordingly. At the same time, practically all magnetic flux is cleared from within the largest plume and remains clustered at its edge. However, the growth of such a plume is soon halted and it sometimes shrinks again, while another plume is allowed to grow. This aperiodic cycle continues, as illustrated in Figure 2-3(d). Note that at different times there may be 2, 3 or 4 plumes in the box, as may be seen in Figure 2-5(c).

§2.2.3. Separation of the magnetic field in wide boxes ($\lambda \geq 6$)

The behaviour just described is a prelude to the appearance of an entirely new regime. Increasing the box size from $\lambda = 4$ to $\lambda = 6$ allows the development of a qualitatively different pattern. Initially, there are seven plumes in the box, undergoing spatially modulated oscillations – as would be predicted from the results that have just been described. Just as for $\lambda = 4$, some of these plumes begin to grow, while others shrink and vanish. This evolutionary process can again be

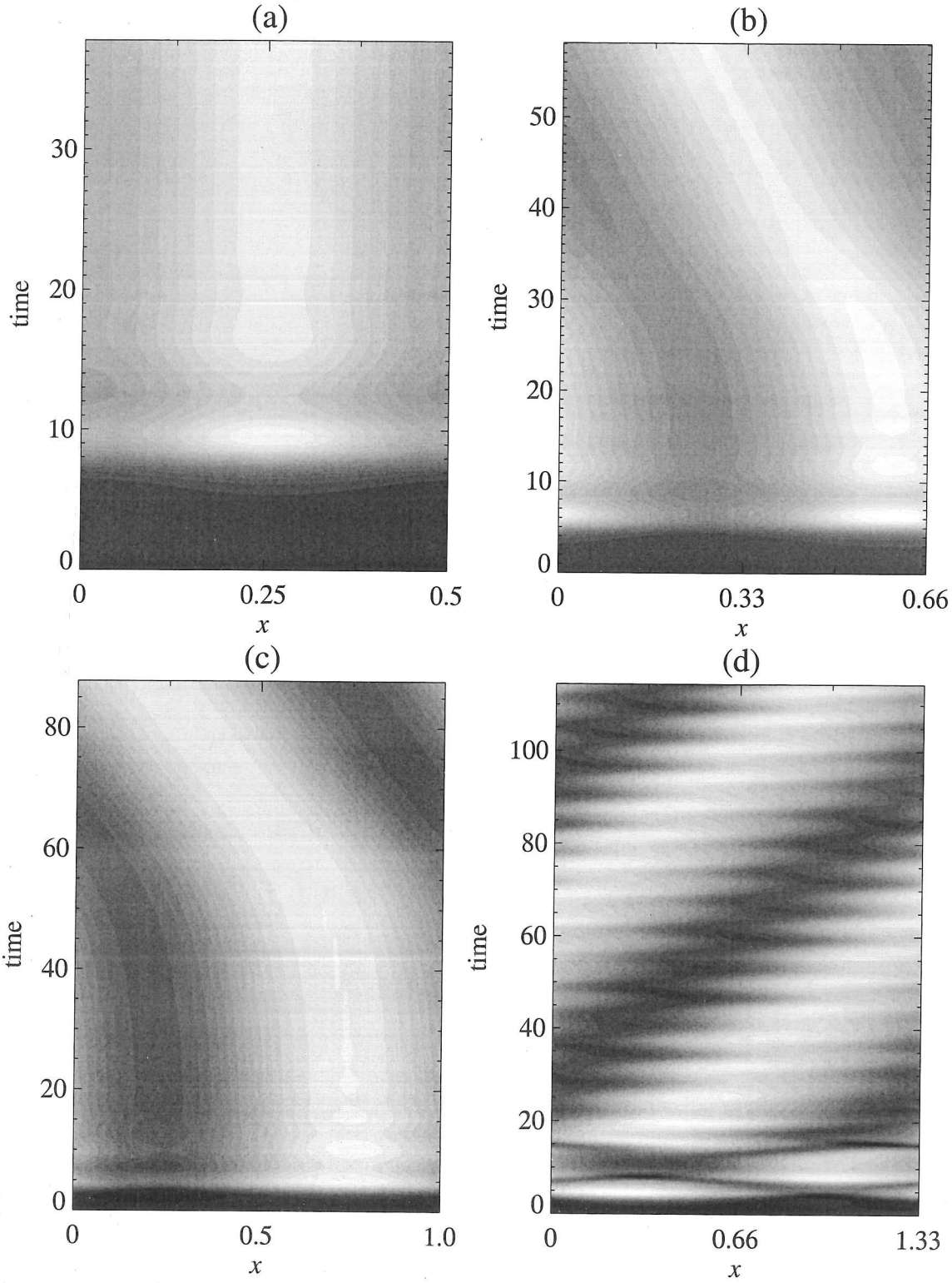

Figure 2-4. *The variation of surface temperature with time for* $Q = 700$. *(a) shows* $\lambda = \frac{1}{2}$, *(b)* $\lambda = \frac{2}{3}$, *(c)* $\lambda = 1$, *(d)* $\lambda = \frac{4}{3}$.

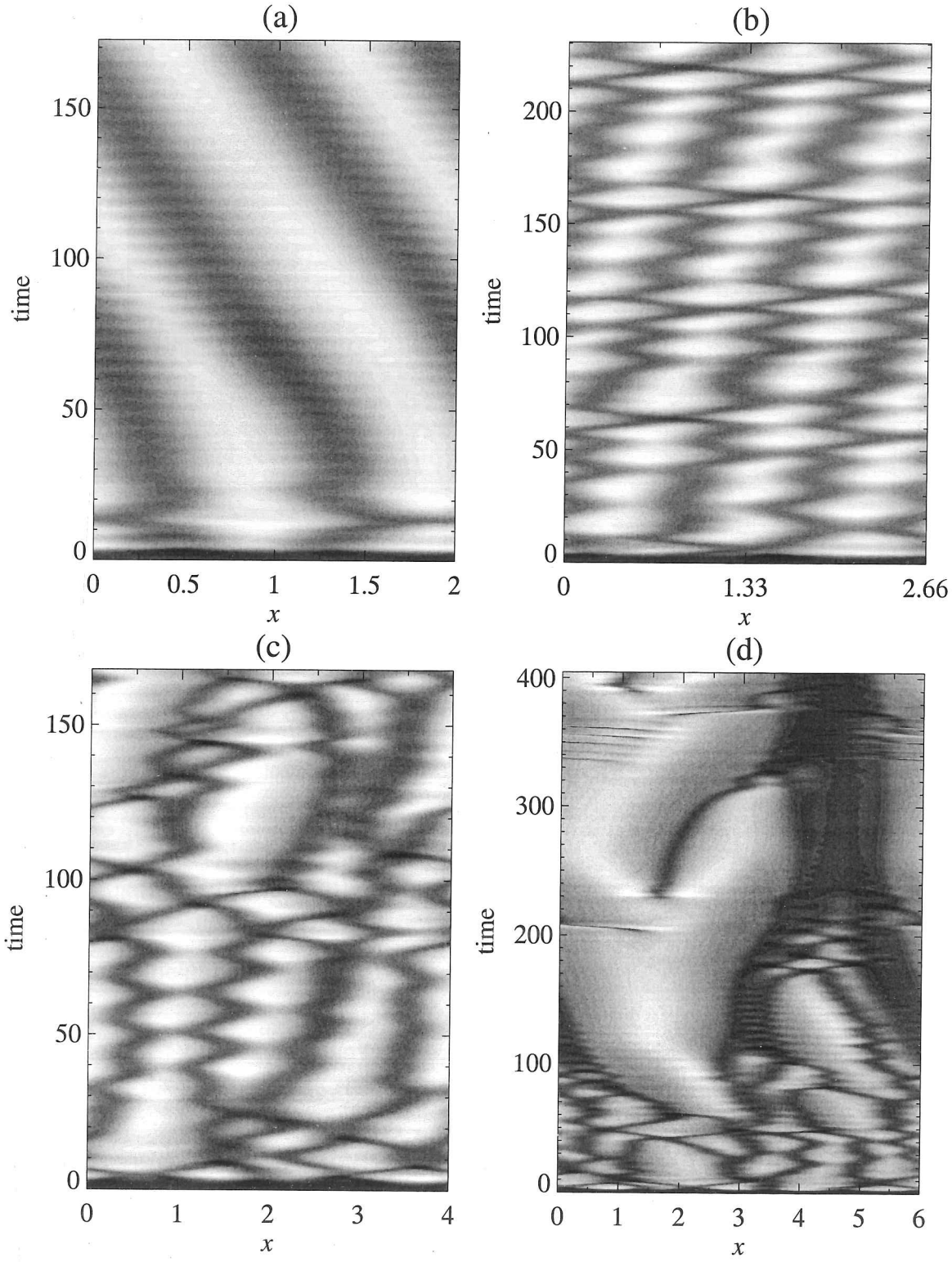

Figure 2-5. *The variation of surface temperature with time for* $Q = 700$. *(a) shows* $\lambda = 2$, *(b)* $\lambda = \frac{8}{3}$, *(c)* $\lambda = 4$, *(d)* $\lambda = 6$. *In the final case, the early oscillations and the formation of the large plume are clearly visible, as is the irregular splitting of the plume.*

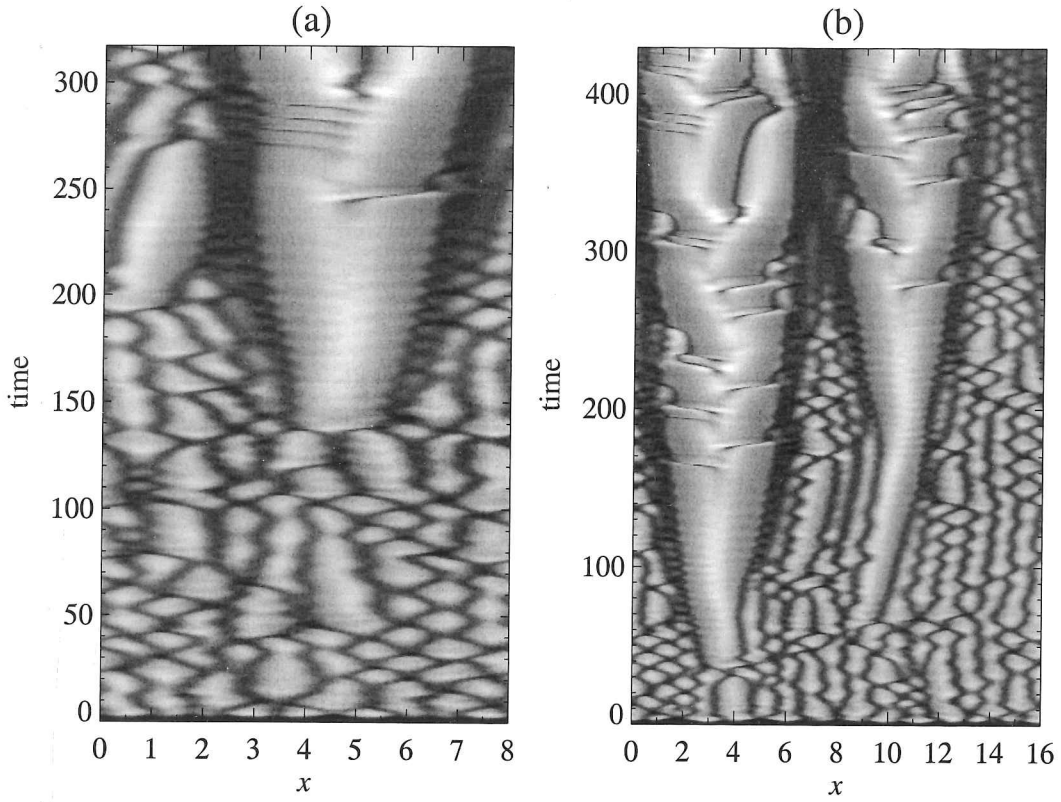

Figure 2-6. *The variation of surface temperature with time for $Q = 700$. (a) shows $\lambda = 8$, (b) $\lambda = 16$. Again note that the oscillations give way to the formation of large plumes, which split irregularly. A box with $\lambda = 16$ is clearly wide enough to accommodate two such plumes.*

visualized by displaying the temperature, $T(x, z_0, t)$, on the upper surface. The grey-scale image in Figure 2-5(d) shows spatially modulated oscillations for $t < 50$. Subsequently, some plumes (such as that at $x \approx 2$) expand and swallow up an immediate neighbour, leaving a single plume of twice the size where there were previously two. The horizontal outflow of the resulting plume is then strong enough for it to resist being torn apart again. This process continues and the total number of plumes declines until only two are left. At this stage, the plumes themselves contain virtually no magnetic flux and the magnetic field is confined to the regions between them, where convection is inhibited. The two plumes then engage in a battle for domination as the horizontal outflow at the top of each exerts a lateral force on the magnetic flux between them. Slowly, one of the plumes – usually, but not always, the one that was initially the smaller – is reduced in size, until the surrounding magnetic field is able to suppress it. This results in a single convective plume occupying approximately $\frac{2}{3}$ of the box.

In Figure 2-7 such a solution is shown for the qualitatively similar case of

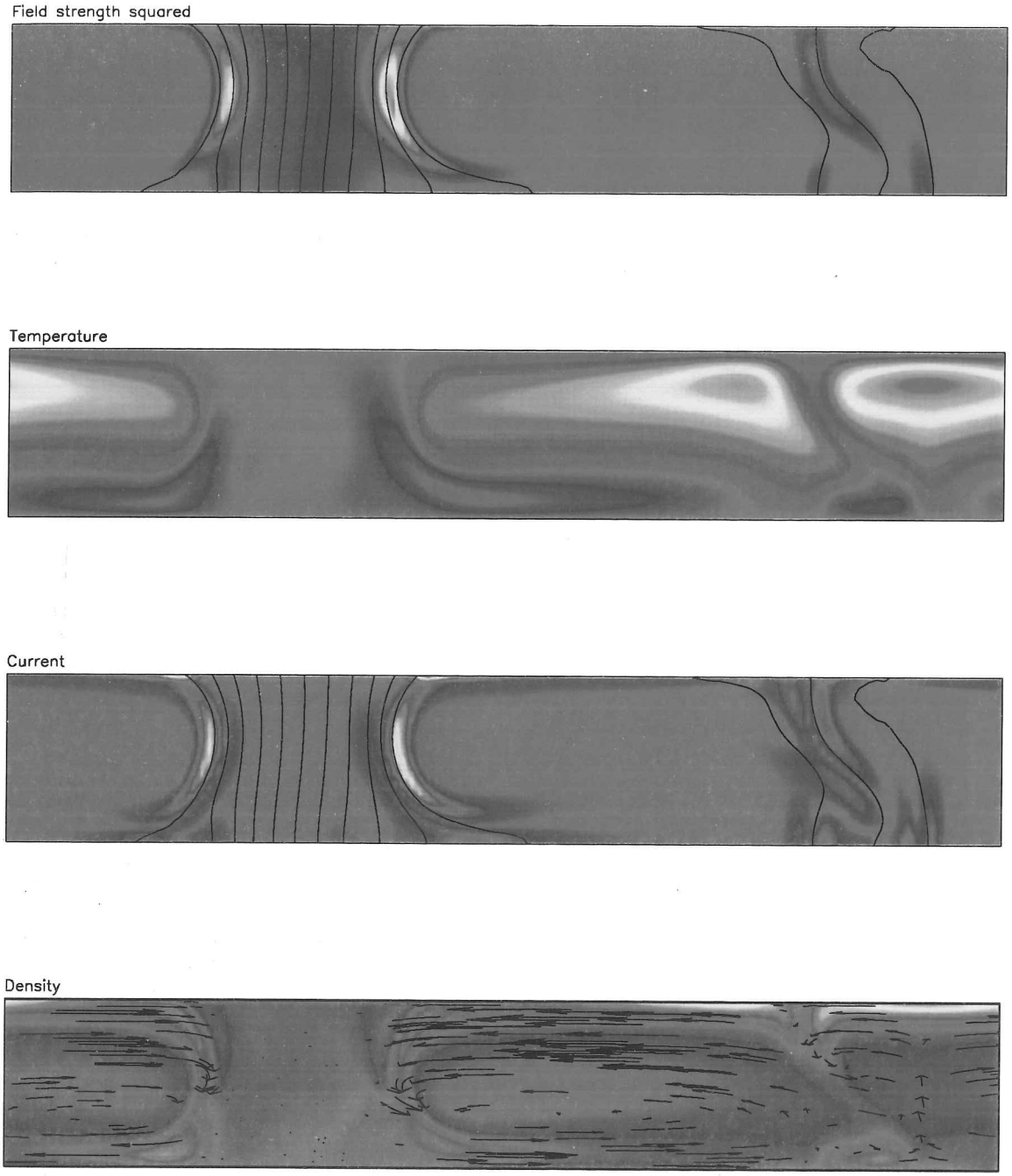

Figure 2-7. $Q = 500$. *Four frames taken at a single moment in time showing several physical properties of the system; (a) Shading is* $|\mathbf{B}^2|$, *with superposed field lines, (b) Temperature, with velocity arrows, (c) Electric current,* $\mathbf{j} = \nabla \wedge \mathbf{B}$, *with field lines, (d) Density, with velocity arrows. Note how the splitting of the plumes is associated with some accumulated flux in the region of the split.*

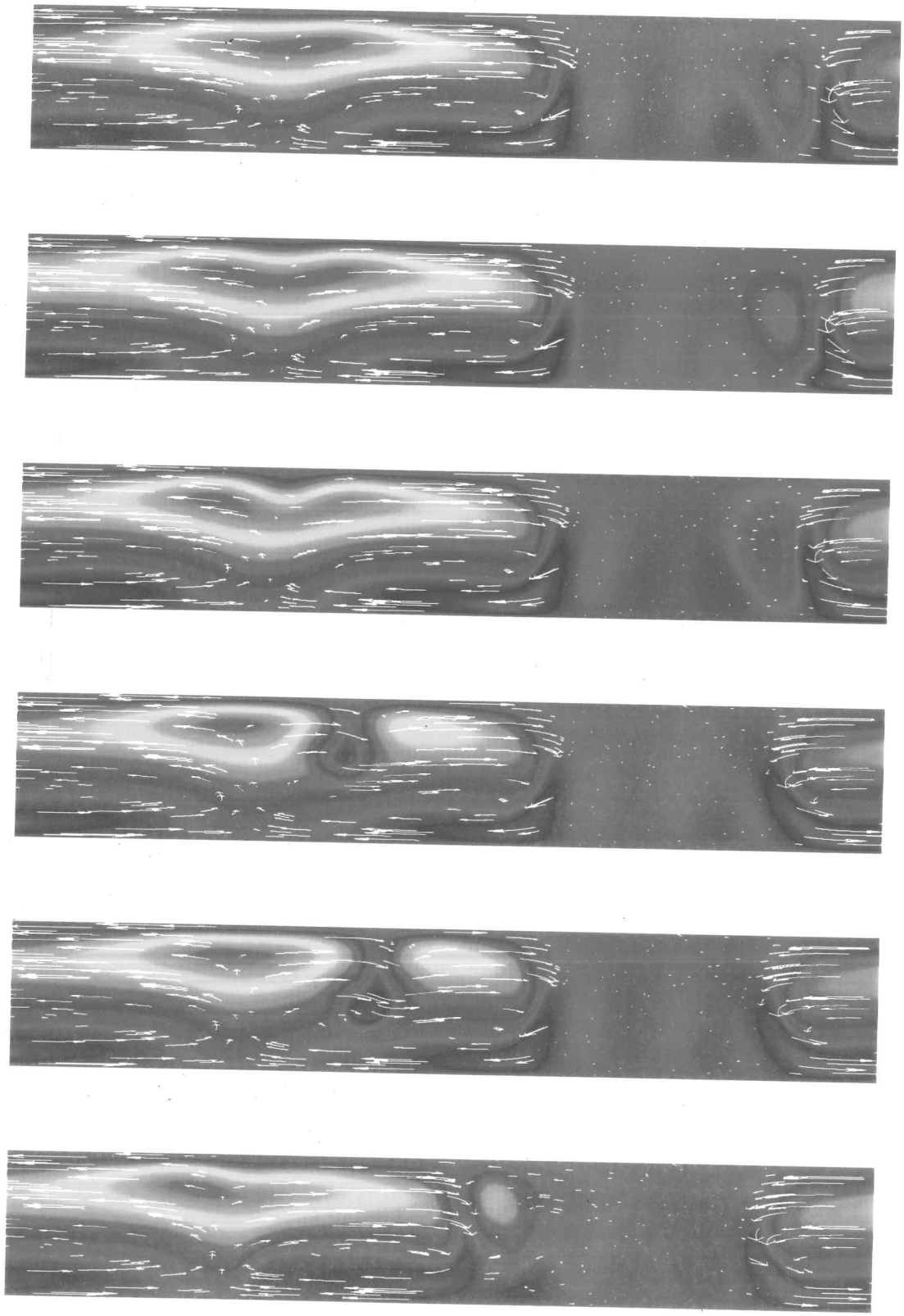

Figure 2-8. *Six snapshots of temperature with superposed velocity arrows showing splitting of the convective plume for* $Q = 700$ *and* $\lambda = 6$. *The elapsed time between the first and last frames is about 8, but for clarity the time between frames is not constant.*

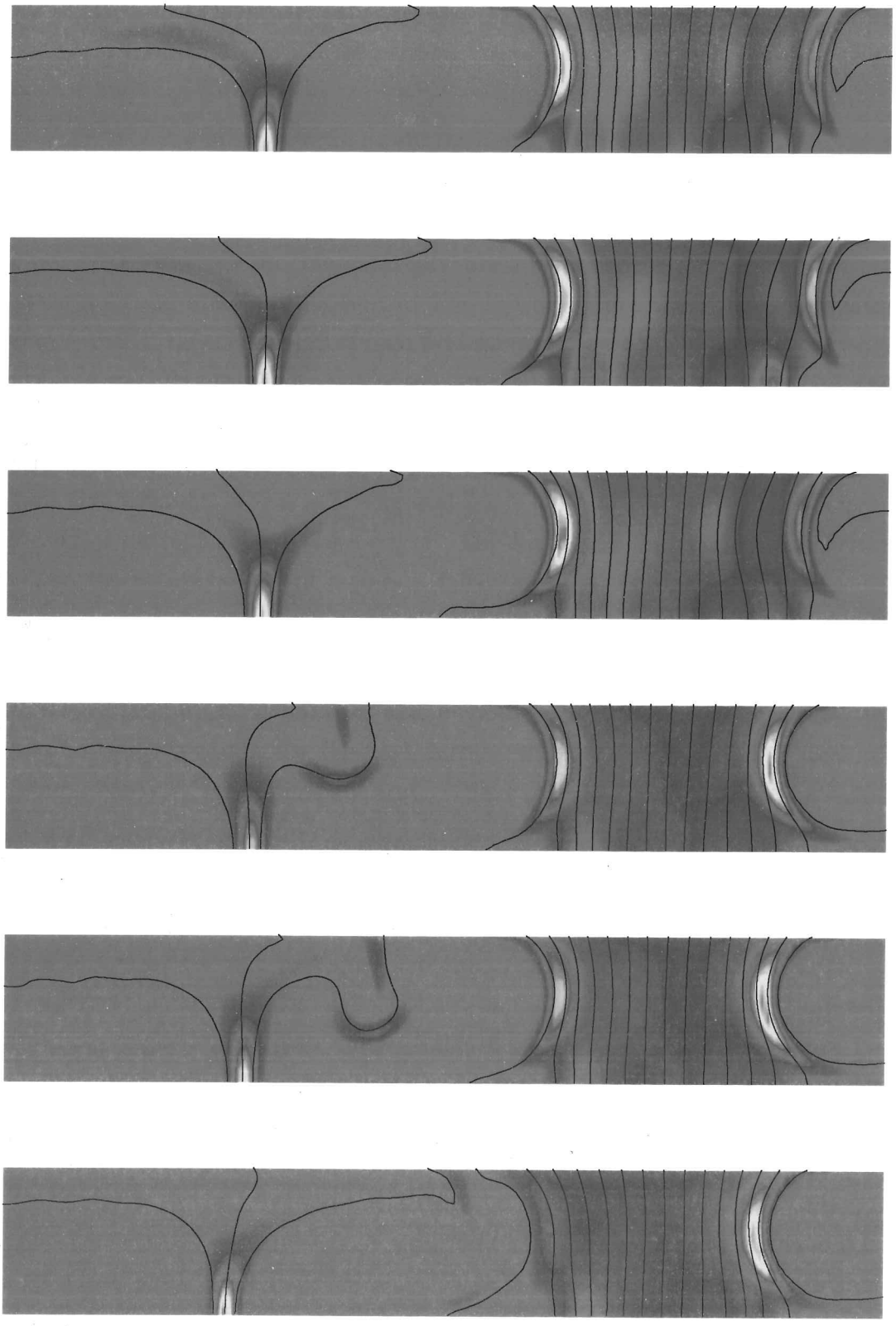

Figure 2-9. *As for Figure 2-8 but showing the corresponding field strengths with superposed field lines.*

$Q = 500$. Figure 2-7(a) shows how the magnetic field is contained in one region where convection is effectively suppressed. Within this region the field is vertical and fairly uniform. Figure 2-7(b) shows the single plume of hot fluid, rising at its centre, moving horizontally outwards, cooling, and falling at its edges. Strong current sheets are seen in Figure 2-7(c) at either edge of the plume.

This plume can settle to what appears to be a steady state but, as is apparent in Figure 2-5(d), it is liable to split. Figure 2-8 and Figure 2-9 show a time-sequence that demonstrates this process. Initially, there is a broad, symmetric convection cell with a strong upflow in its centre. The hot rising gas then moves horizontally outwards until it meets the wall of high field strength, before sinking suddenly again. The plume itself is practically field-free – in places the field strength is reduced to one-millionth of its original value – except for a narrow flux concentration at its base, where the field is pinned down by the horizontal inflow. The remainder of the box, on the other hand, has a strong and fairly uniform vertical field throughout, with narrow current sheets at its edges. The high field strength halts convection here, and the region is held at a steady, fairly cool temperature.

At the centre of the plume, buoyancy braking (see Spruit *et al.* 1990) inhibits upward motion. From time to time this causes local cooling to occur and the plume effectively splits into two. Some of the magnetic flux accumulated near the upper stagnation point is caught by the horizontal outflow and is rapidly expelled, while the plume recovers its symmetric state. This process takes place on a dynamic timescale and repeats indefinitely at irregular intervals.

This new pattern of behaviour persists thereafter as the aspect ratio is increased. When $\lambda = 8$ the main plume takes a little longer to form, and is narrower relative to the box size (see Figure 2-6(a)). Apparently this width of box is on the borderline between being able to hold one stable plume and two; indeed, it takes much longer for the two parts of the main plume to recombine once it has split. Such behaviour is consistent with the results for $\lambda = 16$, which are shown in Figure 2-6(b). The box now contains two large stable plumes, which undergo irregular dynamic splitting independently of each other. Magnetic flux is trapped in the two regions that lie between them: in one, the field is strong enough to suppress convection; in the other, a weaker field allows feeble spatially modulated oscillations to survive. Table 2.1 confirms that the spatially averaged behaviour does not change significantly for $\lambda > 6$. I conclude therefore that an aspect ratio $\lambda = 6$ should be sufficient to deliver the true pattern of convection, namely one that remains unchanged as λ is indefinitely increased.

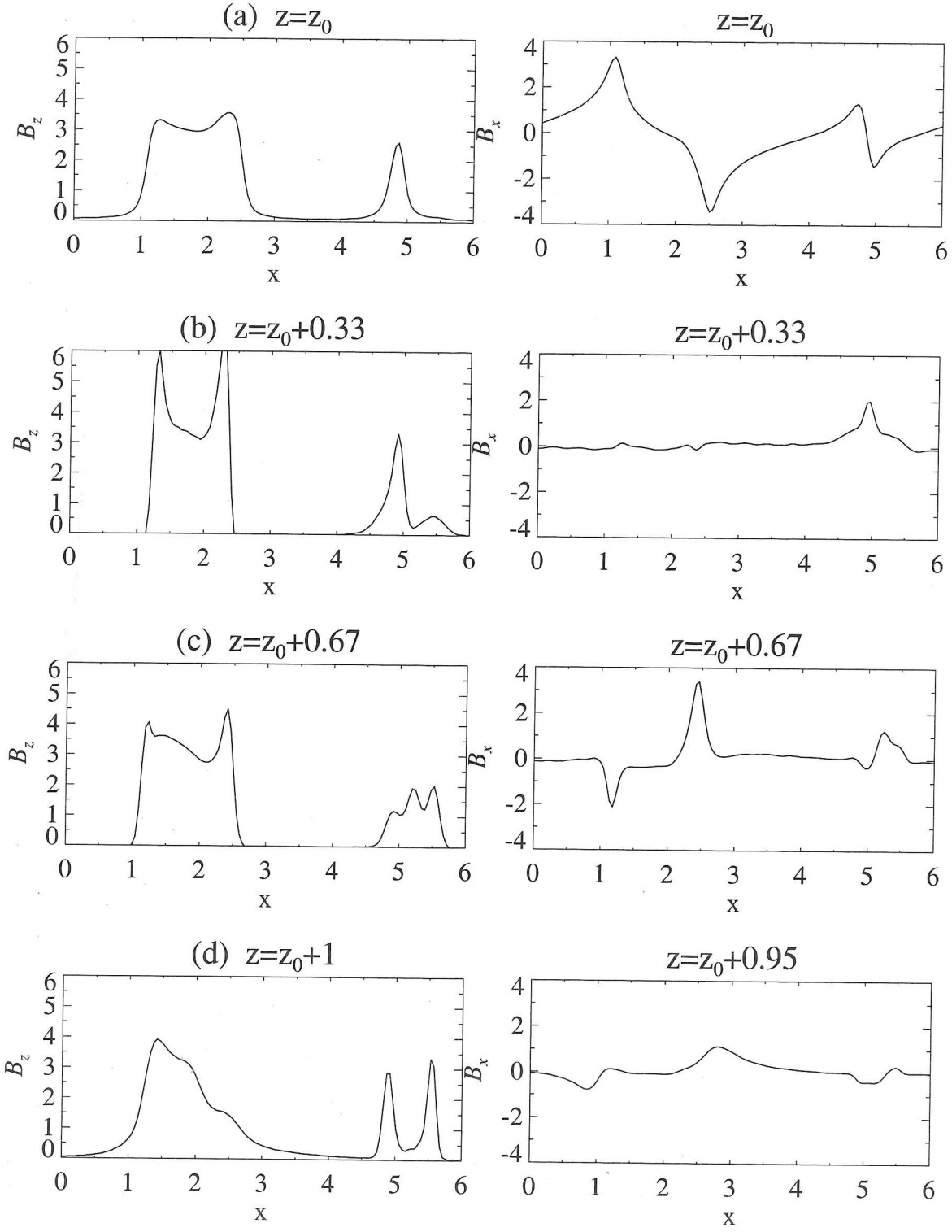

Figure 2-10. *B_z (left) and B_x (right) at (a) $z = z_0$ (the surface); (b) $z = z_0 + \frac{1}{3}$; (c) $z = z_0 + \frac{2}{3}$; (d) $z = z_0 + 1$ (B_z) and $z = z_0 + 0.95$ (B_x). In each case $Q = 500$ and $\lambda = 6$. The field profiles are taken at the same time as Figure 2-7.*

λ	*pattern*	n	u_{rms}	$\bar{T}$	$\overline{T^4}$	$B_{\max}$
$\frac{2}{3}$	*travelling wave*	1	0.64	1.082	1.379	17.5
$\frac{4}{3}$	*travelling wave*	1	0.72	1.102	1.492	24.4
2	*flux separation*	2	0.67	1.105	1.501	46.3
$\frac{8}{3}$	*flux separation*	1	0.93	1.105	1.512	30.2
4	*flux separation*	2?	0.76	1.104	1.504	26.4
6	*flux separation*	1	1.08	1.101	1.496	38.0

Table 2.2. $Q = 500$. *The column entries are defined in (2.17).*

λ	*pattern*	n	u_{rms}	$\bar{T}$	$\overline{T^4}$	$B_{\max}$
$\frac{2}{3}$	*steady convection*	1	0.25	1.060	1.268	6.3
$\frac{4}{3}$	*periodic oscillations*	1	0.31	1.080	1.377	8.9
2	*aperiodic oscillations*	2	0.31	1.079	1.372	7.6
$\frac{8}{3}$	*aperiodic oscillations*	4	0.32	1.076	1.357	9.8
4	*oscillations*	5	0.30	1.079	1.367	12.2
6	*oscillations*	8	0.30	1.079	1.369	11.1
8	*oscillations*	10	0.31	1.079	1.369	10.6
16	*oscillations*	20	0.32	1.078	1.366	12.7

Table 2.3. $Q = 1000$.

§2.2.4. Varying the aspect ratio for different values of field strength

The process of keeping the field strength fixed and increasing the aspect ratio λ to investigate the different patterns of behaviour was repeated with several values of the Chandrasekhar number Q. The results for $Q = 500$, $Q = 1000$, $Q = 2000$, and $Q = 4000$ are displayed in Table 2.2–Table 2.5 respectively. Although several types of solution are obtained in each case, it is clear that varying the field strength has a profound effect on the resulting behaviour. I investigate this further in the following section.

λ	*pattern*	n	$u_{\rm rms}$	$\bar{T}$	$\overline{T^4}$	$B_{\rm max}$
$\frac{2}{3}$	*steady convection*	1	0.089	1.030	1.123	3.1
$\frac{4}{3}$	*steady convection*	2	0.089	1.034	1.144	3.1
2	*steady convection*	3	0.089	1.033	1.140	3.1
$\frac{8}{3}$	*steady convection*	4	0.089	1.033	1.139	3.1
4	*steady convection*	5	0.096	1.037	1.158	3.9
6	*steady convection*	8	0.092	1.036	1.151	3.6

Table 2.4. $Q = 2000$. *The column entries are defined in (2.17).*

λ	*pattern*	n	$u_{\rm rms}$	$\bar{T}$	$\overline{T^4}$	$B_{\rm max}$
$\frac{2}{3}$	*no convection*	-	–	1.000	1.000	1.0
$\frac{4}{3}$	*steady convection*	2	0.010	1.002	1.007	1.3
2	*steady convection*	3	0.011	1.002	1.007	1.3
$\frac{8}{3}$	*steady convection*	4	0.010	1.002	1.007	1.3
4	*steady convection*	6	0.010	1.001	1.005	1.3
6	*steady convection*	9	0.010	1.001	1.004	1.3

Table 2.5. $Q = 4000$.

§2.3. Varying the field strength

The results in the previous section show that the pattern of convection is constrained in boxes with small aspect ratios. Even when the box contains several plumes (as in Figure 2-3(c) for $\lambda = \frac{8}{3}$), the results may be misleading, since wider boxes allow the magnetic field to separate from the motion. We can, however, be confident that this new form of magnetoconvection is adequately represented for all $\lambda \geq 6$. In this section I therefore fix the aspect ratio by setting $\lambda = 6$ and obtain a single-parameter set of solutions by holding the Rayleigh number fixed (with $\hat{R} = 100\,000$) and varying the field strength. (Decreasing Q for fixed $\hat{R}$ is of course equivalent to increasing $\hat{R}$ for fixed Q but my studies are concerned more with the effects of strong fields on the pattern of convection.) The results for $250 \leq Q \leq 5000$

Q	*pattern*	n	$u_{\rm rms}$	$\bar{T}$	$\overline{T^4}$	$B_{\rm max}$
250	*flux separation*	1	1.554	1.114	1.560	68.0
500	*flux separation*	1	1.076	1.101	1.496	38.0
700	*flux separation*	1	0.681	1.092	1.445	24.0
750	*oscillations*	7	0.412	1.095	1.452	18.2
800	*oscillations*	7	0.374	1.094	1.448	16.0
1000	*oscillations*	8	0.303	1.079	1.369	11.1
1500	*oscillations*	9	0.147	1.049	1.213	4.4
1750	*steady convection*	9	0.112	1.041	1.175	3.8
2000	*steady convection*	8	0.092	1.036	1.151	3.6
3000	*steady convection*	9	0.040	1.014	1.057	2.0
4000	*steady convection*	9	0.010	1.001	1.004	1.3
4500	*no convection*	–	–	1.000	1.000	1.0
5000	*no convection*	–	–	1.000	1.000	1.0

Table 2.6. *Varying the field strength for fixed aspect ratio, $\lambda = 6$, as the Chandrasekhar number, Q, is varied. The column entries are defined in (2.17).*

are summarized in Table 2.6.

§2.3.1. The magnetically dominated regime

Commencing with a magnetic field strong enough to suppress all convection, the field strength is gradually decreased until the kinematic regime is reached. For $Q \geq 4500$, the Rayleigh number is subcritical and all perturbations to the static state, with a uniform vertical field and a uniformly stratified equilibrium atmosphere, decay to zero.

Convection sets in with narrow rolls at $Q_{\rm c} \approx 4200$. For $Q = 4000$, nine small, equally sized cells are rapidly formed (so $\bar{\lambda} = \frac{2}{3}$) and they remain steady throughout the ensuing motion (see Figure 2-12). The pattern in each cell is similar to that of Figure 2-3(a), and the magnetic field is only slightly distorted by the fluid motion. Figure 2-11(a) shows the evolution of the surface temperature $T(x, z_0, t)$

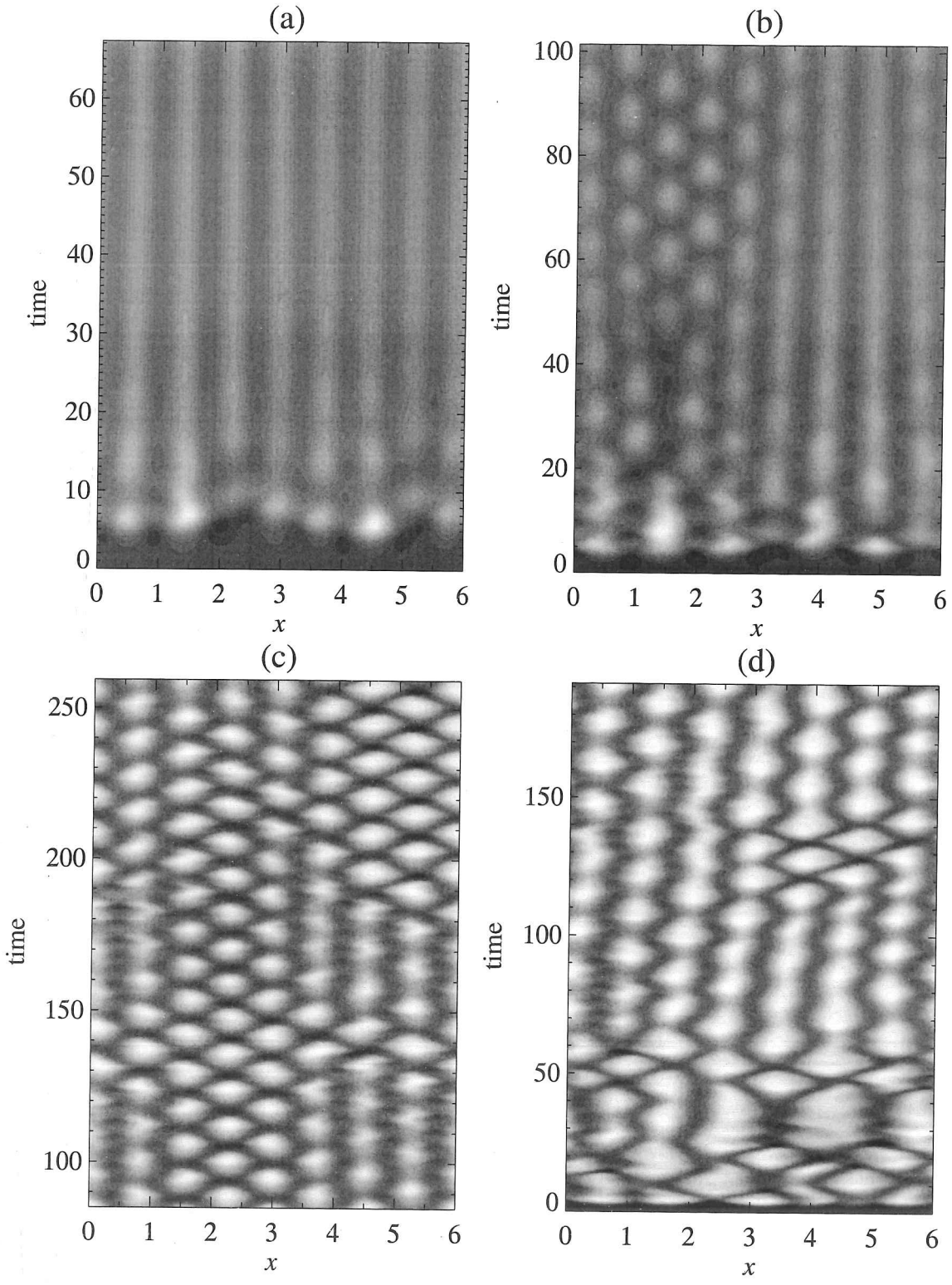

Figure 2-11. *The surface temperature $T(x, z_0, t)$ for: (a) $Q = 2000$, (b) $Q = 1500$, (c) $Q = 1000$, (d) $Q = 750$, with $\lambda = 6$. The case $Q = 700$ is shown in Figure 2-5(d).*

when $Q = 2000$. Once again, the strong field enforces steady motion, somewhat more vigorous than before, but there are now only eight plumes ($\bar{\lambda} = \frac{3}{4}$). Such a solution is displayed in Figure 2-13.

§2.3.2. Spatially modulated oscillations

This steady solution undergoes an oscillatory bifurcation at $Q \approx 1700$. For $Q = 1500$, the preferred convective pattern is that of oscillations that are effectively periodic. The box contains nine plumes of comparable size, which are spatially modulated so that alternate plumes grow and shrink in strength. This solution closely resembles that found by Weiss *et al.* (1990) for $Q = 1200$ but with different boundary conditions.

The motion becomes more vigorous as the magnetic field strength is further reduced. The evolution of the surface temperature for $Q = 1000$ is displayed in Figure 2-11(c). This solution bears little resemblance to the ordered oscillations seen when $Q = 1500$, as in Figure 2-11(b); there are now only eight plumes, which oscillate aperiodically and much more vigorously than before. With $Q = 800$, the chaotic solution has only seven plumes and convection has increased yet further in strength. Finally, at $Q = 750$, the seven plumes are no longer held separate by the field; sporadically two of them merge, only to be torn apart again soon after, as shown in Figure 2-11(d). The field no longer has any persistent structure, and is tossed around by the disordered motion of the fluid. The distribution of the magnetic field and the turbulent nature of the flow in this case can be seen in Figure 2-14.

§2.3.3. Flux separation

As Q is reduced from 750 to 700, there is a very rapid change in the system. When the field strength passes below a certain point, the global behaviour is no longer dominated by the magnetic field and we begin the approach to the kinematic regime: motion is now so vigorous that the magnetic field is only important dynamically in the regions where it is locally strong. The evolution of the surface temperature for $Q = 700$ is shown in Figure 2-5(d) and has already been discussed. We see the formation of the single convection cell that was described in §2.2.3 and illustrated in Figure 2-8. The rms velocity has increased dramatically to nearly 70% of the surface Alfvén velocity, while the maximum velocity has more than double the value of that for $Q = 750$. The rapid oscillations that are visible in Figure 2-5(d) are due to convectively excited magnetoacoustic modes (cf. Steffen, Ludwig & Krüss 1989).

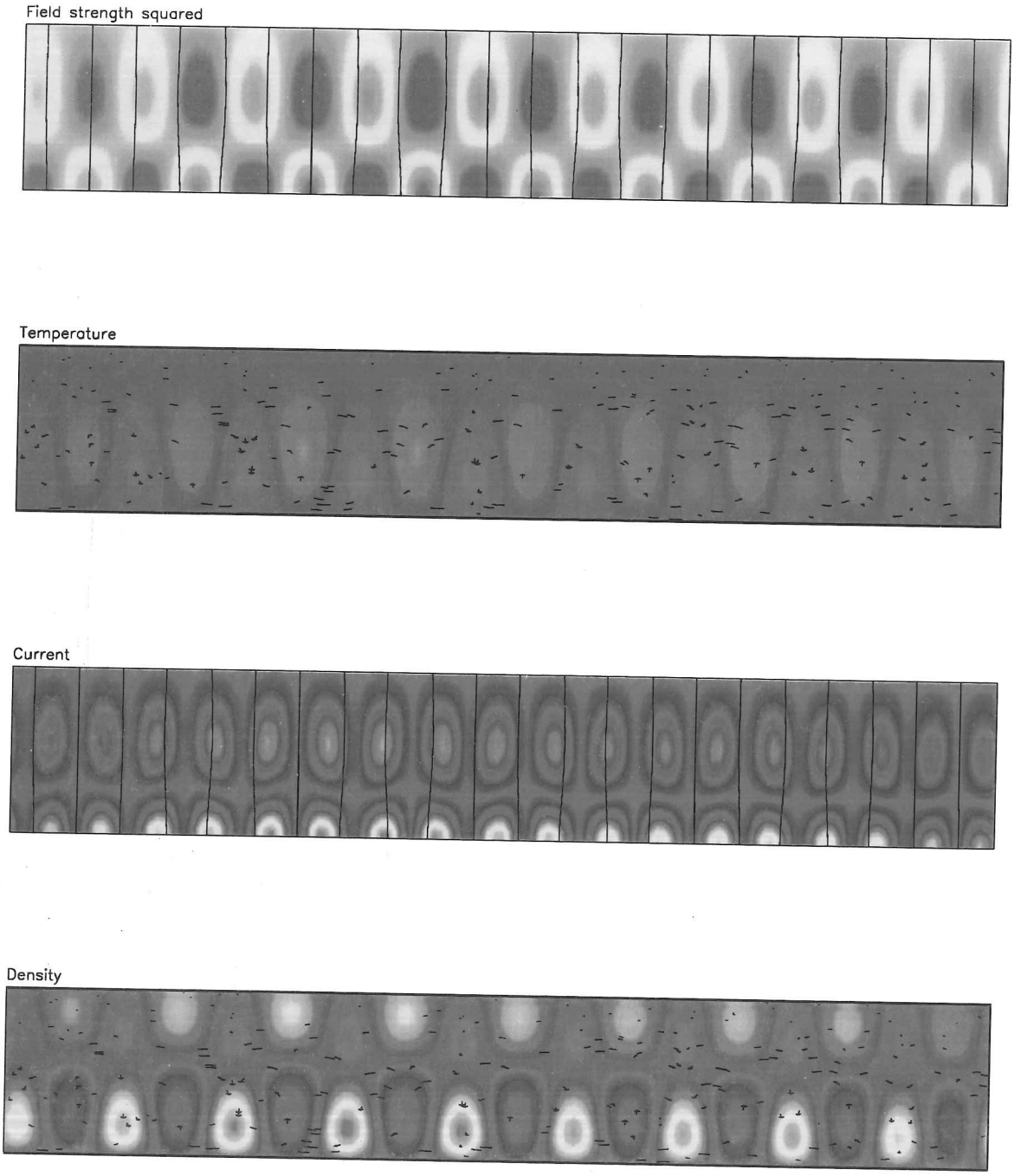

Figure 2-12. $Q = 4000$, *with* $\lambda = 6$. *Four frames taken at a single moment in time (as in Figure 2-7) showing (a) field strength with field lines, (b) temperature with velocity arrows, (c) current with field lines, (d) density with velocity arrows. Here we see very feeble, steady convection of nine plumes.*

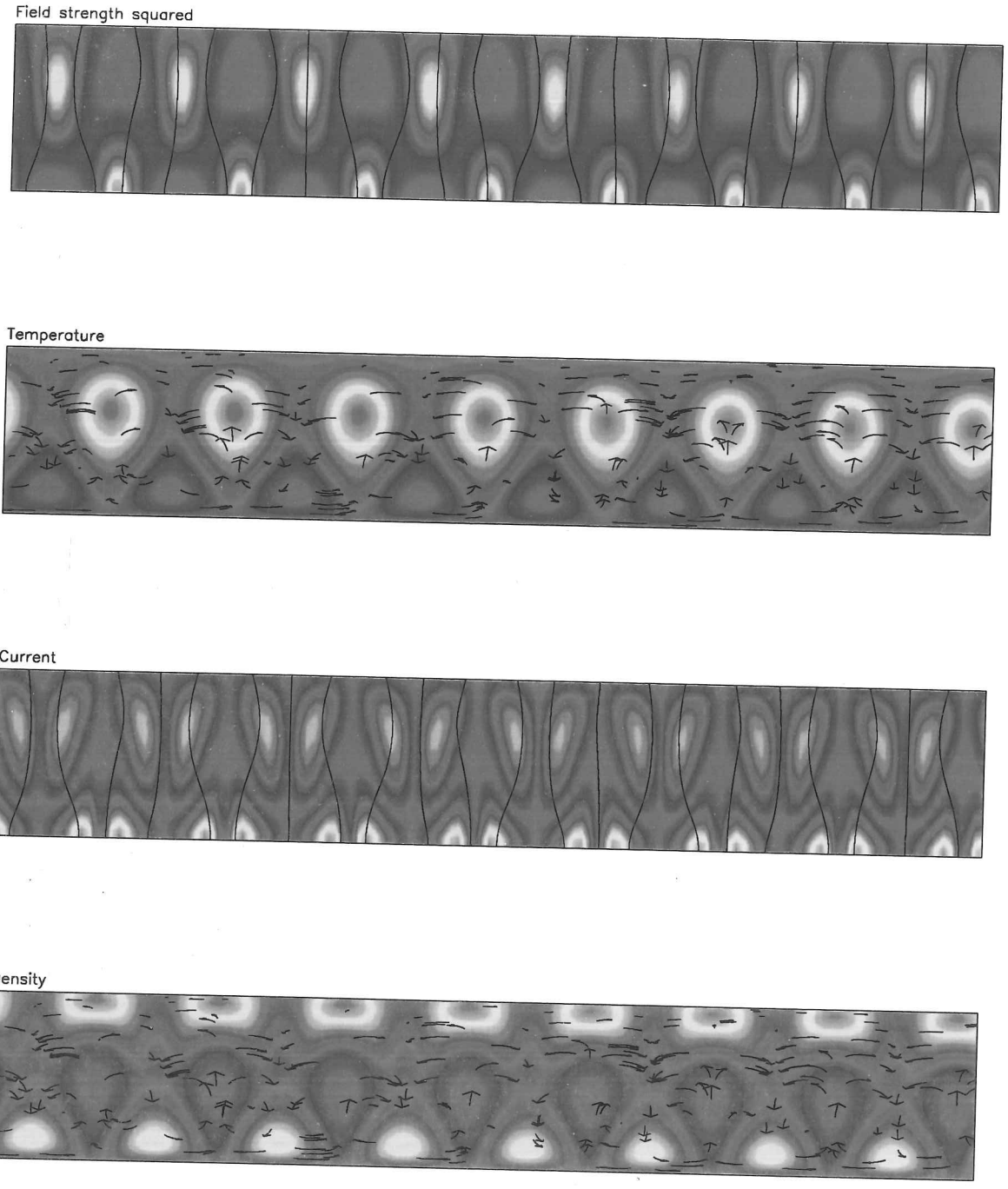

Figure 2-13. $Q = 2000$, $\lambda = 6$. *The pattern shown consists of steady convection of eight plumes. (See caption of Figure 2-12 for description of the frames.)*

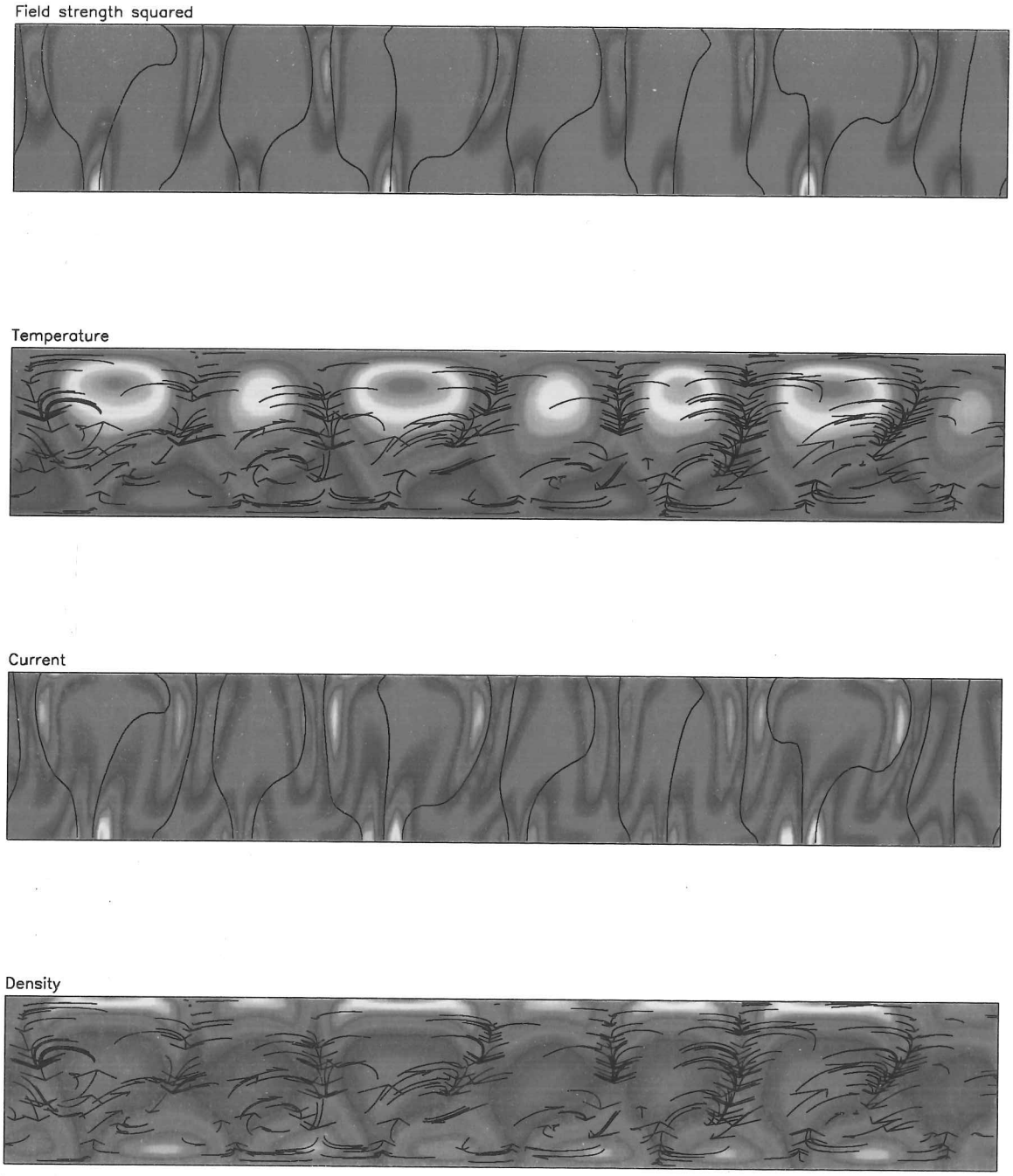

Figure 2-14. $Q = 750$, $\lambda = 6$. *Here we see irregular spatially modulated oscillations of seven plumes. (See caption of Figure 2-12 for description of the frames.) The case* $Q = 1000$ *is given later, in Figure 2-21.*

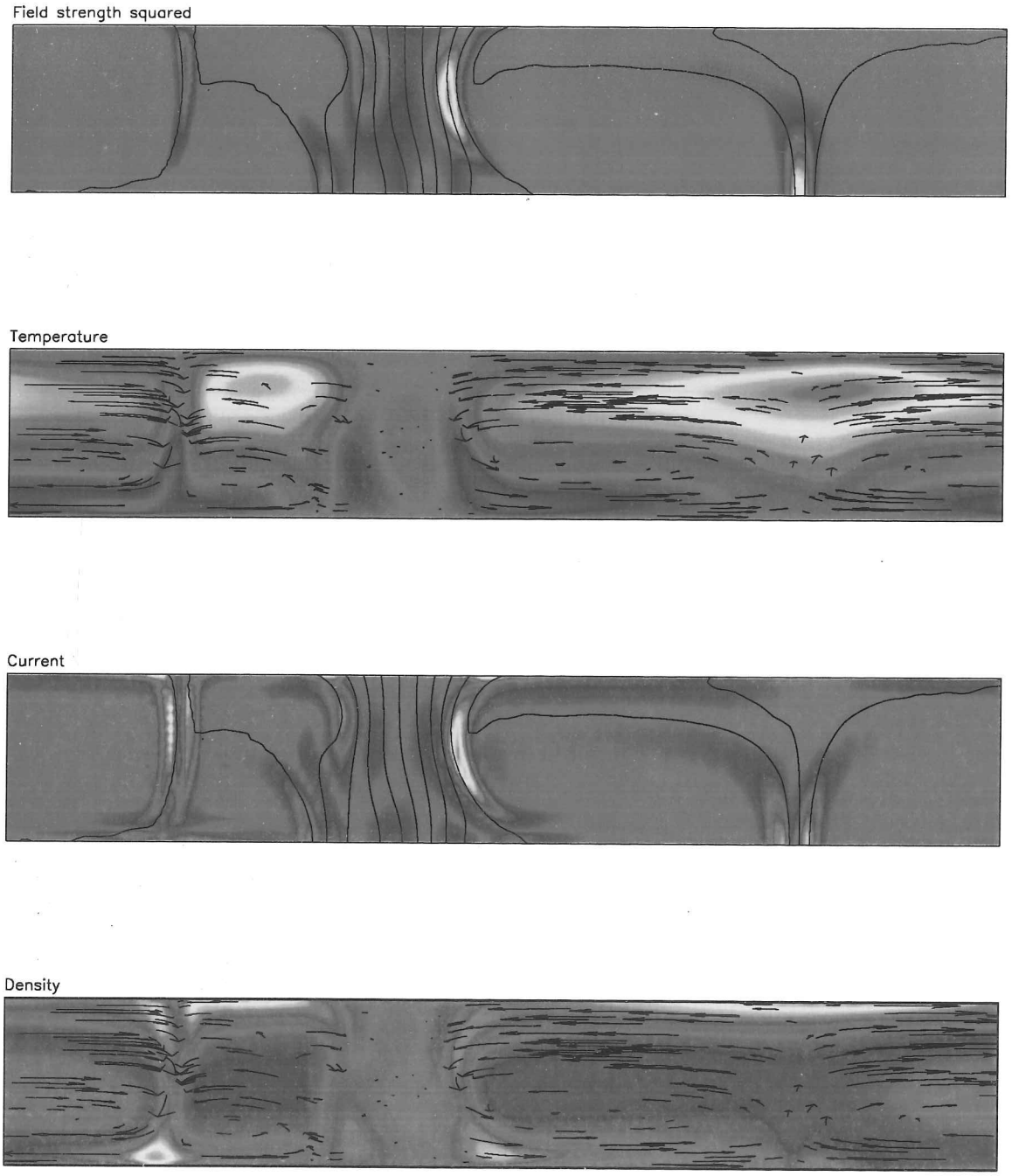

Figure 2-15. $Q = 250$, $\lambda = 6$. *Here we see a single flux-separated plume in the process of splitting (Figure 2-8). The case* $Q = 500$ *is shown in Figure 2-7. (See caption of Figure 2-12 for description of the frames.)*

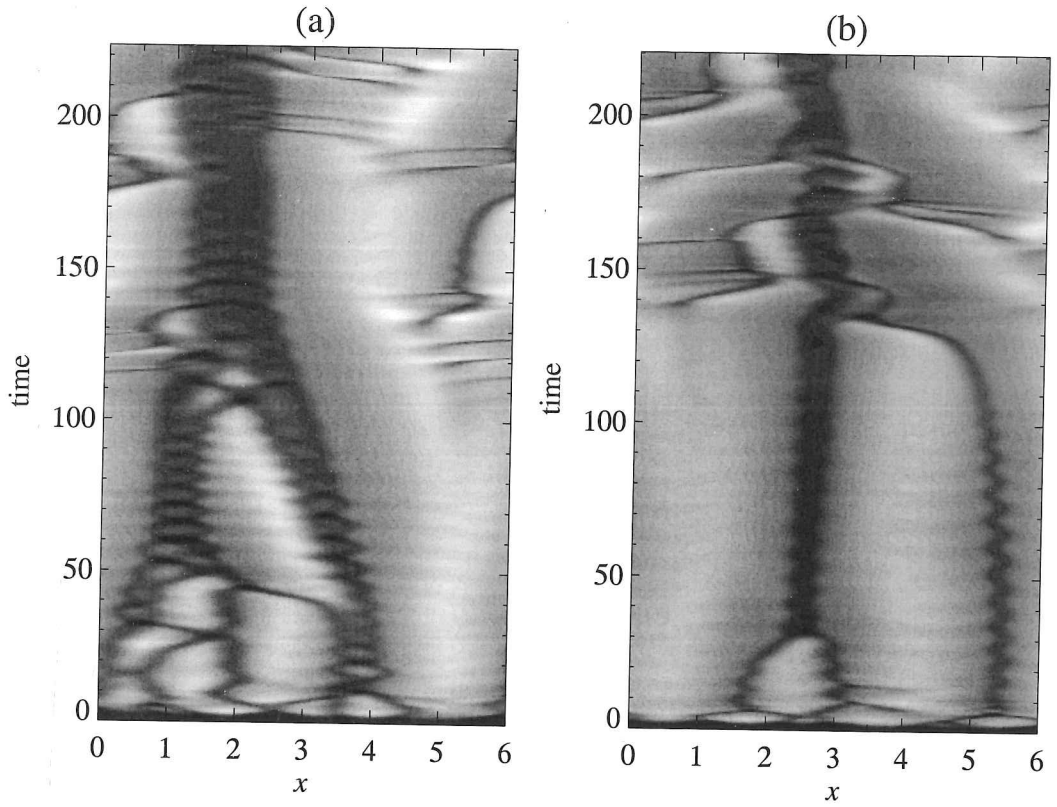

Figure 2-16. *The surface temperature $T(x, z_0, t)$ for (a) $Q = 500$, (b) $Q = 250$, with $\lambda = 6$.*

Further reduction of Q produces very little qualitative change. The two large plumes form more rapidly, the motion becomes more chaotic, and the dynamic splitting and flux expulsion grow more violent. The decreased field strength allows the flow to confine the flux to an ever smaller region, while the plume width increases accordingly. Figure 2-16(a) shows $T(x, z_0, t)$ for $Q = 500$. In the final state, the pair of convection rolls now occupies about three-quarters of the box, with the flux sheet filling the remaining quarter. Compare this to Figure 2-16(b) which shows $T(x, z_0, t)$ for $Q = 250$ in which the rolls take up over 90% of the box. The early oscillations are suppressed far more rapidly as the field distortion becomes ever more nearly kinematic. In both cases, the structure is repeatedly distorted by splitting of the plume, as in Figure 2-8.

The flux sheet (see Figure 2-7(c)) has a strong, predominantly vertical field but the field lines at its edges are curved so as to be concave outwards. At the base of the layer the field lines follow the flow, but at the top the expansion is caused by magnetic pressure, which becomes increasingly important for small z in a strongly stratified atmosphere. The curvature force is almost balanced by a magnetic pressure gradient. Figure 2-10 shows profiles of the vertical and horizontal

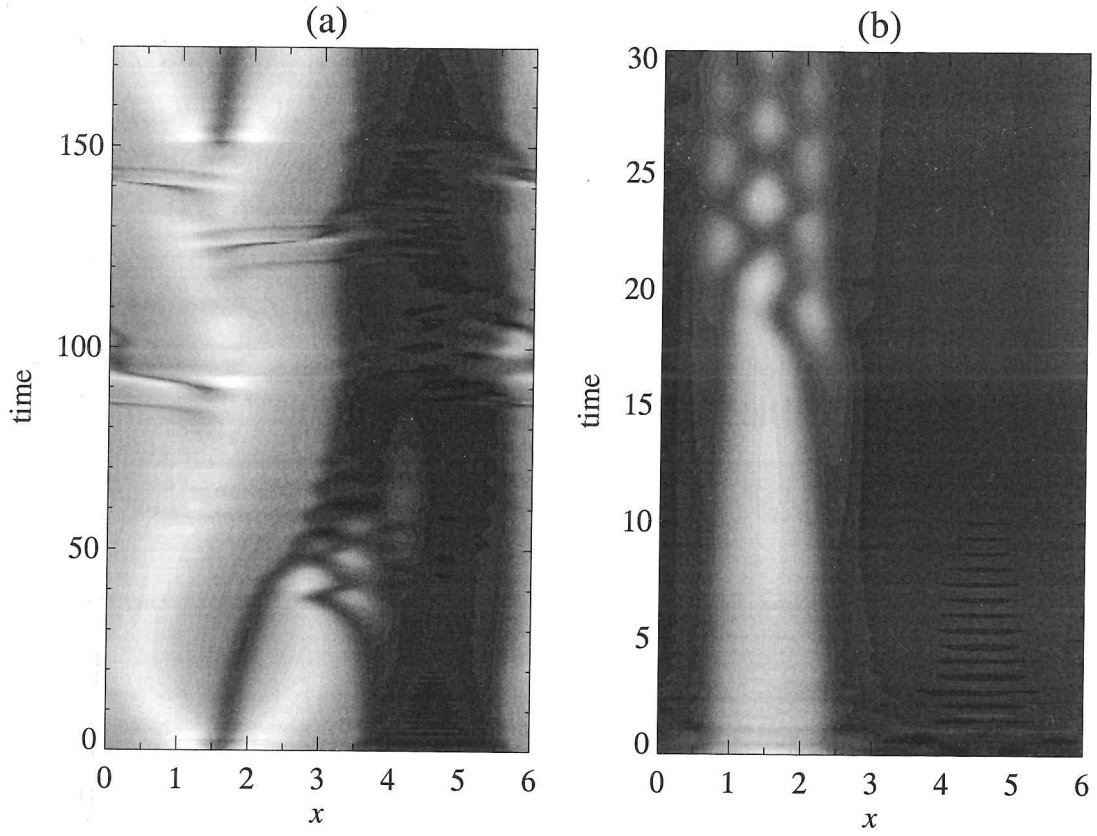

Figure 2-17. *The surface temperature $T(x, z_0, t)$ for: (a) $Q = 1000$ having started from the final state for $Q = 700$, in Figure 2-5(d), and (b) $Q = 3000$ having started from a different 'flux separated' state.*

components of **B** at the middle of the layer, where the field points outwards. Some of the magnetic flux is trapped in the rising plume, but most of it is contained in the main flux sheet. In the centre of the plume the field is fairly uniform but B_z rises to sharp peaks at the edges of the sheet. Close inspection of the solutions shows that these peaks are maintained by slender countercells in the lower part of the box.

The abrupt transition from chaotically modulated oscillations to flux separation at $Q \approx 730$ is associated with hysteresis. In Figure 2-17(a), I plot the surface temperature for a run with $Q = 1000$. Unlike those for Figure 2-11(c), which was started from small random perturbations to the static solution, the initial conditions for this run correspond to the final state for $Q = 700$, as shown in Figure 2-5(d). As was seen in §2.3.2, the case $Q = 1000$ results in spatially modulated oscillations when started from small perturbations of the static solution, but in this case we observe that flux separation is maintained. The flux sheet expands a little due to the increased field strength, while the convective plume contracts and is more liable to split. As Q is further increased, flux separation eventually gives way to small scale

oscillatory convection: with carefully chosen initial conditions, a transient single-cell solution is nevertheless able to persist for a long time (over 100 dimensionless time units), even when $Q = 2000$. Figure 2-17(b) shows a solution obtained for $Q = 3000$ when started from a state of flux separation (a different one to that used to obtain Figure 2-17(a)). Here we observe that the plume breaks up into several oscillatory plumes, yet convection is still confined to the same almost field-free region.

Eventually, when Q is very small, the Lorentz force becomes negligible and the field profile is determined by diffusion. In this kinematic regime the whole box is filled by a single plume ($\bar{\lambda} = \lambda$). I have not attempted to discover whether the plume width saturates at some finite size in the absence of a magnetic field. I note, however, that N.E. Hurlburt (private communication) investigated two-dimensional convection for $\lambda = 12$ in a similar configuration (but with idealized boundary conditions) and found that although the box contained several plumes early on in the simulation, over a long period of time a single plume began to dominate whilst the others dwindled away. Of course, such a plume would be unstable to three-dimensional perturbations in the form of cross-rolls (cf. Matthews *et al.* 1995).

The numerical results given in Table 2.6 are summarized in Figure 2-18. I note that $\overline{T^4}$ rises rapidly with decreasing Q after the onset of convection, with an increased rate of change after the onset of oscillatory convection, but that – despite a rapid increase in $u_{\rm rms}$ – convection becomes *less* efficient after flux separation occurs at $Q \approx 730$, owing to the appearance of stationary flux sheets.

With our scaling, the temperature fluctuations at the upper surface remain small (less than 20%) and the mean vertical temperature gradient $\beta = 1 + z_0(1 - \bar{T})$ differs only slightly from its value in the static polytrope. To measure the efficiency of convection, one should compare the heat transport with the energy that would be conducted down the superadiabatic gradient. I thus define a Nusselt number

$$N = \frac{\overline{T^4} - \beta_{\rm ad}}{\beta - \beta_{\rm ad}}, \tag{2.18}$$

where the adiabatic gradient is given by $\beta_{\rm ad} = [(\gamma - 1)/\gamma](m + 1)\beta$ (Hurlburt *et al.* 1989). With our choice of parameters, $N \approx 5\overline{T^4} - 4$, so the Nusselt number rises from unity (in the absence of convection) to about 4 when $Q = 250$. The difference between this and the much higher value of N for two-dimensional Boussinesq convection at the same value of $\hat{R}$ is due to the combined effects of stratification and of the stagnant flux sheet.

In order to study the dynamics of the solutions at a given time the gas pressure $P = \rho T$, the magnetic pressure $P_m = \frac{1}{2}F|\mathbf{B}|^2$, and the dynamic pressure $P_d =$

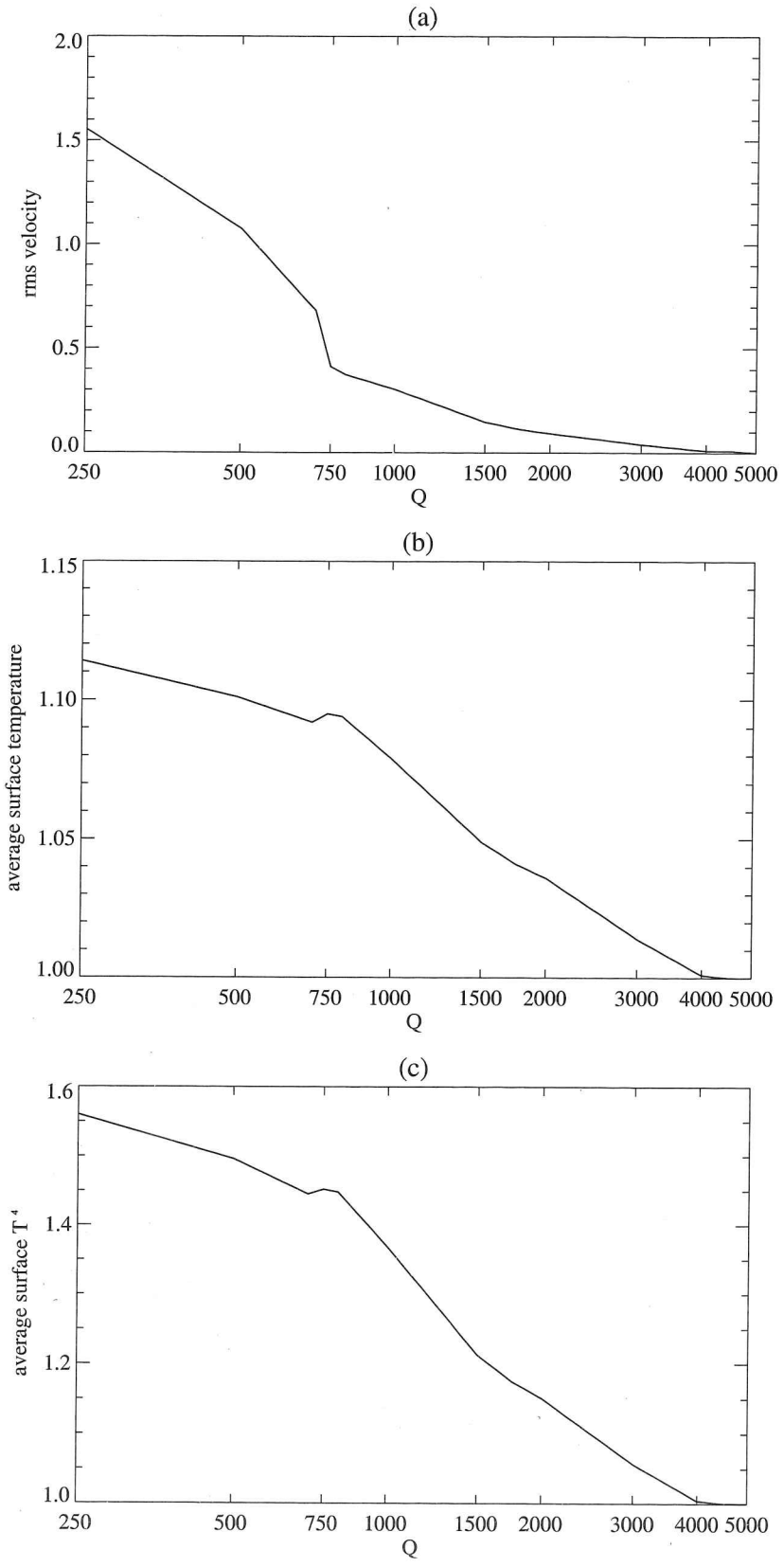

Figure 2-18. *(a) rms velocity $u_{\rm rms}$, (b) the normalized mean surface temperature $\bar{T}$, and (c) the normalized energy transport $\overline{T^4}$ as functions of Chandrasekhar number Q.*

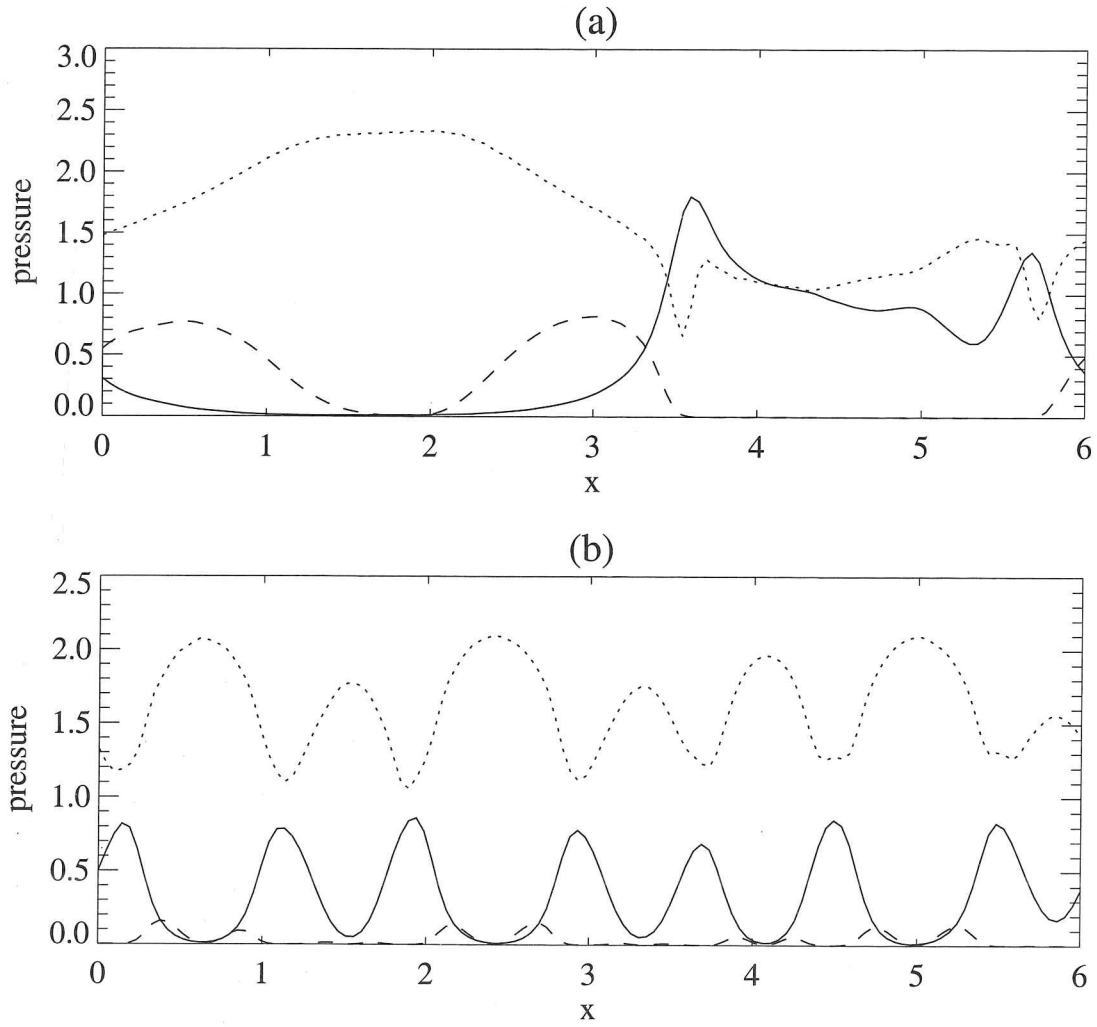

Figure 2-19. *The surface pressures ($z = 0$) at a representative instant in time for (a) $Q = 700$, and (b) $Q = 750$. The solid line is magnetic pressure P_m, the dotted line shows gas pressure P, and the dashed line gives the dynamic pressure P_d. Graph (b) is taken at the same time as the frames in Figure 2-14.*

$\frac{1}{2}\rho|\mathbf{u}|^2$ may be compared. Figure 2-19 shows a selected profile for each of the two cases $Q = 700$ and $Q = 750$ taken at the surface $z = z_0$. They demonstrate the marked change in the overall solutions that occurs as the field strength is reduced beyond the critical value corresponding to $Q \approx 730$. In Figure 2-19(a) the location of the plume is clear. In the plume the gas pressure dominates, and there is significant dynamic pressure due to the strong horizontal outflows. The remainder of the box ($3.5 < x < 5.7$) contains the flux sheet, where the gas pressure drops due to the combined reduction in both temperature and density, and the magnetic pressure is high. In contrast Figure 2-19(b) shows the more regular structure of the oscillatory plumes, where the gas and magnetic pressures are in antiphase. The dynamic pressure is comparatively small throughout the layer.

Despite the fact that a magnetohydrostatic balance is not necessarily expected, the total pressure is fairly uniform across the surface. In the flux-separated case, the maximum value of the magnetic pressure is in fact comparable to that of the gas pressure, implying that the dynamics of the flow depend on the magnetic tension as well as the magnetic pressure. In both Figure 2-19(a) and Figure 2-19(b), the dynamic pressure is small compared to the magnetic pressure, which is equivalent to saying that the field is significantly above its value at equipartition.

§2.4. *Effects of different boundary conditions*

I have obtained solutions with 'realistic' boundary conditions (2.12)–(2.14) at $z = z_0$ for other combinations of Q and λ, in addition to those already described. Figure 2-25(a) shows the various types of solution found in different regions of the (Q, λ)-parameter plane. It is clear that the sequence of transitions, from the static state to steady convection, then to spatially modulated oscillations and finally to flux separation is robust. Their order does not vary with the aspect ratio once $\lambda > 1$, although the transitions do occur at somewhat higher values of Q for $\lambda \geq 6$.

The transition from oscillations to flux separation is accompanied by a change in horizontal scale. The physical mechanism whereby narrow rolls give way to broader rolls is straightforward: once convection is strong enough for flux expulsion to occur, motion becomes more vigorous as the width of a roll increases (up to some limit that I have been unable to determine). Consider a symmetrical pair of rolls in dynamical equilibrium, with magnetic flux confined to a sheet between them. Suppose now that one roll expands slightly while the other contracts: then the expanding roll will squeeze the flux sheet to produce a stronger field, which will in turn lead to a further contraction of the smaller roll. This process can then continue until the weaker roll is eliminated. Moreover, flux transport may be facilitated if

the rising plume tilts and gives rise to shearing motion (cf. Proctor *et al.* 1994). One would expect there to be parameter values at which both the narrow-roll and the flux separated regimes are stable, as I have demonstrated.

From a mathematical point of view, one would like to associate these transitions with bifurcations from one state to another. This is feasible for solutions whose spatiotemporal structure is straightforward. Thus we can identify the initial pitchfork bifurcation from the trivial solution and the subsequent bifurcation that leads to travelling waves as Q is decreased (cf. Hurlburt *et al.* 1989). While the chaotically modulated regime that is present with weaker magnetic fields has complicated spatial and temporal structures, it is clear – at least qualitatively – that it retains a characteristic spatial scale that is much smaller than in the flux-separated regime. Neither of these two states has instantaneous spatial symmetries, but one quantitative way of characterising the difference between the two is through their time-averaged spatial periodicity. For instance, once the slow drift is removed from the data in Figure 2-11(d) ($\lambda = 6$, $Q = 750$), the time-averaged solution has wavelength 6/7, while the wavelength of the pattern with $Q = 700$ (Figure 2-5(d)) is 6, the size of the box. Techniques for measuring time-averaged symmetries have been developed by Barany, Dellnitz & Golubitsky (1993), and would be useful in more precisely determining the nature of the transitions that have been observed. In particular, it should be possible to relate the transitions between the narrow-roll and flux-separated regimes to the bifurcation structure associated with subcritical behaviour in Boussinesq magnetoconvection (cf. Proctor & Weiss 1982, Figure 31). This approach deserves further investigation.

Having ascertained the effects of varying the aspect ratio and field strength on the pattern of convection, I now go on to investigate the sensitivity of this behaviour to changes in the magnetic and thermal boundary conditions at the top of the layer.

§2.4.1. *Magnetic boundary conditions*

The obvious alternative to imposing the potential field conditions (2.12) and (2.13) is to set $B_x = \partial B_z/\partial z = 0$ at $z = z_0$, as in (2.10), while retaining the radiative condition (2.14), so that $\mathbf{B}$ is vertical at the top as well as at the bottom of the layer. Results for this choice of boundary conditions are summarized in Figure 2-25(b). Although the survey is less thorough than that in Figure 2-25(a), it is clear that the overall pattern is similar but with transitions displaced to higher values of Q. The two sets of runs for $\lambda = 6$ are contrasted in Figure 2-25. The sequences of transitions are identical, and the initial bifurcations occur very close together. However, steady solutions persist over a wider range of Q with a potential

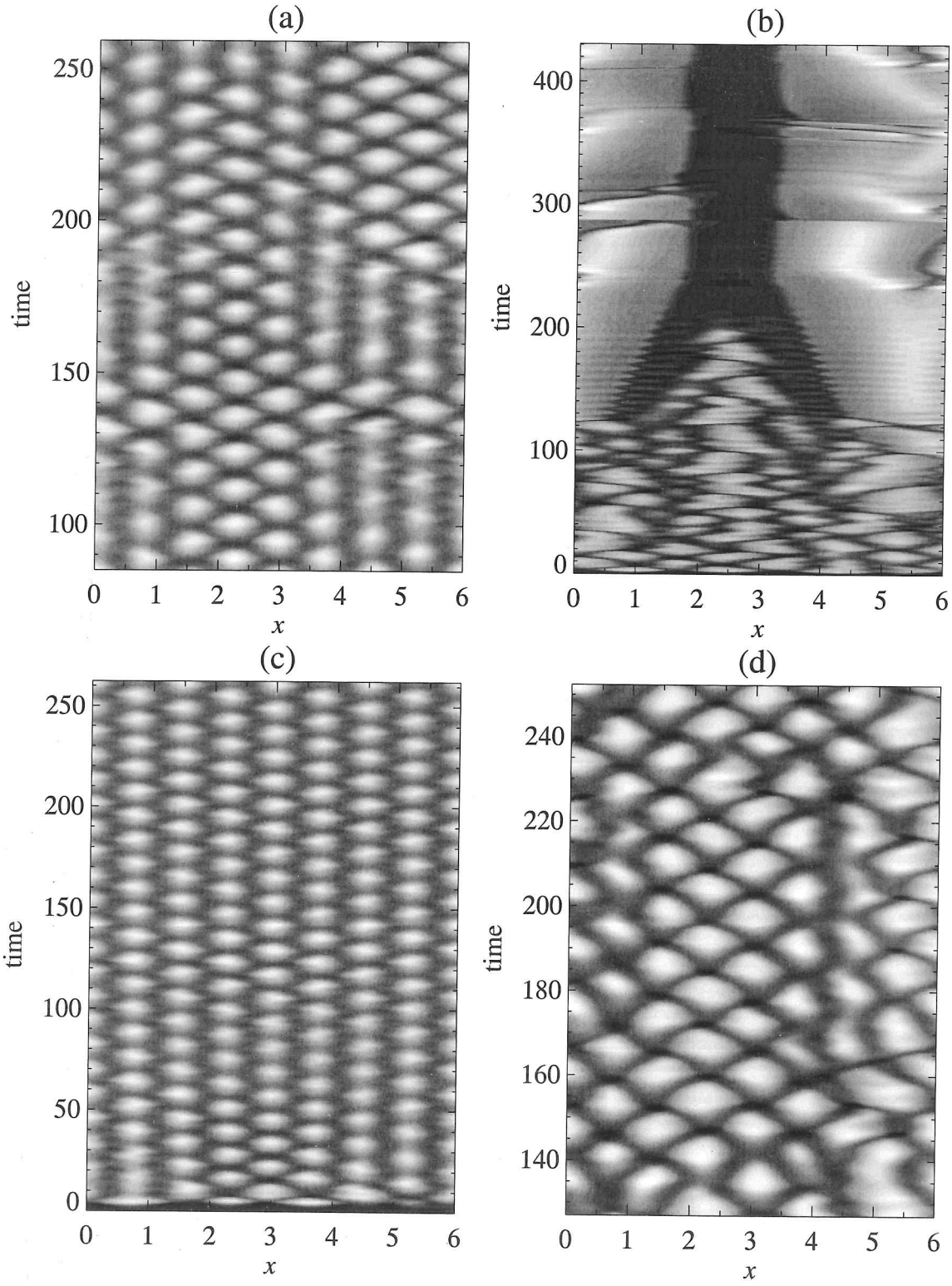

Figure 2-20. *Different magnetic boundary conditions. The surface temperature $T(x, z_0, t)$ for (a) 'realistic', (b) 'idealized', (c) 'potential', and (d) 'inverted' boundary conditions, with $\lambda = 6$ and $Q = 1000$.*
See p.50 for the definitions of these magnetic boundary conditions.

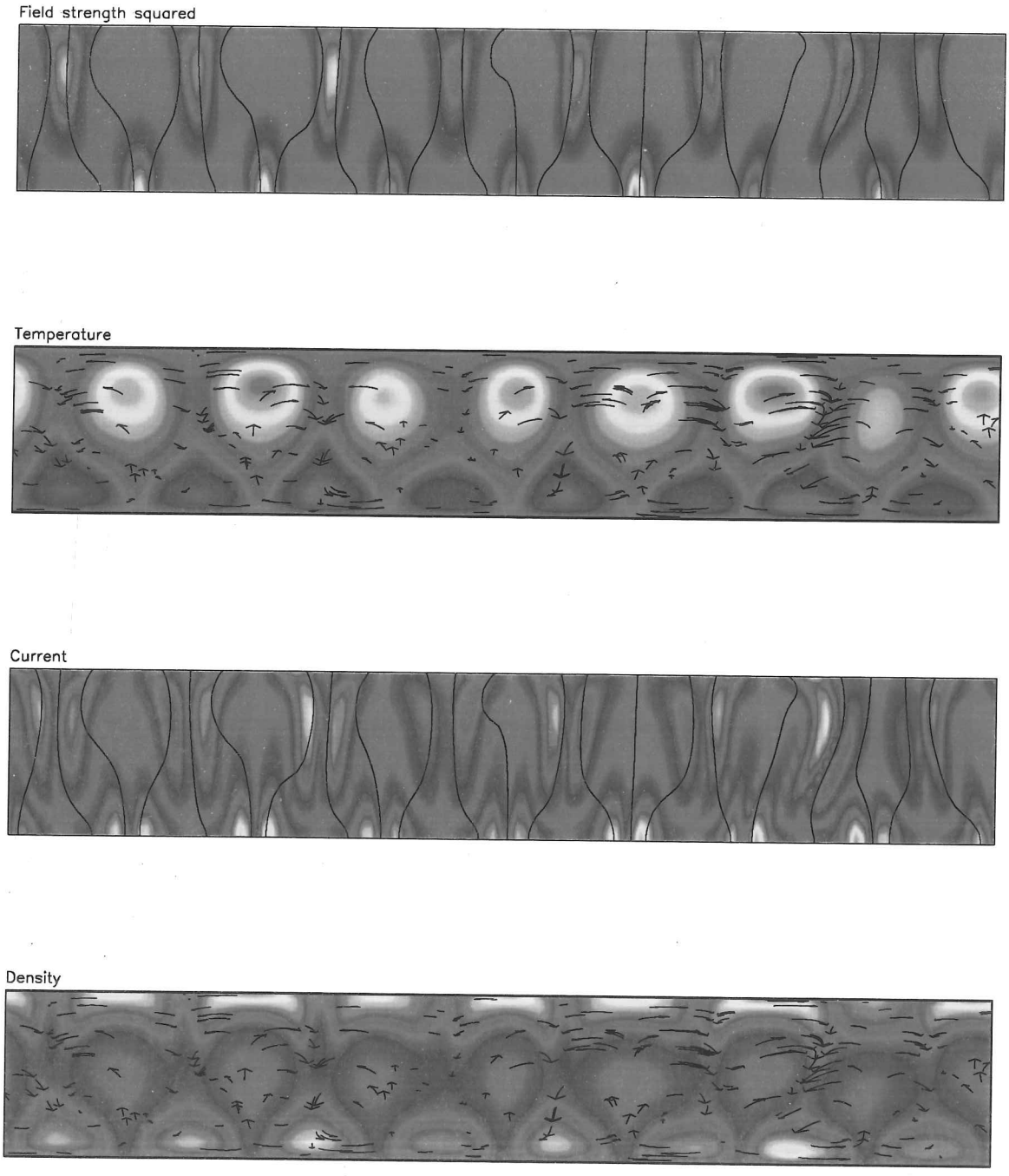

Figure 2-21. *'Realistic' magnetic boundary conditions for $Q = 1000$. Four frames taken at a single moment in time (as in Figure 2-7) showing (a) field strength with field lines, (b) temperature with velocity arrows, (c) current with field lines, (d) density with velocity arrows. The case $Q = 500$ is shown in Figure 2-7, and cases $Q = 4000, 2000, 750, 250$ in Figure 2-12–Figure 2-15.*

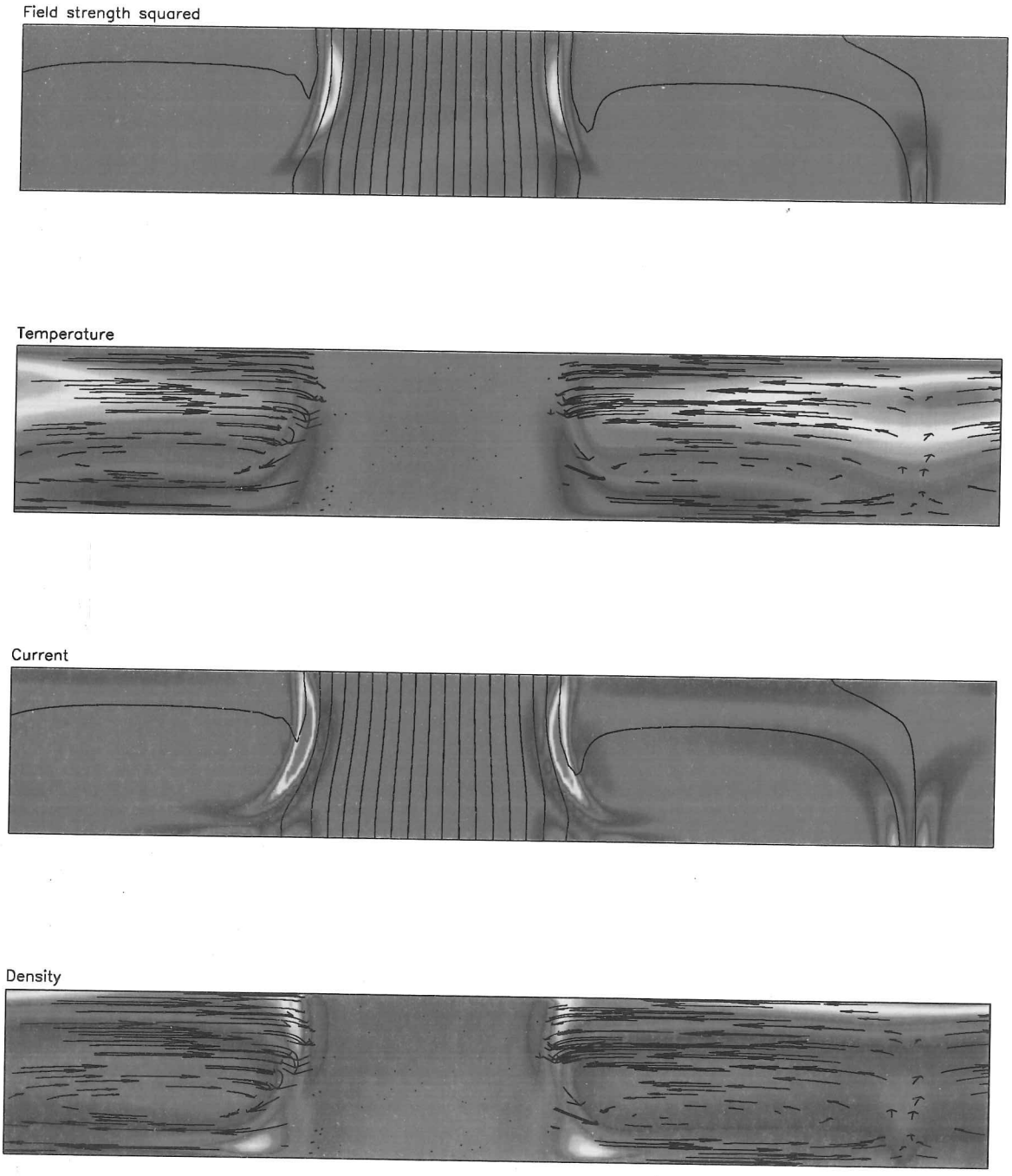

Figure 2-22. *'Idealized' magnetic boundary conditions for $Q = 1000$. We see a fairly steady flux-separated state similar to that described in §2.2.3. (see caption of Figure 2-21 for a description of the frames)*

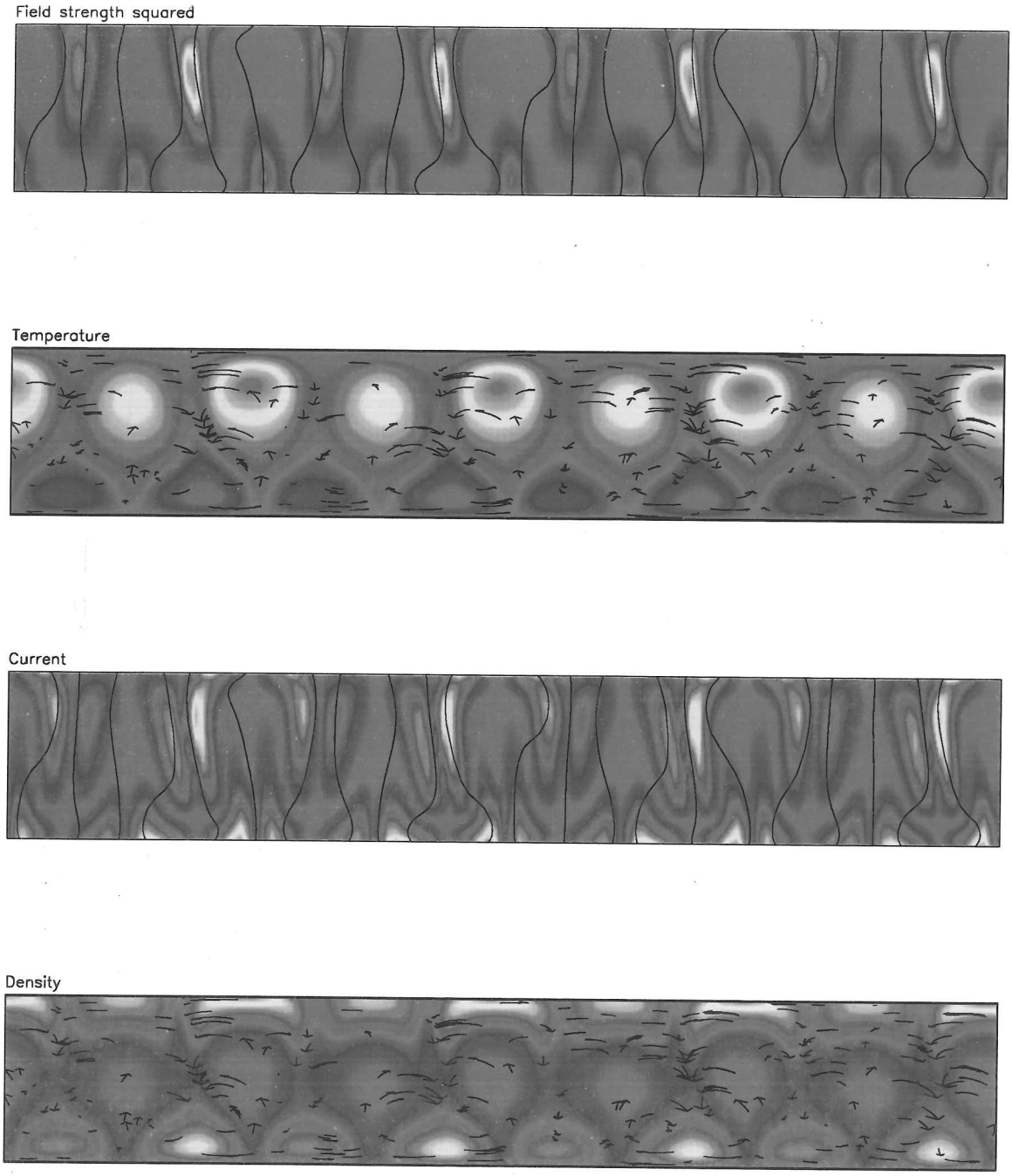

Figure 2-23. *'Potential' magnetic boundary conditions for $Q = 1000$. We see eight irregular spatially modulated oscillations similar to those in Figure 2-21. (See caption of Figure 2-21 for a description of the frames.)*

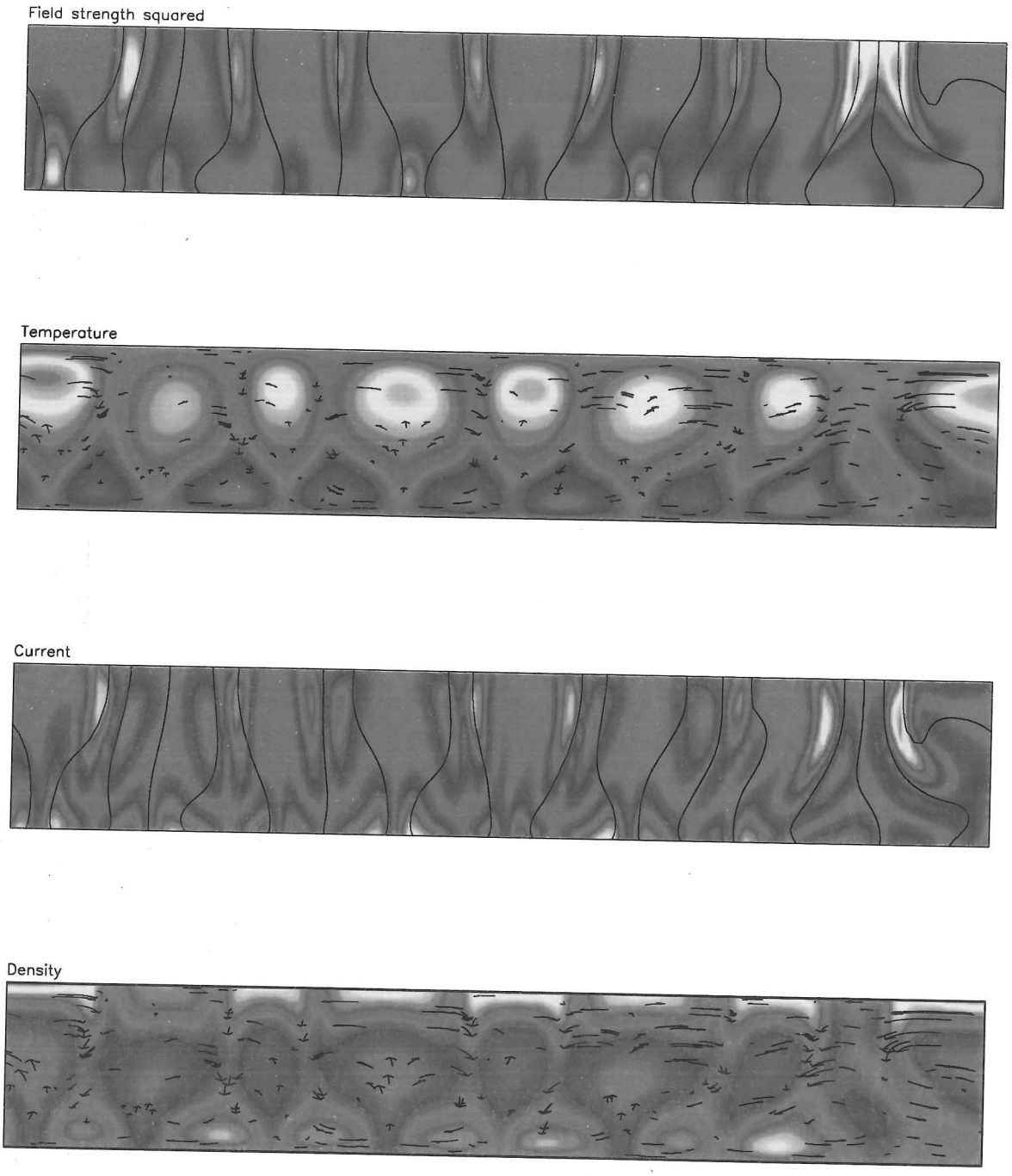

Figure 2-24. *'Inverted' magnetic boundary conditions for $Q = 1000$. Here we see seven irregular spatially modulated oscillations. (See caption of Figure 2-21 for a description of the frames.)*

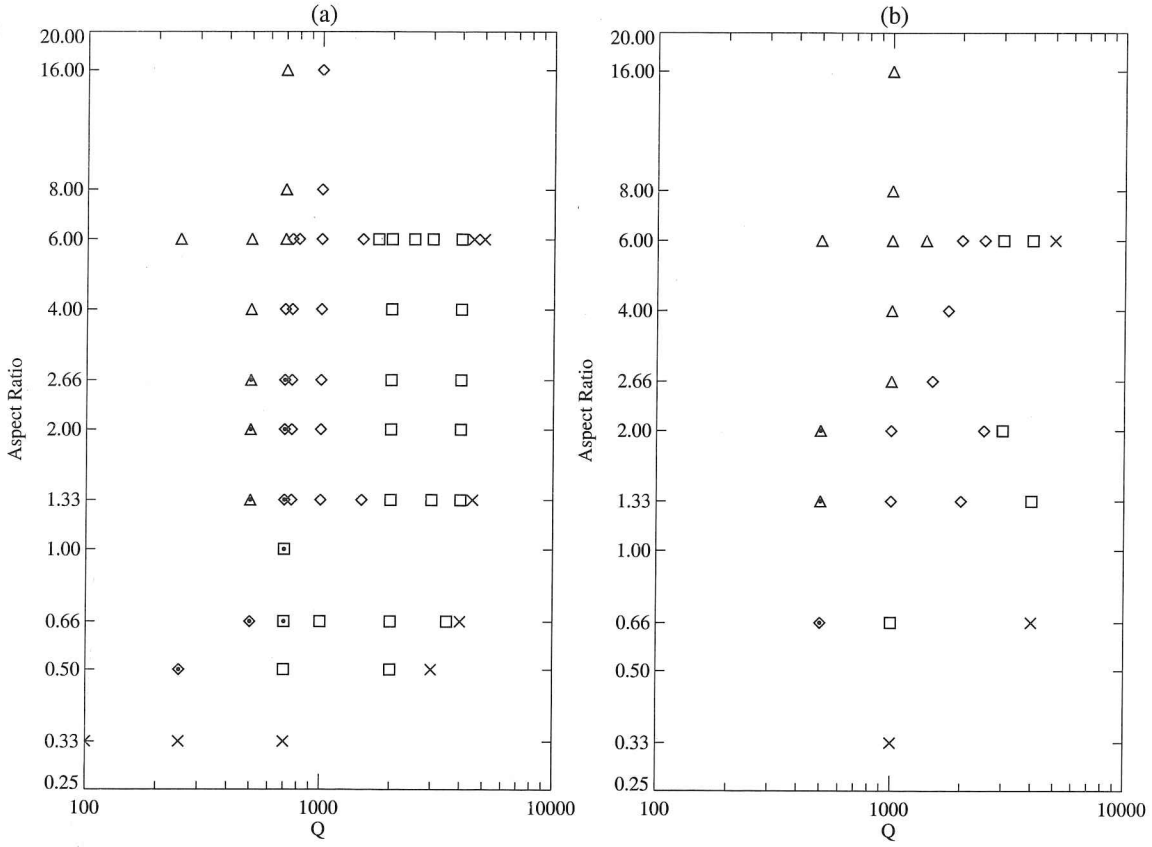

Figure 2-25. *The results of runs for various values of Q and λ with (a) 'realistic' magnetic boundary conditions (2.12)–(2.13), and (b) 'idealized' magnetic boundary conditions (2.10) at $z = z_0$. The black-body temperature boundary condition (2.14) at $z = z_0$ is used in both cases. Crosses represent the regime where no convection occurs, squares represent steady convection, diamonds represent spatially modulated oscillations, and triangles represent separation of flux. Dots within the symbols indicate that the solution is a travelling wave.*

field. Moreover, flux separation appears already at $Q = 1500$ with a vertical field, rather than at $Q = 700$ as it does with a potential field. Some quantitative differences are highlighted in Table 2.7, which gives the results of numerical experiments for $Q = 1000$ and a vertical field boundary condition at both the surface and base. Note also the differences between this and Table 2.3 in which the field was matched to a potential field at the surface, as described at length in §2.2.

The difference between the two cases is simply that, for a given value of Q, the magnetic field is less potent in Figure 2-25(b) than in Figure 2-25(a). One possible explanation is that this is due to the added restrictions on the magnetic field when constrained to be vertical at the surface. On the other hand, the potential field boundary conditions allow the Lorentz force to inhibit convection more efficiently.

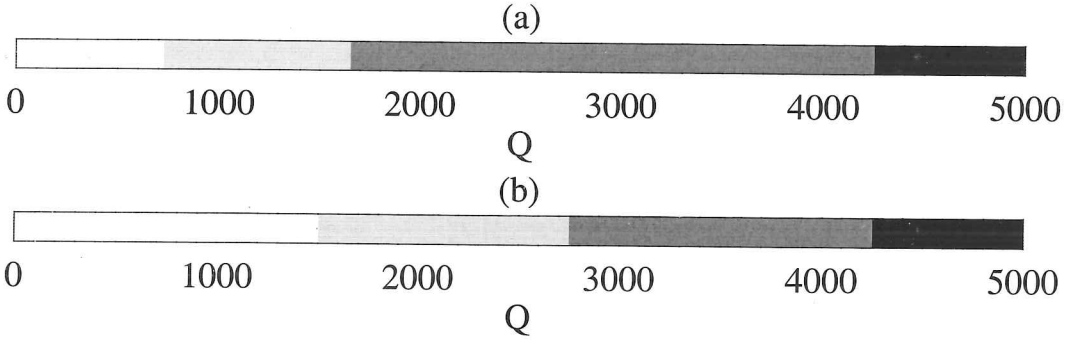

Figure 2-26. *The results of varying Q for $\lambda = 6$ with (a) 'realistic' magnetic boundary conditions (2.12)–(2.13), and (b) 'idealized' magnetic boundary conditions (2.10) at $z = z_0$. Again the black-body temperature boundary condition (2.14) at $z = z_0$ is used in both cases. Lightest shading represents flux separation, followed by spatially modulated oscillations, steady convection, and no convection.*

λ	*pattern*	n	$u_{\rm rms}$	$\bar{T}$	$\overline{T^4}$	$B_{\rm max}$
$\frac{1}{3}$	*no convection*	-	–	1.000	1.000	1.0
$\frac{2}{3}$	*steady convection*	1	0.26	1.067	1.301	6.1
$\frac{4}{3}$	*periodic oscillations*	1	0.34	1.096	1.464	11.9
2	*aperiodic oscillations*	2	0.35	1.081	1.385	12.9
$\frac{8}{3}$	*flux separation*	1	0.45	1.086	1.421	11.4
4	*flux separation*	1	0.42	1.071	1.343	13.9
6	*flux separation*	1	0.80	1.090	1.441	24.6
8	*flux separation*	1	0.74	1.069	1.335	24.4
16	*flux separation*	2	0.82	1.088	1.425	23.0

Table 2.7. *$Q = 1000$, for the 'idealized' boundary conditions. The column entries are defined in (2.17). Compare to Table 2.3, which is the case $Q = 1000$ for the 'realistic' boundary conditions.*

It is instructive to experiment with other combinations of the magnetic boundary conditions while keeping $Q = 1000$ and $\lambda = 6$. Comparing the new results with those in §2.3, I find that imposing a potential field at both the top *and* the bottom

bc's	surface	base	*pattern*	n	u_{rms}	$\bar{T}$	$\overline{T^4}$	$B_{\max}$
'realistic'	p	v	*oscillations*	8	0.30	1.079	1.369	11.1
'idealized'	v	v	*flux separation*	1	0.80	1.090	1.441	24.6
'potential'	p	p	*oscillations*	8	0.29	1.079	1.365	8.8
'inverted'	v	p	*oscillations*	7	0.36	1.084	1.402	9.7

Table 2.8. *Comparing the results for the different magnetic boundary conditions with $Q = 1000$ and $\lambda = 6$. The columns 'surface' and 'base' indicate whether the magnetic field is held vertical (v) or matched to a potential field (p), at the surface and the base respectively. The other column entries are defined in (2.17).*

has little effect. The spatially modulated oscillations are more regular and uniform, and the plumes wobble laterally as they wax and wane, reflecting the extra freedom given by a potential field. Imposing a potential field at the base with a vertical field at the top, though unphysical, has a more marked effect: the oscillating plumes demonstrate no real regularity in either space or time, being of varying size, shape and period. Their number varies between seven and eight, and the pattern of behaviour is exceedingly complex.

In order to highlight the differences, Figure 2-20 shows the surface temperature $T(x, z_0, t)$ for each of the four combinations of magnetic boundary conditions. Similarly a representative set of stills is given for each combination in Figure 2-21–Figure 2-24. Some results are given in Table 2.8.

The nomenclature used for the different combinations of magnetic boundary conditions in the figures is:

'realistic' = potential field at surface, vertical field at base;
'idealized' = vertical field at surface, vertical field at base;
'potential' = potential field at surface, potential field at base;
'inverted' = vertical field at surface, potential field at base.

§2.4.2. Thermal boundary condition

In previous studies (e.g. Weiss *et al.* 1990, 1996), the temperature was held fixed at both the surface and base. It is important to discover how those results are changed via substituting the radiative boundary condition (2.14) at the surface. Two sets of numerical experiments were thus performed in which all parameters and boundary conditions were identical, except that in one run the temperature was held constant at $z = z_0$, $z_0 + 1$, and in the other the radiative boundary condition $\frac{\partial T}{\partial z} = \theta T^4$ was imposed at $z = z_0$ (and the temperature held constant at $z = z_0 + 1$). The results of these computations demonstrate that imposing the new boundary condition has very little effect on the pattern of convection – which is not surprising, since the resulting temperature variations at the surface are comparatively small. In each case the two runs were almost identical, though the radiative boundary condition produced slightly more dynamical activity.

For comparison with earlier work, Figure 2-27 shows a time sequence from a run with $Q = 1000$ and $\lambda = 6$, with the idealized boundary conditions (2.9) and (2.10) at both boundaries. During this transient phase, there are five or six oscillating plumes of different strengths and sizes, but eventually, after a very long time, the flux separates out to leave a single plume. I comment later on the implications of this run.

§2.5. Varying the diffusivities

In the equations of magnetohydrodynamics the relative values of the diffusivities are given by the two dimensionless parameters,

$$\zeta = \frac{\eta}{\kappa}, \tag{2.19}$$

and the Prandtl number

$$\sigma = \frac{\nu}{\kappa} \tag{2.20}$$

where η, ν, and κ are the magnetic, viscous, and thermal diffusivities respectively.

As detailed in §2.1.4, ζ varies vertically and is specified by its value at the surface, ζ_0. In our case of $\zeta_0 = 0.2$, $\zeta < 1$ at the surface and $\zeta > 1$ at the base of our computational box, leading to oscillations at the surface and steady overturning convection at the base close to onset. A brief investigation into the choice of $\zeta_0 = 0.2$ and $\sigma = 1$ that was used in the previous sections was carried out on purely theoretical grounds. These values were chosen to be representative

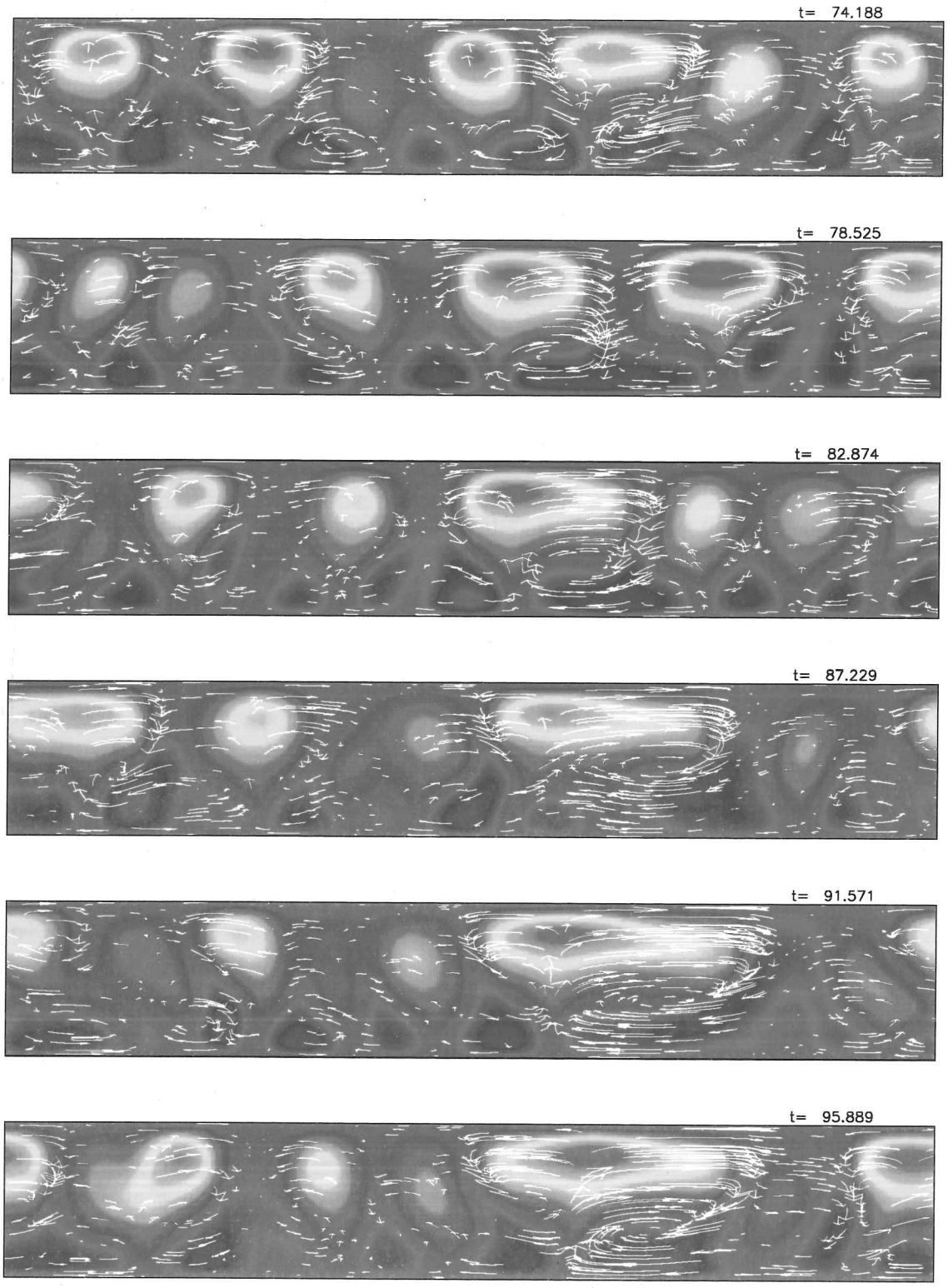

Figure 2-27. *A time sequence of images taken from a run with $Q = 1000$ and $\lambda = 6$, for the 'idealized' boundary conditions (2.9)–(2.10) at both boundaries. It shows the different scales of convection that may be obtained in a single simulation.*

of the solar photosphere and to fit with observations, and their use in §2.2–§2.4 is justified.

I experimented with altering the values of both ζ_0 and σ, investigating the results for the case $\lambda = 6$, $\hat{R} = 100\,000$, and $Q = 500$, with vertical magnetic field boundary conditions at both the surface and the base. Results are shown as plots of the surface heat flux with time in Figure 2-28, and a typical snapshot of the convection for each case is given in Figure 2-29.

The result for the familiar values $\zeta_0 = 0.2$, $\sigma = 1$ shows the flux separated state that was described in detail in §2.2. As was the case for the 'realistic' magnetic boundary conditions, the run settles to a single large convective plume and an intermediate region into which the vast majority of the magnetic field has been swept. As before, the plume splits from time to time, but in each case the single plume is soon reformed. Similarly, for $\zeta_0 = 0.2$, $\sigma = 0.1$, the overall convective pattern is dominated by the fluid flow. However the reduction in the Prandtl number, corresponding to a relatively lower viscous diffusivity, results in a solution that is effectively kinematic. The magnetic field is no longer coherent enough even to create its own region of field strength, and is tossed about violently by the strong fluid motion.

Increasing ζ_0 to 1 has a profound effect on the solution: for $\sigma = 1$, six regular, steady plumes are obtained, similar to those seen previously for higher Q (for example in Figure 2-13). Also, when σ is reduced again to 0.1, several regular plumes are again seen. However, as is clear in Figure 2-28(d), these convective cells are not in fact steady, but oscillate slightly in size. This seems to be associated with the motion of travelling waves which traverse each cell from side to side. This increase of the surface value ζ_0 to 1 causes $\zeta(z)$ to be greater than 1 throughout the layer, which in turn implies that the characteristic oscillations at the surface near onset associated with small values of ζ are no longer obtained. It is thus not surprising that much less time-dependent behaviour is observed in this case.

§2.6. *Comparison with observations*

In the previous sections, I have presented a full study of the types of convective solution that may be obtained using our two-dimensional model for different values of both the aspect ratio and the magnetic field strength, and also for various boundary conditions. I concluded that the resulting patterns depend critically on the aspect ratio of the box λ, and that solutions can be limited greatly if the aspect ratio is too small. In their studies of fully compressible two-dimensional magnetoconvection, Weiss *et al.* (1990) discovered the change from a steady solution to spatially

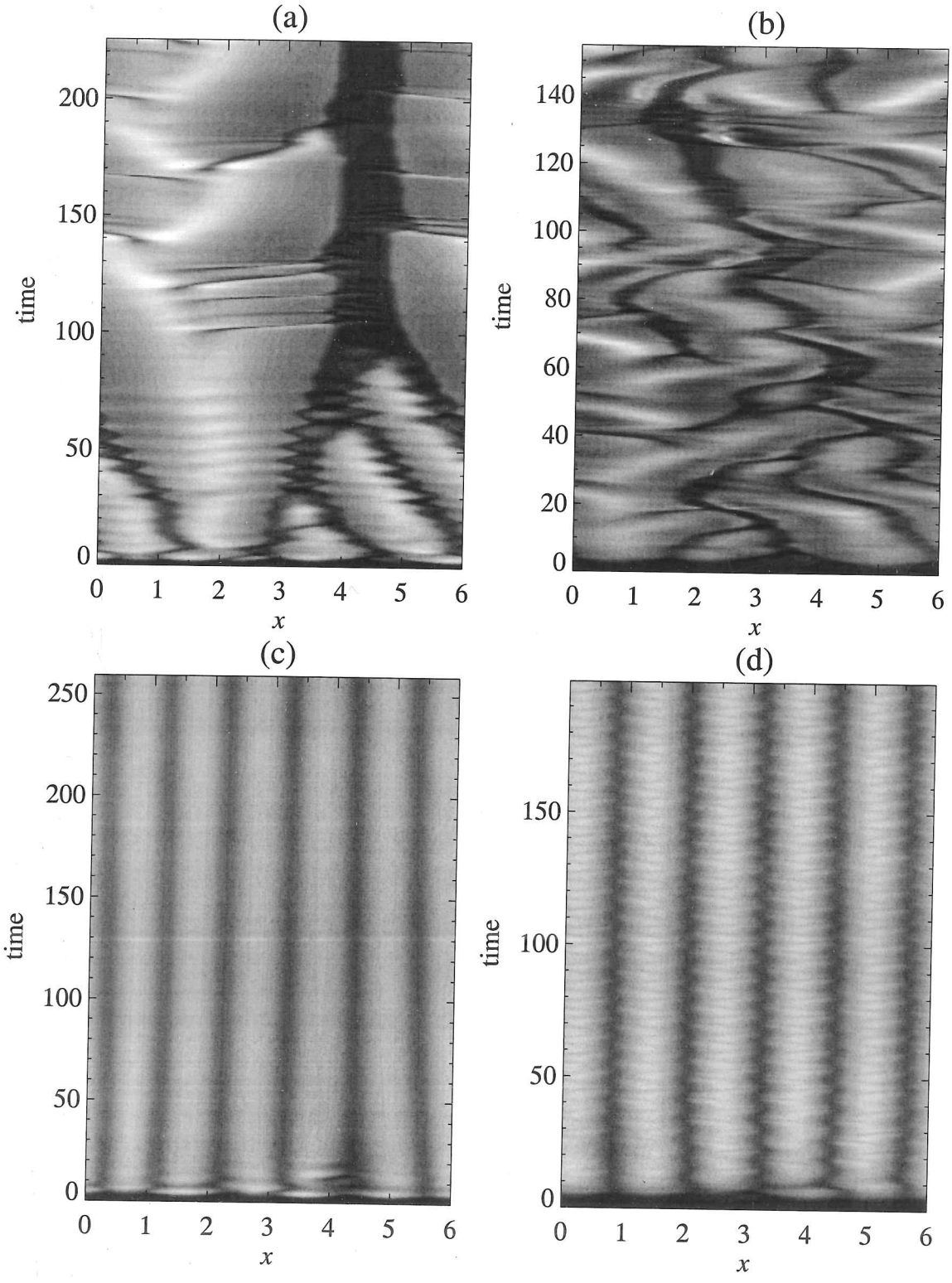

Figure 2-28. *Surface temperature shown as a function of time, for* $\hat{R} = 100\,000$, $Q = 500$ *and (a)* $\sigma = 1$, $\zeta_0 = 0.2$; *(b)* $\sigma = 0.1$, $\zeta_0 = 0.2$; *(c)* $\sigma = 1$, $\zeta_0 = 1.0$; *(d)* $\sigma = 0.1$, $\zeta_0 = 1.0$.

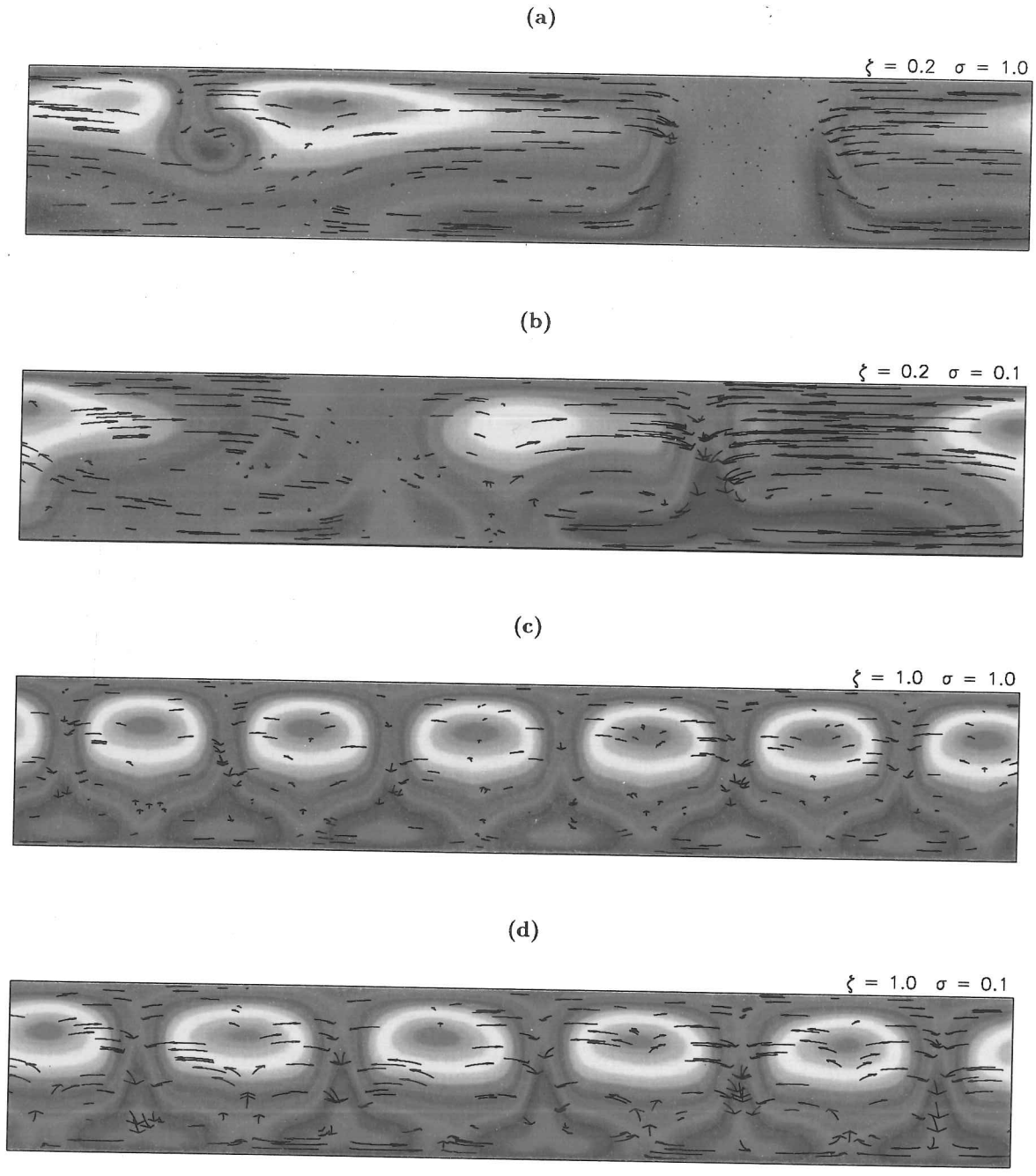

Figure 2-29. *Typical snapshots of the solutions obtained for* $\hat{R} = 100\,000$, $Q = 500$ *and (a)* $\sigma = 1$, $\zeta_0 = 0.2$, *(b)* $\sigma = 0.1$, $\zeta_0 = 0.2$, *(c)* $\sigma = 1$, $\zeta_0 = 1.0$, *(d)* $\sigma = 0.1$, $\zeta_0 = 1.0$

modulated oscillations as λ is increased, so it was expected that this would be repeated with the new radiative temperature boundary condition (2.14). However, I also located a pattern of convection in which the magnetic flux is swept into a single region of the box, leading to an entirely new phenomenon – the formation of a large, isolated plume. Furthermore, as shown in §2.3, there exists a parameter range in which both flux separation and spatially modulated oscillations of several cells are stable. This result could have important consequences in solar studies, suggesting that isolated flux tubes may be able to remain intact when they are introduced into regions of small-scale convection.

Our studies of magnetoconvection are motivated by attempts to model the solar photosphere in ever greater detail and to explain the observations of increasingly high resolution. At this stage our models give no real quantitative results, but give many important clues as to the sorts of qualitative behaviour that may be expected in current photospheric observations.

The greatest range of convective behaviour is observed in sunspots, and it is here that magnetic fields play their most important roles in influencing the patterns of convection. It is now established that umbral dots are a convective phenomenon (Lites *et al.* 1991). Current observations (Rimmele 1997) have detected periodic variation in the brightness of some large umbral dots with periods of around 20 minutes. Rimmele also measured relatively low upward velocities and found no discernible variation in the magnetic field strength. These observations are all consistent with theoretical studies of spatially modulated oscillations (Weiss *et al.* 1990), as seen in our model. High resolution studies of sunspots (eg Sobotka 1997) show that there is no typical size for umbral dots and that they exist on all scales from $8''$ down to the limit of resolution of $0''.28$, as shown in Figure 2-30. Our studies have confirmed that such a range of scales is possible if the aspect ratio is sufficiently large, as is seen in Figure 2-27.

Sunspots also contain dark nuclei in which no convective activity is seen. These correspond to regions where the magnetic field is almost vertical and the field strength is at its greatest (Stanchfield, Lites & Thomas 1997). It is likely that dark nuclei occur as the result of flux separation, being regions of high field strength and very weak convection as was seen in §2.2.3. Similarly, plages may represent some form of flux separation. Observations show smaller scale convection within strong fields beside field-free regions, as may be seen in our results such as Figure 2-6(b).

The persistence of plage regions, as local flux concentrations with abnormal granulation, is another example of flux separation. Here, the stronger fields allow

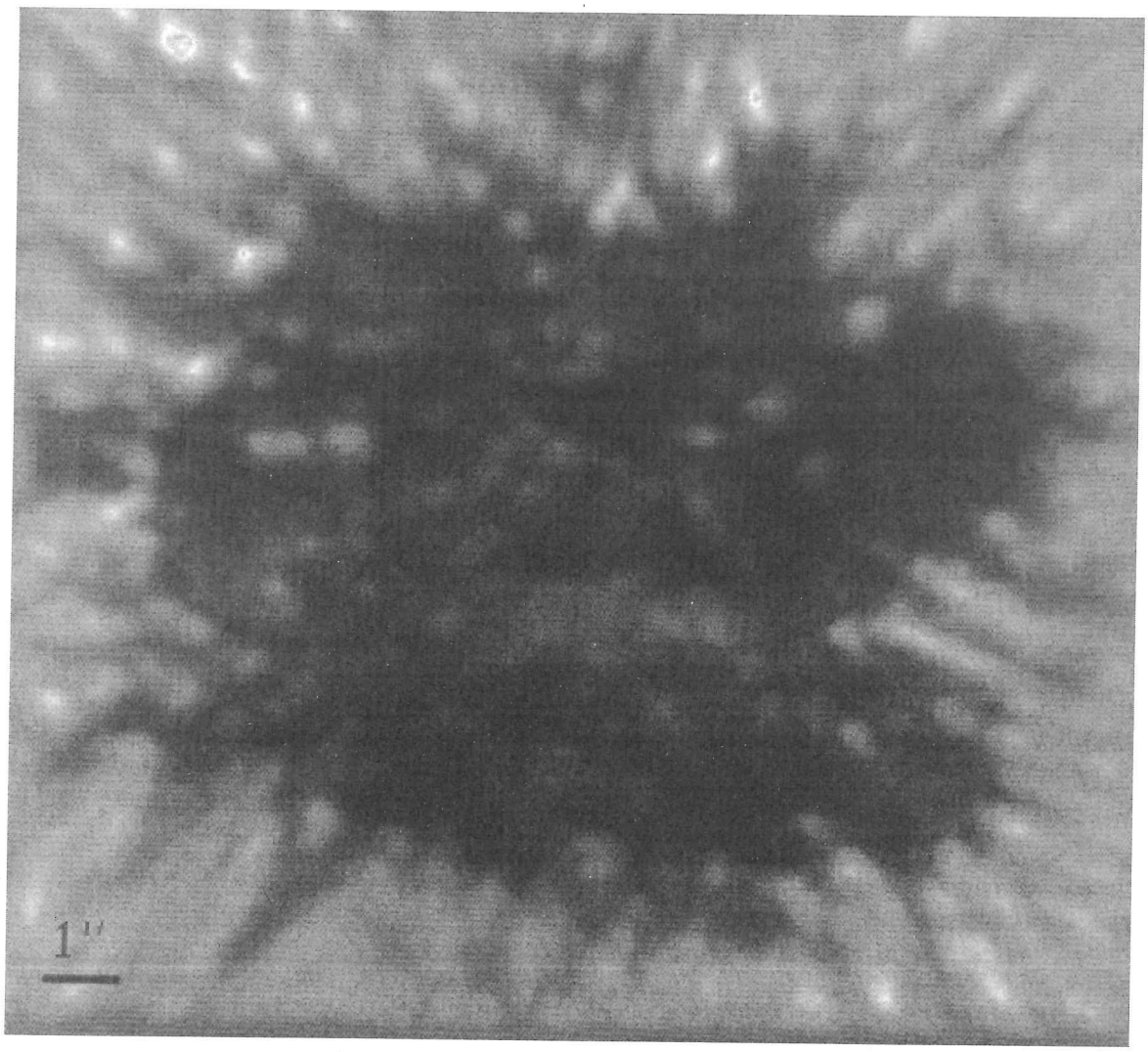

Figure 2-30. *The umbra of a sunspot, showing the range of scales of umbral dots. Note also the dark nucleus and a faint granular light bridge. SVST, La Palma (from Sobotka 1997).*

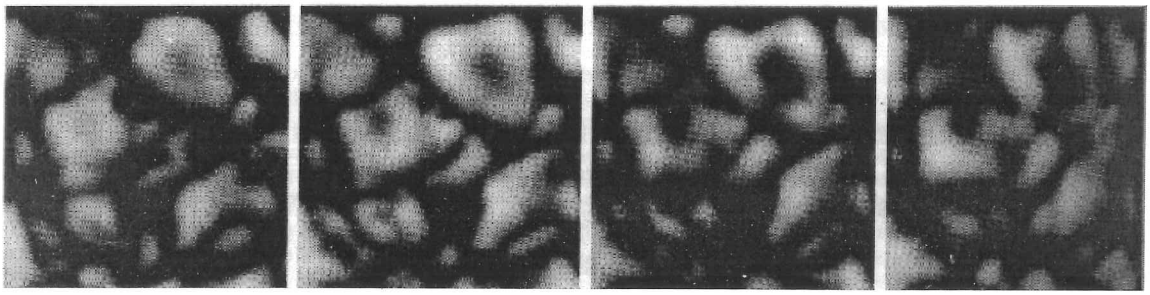

Figure 2-31. *A time sequence showing an exploding granule. Shown are images of the solar photosphere continuum taken at 1 minute intervals. The field of view is 7″ × 7″ (From Foukal 1990).*

a modified form of convection, with smaller plumes than in the ambient field-free photosphere. An idealized version of this behaviour appears in some of my runs, which show small-scale spatially modulated oscillations adjacent to broad convective plumes (eg Figure 2-6(b)). In my calculations, flux separation is associated with splitting of the field-free plumes, as illustrated in Figure 2-8. The key feature of this process is the appearance of a downflow near the centre of the plume, as a result of buoyancy braking (Spruit *et al.* 1990). What happens next depends on the imposed geometry: with imposed axial symmetry the reversed flow remains on the axis (Steffen *et al.* 1989), while in my studies the downflows move outwards.

Repeated observations of the photosphere over short periods of time show what are known as exploding granules (Rast *et al.* 1993, Rast 1995), as shown in Figure 2-31. Some previous numerical simulations in three dimensions show similar behaviour to that seen on the Sun (Nordlund 1985, Spruit *et al.* 1990). The splitting of the field-free plumes associated with flux separation seen in Figure 2-8 is the two-dimensional analogue of these results and the sizes of field-free plumes are limited by this process.

Light bridges are effectively two-dimensional phenomena and observations have confirmed that they are convective (Rimmele 1997). Fields less than $1kG$ allow comparatively large granules to form, whose intensity varies slightly with a period of around 30 minutes. This is again consistent with the behaviour of spatially modulated oscillations and a light bridge could be modelled by a fairly narrow box such as in Figure 2-3(c).

It is clear that two-dimensional studies are limited in their application to photospheric magnetoconvection, and that a much greater understanding must come from taking the step up to three dimensions. Our studies have demonstrated that such computations must be carried out in boxes of sufficiently large aspect ratio, a task that is still computationally extremely expensive. However, some calculations

have been performed and demonstrate that the three-dimensional equivalent of flux separation does indeed still occur for the cases $\lambda = 4$ and $\lambda = 8$ (Tao *et al.* 1998), giving rise to a much more complicated variety of behaviour than in two dimensions. As will be shown in Chapter 5, the majority of convective patterns found in two dimensions have analogues that can still be located in three dimensions, yet the added complexity and freedom of the extra spatial dimension makes the investigation and classification of such patterns a daunting task. There is indeed much to be learned from studying two-dimensional convection that may be carried forward to later more realistic studies.

Chapter 3.

A truncated model

Before the advent of computers, mathematicians wishing to study solutions of the equations of convection were forced to resort to restrictive analytic methods, the complexity of the full partial differential equations proving to be prohibitive in many cases. One method of analysing such a complicated set of equations is to derive a low-order set of ordinary differential equations through harmonic expansions in the spatial variables and truncation of these expansions. Even now, with computer power ever on the increase, the study of dynamical systems is sufficiently advanced that such a method may still prove extremely useful, and careful investigations of the bifurcation sequence of the equations may be carried out.

Early studies of low-order models for convection began with the Lorenz equations in 1963, but such a low order truncation proved too restrictive (Moore & Weiss 1973). Thermosolutal convection was the next area of investigation and Veronis (1965) derived a fifth-order model, with equivalent models being derived for convection in an imposed vertical magnetic field later (Knobloch *et al.* 1981). It has been shown that all such fifth-order models possess a Takens-Bogdanov bifurcation point and can be reduced to the Van der Pol equation as an asymptotically correct second-order model (Knobloch & Proctor 1981). Proctor & Weiss (1990) extended this analysis to a fourth-order set of ODEs in the limit of tall, thin rolls.

Up until now research has concentrated mainly on narrow boxes, which is known to restrict the behaviour to a large extent. Moreover, following the results in Chapter 2, it is desirable to understand the mechanisms that lead to the new phenomenon of flux separation, and what causes the abrupt change in the scale of convection. In order to do this I derive a low-order model in which the equations of magnetoconvection are truncated to only one or two modes in the vertical direction and study the five resulting partial differential equations to try to reproduce some

of the behaviour observed in Chapter 2. This exploits the fact that the vertical behaviour of the results of Chapter 2 was relatively simple, whilst attempts to reproduce the 'flux-separated' states of §2.2.3 require full horizontal resolution. The reduction in computational complexity that this entails has allowed a full sweep of parameter space, whilst retaining the key features of the problem, and I report upon a wide range of convective behaviour. In particular, I investigate examples of further 'flux-separated' states, and find a fundamental new type of fully-isolated convective state. Some of the results in this Chapter are also presented in my recent paper (Blanchflower 1999).

§3.1. *Derivation of the model*

Once again I attempt to model magnetoconvection of a perfect monatomic gas in a two-dimensional rectangular box of aspect ratio λ. This time the Boussinesq approximation is adopted ($\nabla.\mathbf{u} = 0$, $\rho/\rho_0 = 1 - \alpha(T - T_0)$ in the buoyancy term and $\rho = \rho_0$ elsewhere) forcing the redefinition several variables. Using the standard convention for a Boussinesq fluid it is necessary to relabel the coordinates such that the box now occupies the region $\{0 \leq x \leq \lambda;\ 0 \leq z \leq 1\}$, where $z = 0$ at the *base* of the box and increases upwards.

The two-dimensional equations of magnetoconvection under the standard Boussinesq approximation, with a uniform vertical background magnetic field, are (Knobloch *et al.* 1981)

$$\begin{aligned}
\frac{\partial \omega}{\partial t} + \frac{\partial(\psi,\omega)}{\partial(x,z)} &= \sigma\nabla^2\omega - \sigma R\frac{\partial\theta}{\partial x} - \sigma\zeta Q\left(\frac{\partial\nabla^2 A}{\partial z} + \frac{\partial(A,\nabla^2 A)}{\partial(x,z)}\right) \\
\frac{\partial \theta}{\partial t} + \frac{\partial(\psi,\theta)}{\partial(x,z)} &= \nabla^2\theta + \frac{\partial\psi}{\partial x} \\
\frac{\partial A}{\partial t} + \frac{\partial(\psi,A)}{\partial(x,z)} &= \zeta\nabla^2 A + \frac{\partial\psi}{\partial z}
\end{aligned} \tag{3.1}$$

where the Jacobian

$$\frac{\partial(f,g)}{\partial(x,z)} = \frac{\partial f}{\partial x}\frac{\partial g}{\partial z} - \frac{\partial f}{\partial z}\frac{\partial g}{\partial x}. \tag{3.2}$$

where θ is defined via

$$T = T_0 + \theta, \quad (T_0 = 1 - z). \tag{3.3}$$

A is the magnetic flux function,

$$\mathbf{B} = \mathbf{B_0} + \nabla \wedge (0, A, 0) = \left(-\frac{\partial A}{\partial z}, 0, 1 + \frac{\partial A}{\partial x} \right) \tag{3.4}$$

(where $\mathbf{B_0} = (0, 0, 1)$ is the uniform vertical field), and ψ is the stream function satisfying

$$\mathbf{u} = \nabla \wedge (0, \psi, 0) = \left(-\frac{\partial \psi}{\partial z}, 0, \frac{\partial \psi}{\partial x} \right) \tag{3.5}$$

The vorticity is also defined,

$$\Omega = \nabla \wedge \mathbf{u} = (0, \omega, 0) = (0, -\nabla^2 \psi, 0) \tag{3.6}$$

The coordinates x and z have been scaled by the depth of the box d and time t has been scaled by the thermal conduction time d^2/κ, where κ is the thermal diffusivity. A fixed temperature difference ΔT is maintained across the layer. Again the Rayleigh number R is used which in this case is

$$R = \frac{g\alpha \Delta T d^3}{\kappa \nu} \tag{3.7}$$

and the Chandrasekhar number Q is now defined as

$$Q = \frac{B_o^2 d^2}{\mu_0 \rho_0 \eta \nu}. \tag{3.8}$$

$\zeta = \eta/\kappa$, the ratio of the magnetic and thermal diffusivities, and is held constant. All other quantities were defined in §2.

As usual, the surface and base of our box are impermeable but slippery, on which the normal component of the velocity and the tangential component of the viscous stress both vanish. Moreover, for simplicity I impose the 'idealized' magnetic boundary condition that the field is held vertical at both the upper and lower boundary. Such boundary conditions allow us harmonic eigenfunctions. These give:

$$\psi = \omega = \theta = \frac{\partial A}{\partial z} = 0 \quad \text{at } z = 0, 1 \tag{3.9}$$

It is clear that equations (3.1) have a static conducting solution satisfying

$$\theta = \psi = \omega = A = 0, \tag{3.10}$$

corresponding to a stationary fluid with an imposed, uniform, vertical magnetic field. As before, all quantities are constrained to be periodic in the x-direction, with period λ.

Following this and in order to satisfy the above boundary conditions (3.9), I expand each of the variables in the vertical direction as a Fourier sum. I truncate the series and retain the appropriate modes as in the fifth order 'Lorenz system' (Lorenz 1963, Knobloch *et al.* 1981):

$$\begin{aligned} \omega &= \omega_1(x,t)\sin\pi z \\ \psi &= \psi_1(x,t)\sin\pi z \\ \theta &= \theta_1(x,t)\sin\pi z + \theta_2(x,t)\sin 2\pi z \\ A &= A_0(x,t) + A_1(x,t)\cos\pi z \end{aligned} \tag{3.11}$$

Each of these five modes is required to retain consistency of the expansion. Moreover, the appearance of a constant mode A_0 is required if we are to attempt to reproduce some of the behaviour observed in earlier sections, most notably the 'flux separated' states, as without the A_0 mode the total magnetic flux at any value of x is constant, due entirely to the imposed uniform vertical field $\mathbf{B_0}$.

These expansions are substituted into the equations (3.1) and projected onto the different vertical modes to give five partial differential equations governing the evolution of each of the modes.

$$\begin{aligned} \frac{\partial\omega_1}{\partial t} &= \sigma(\omega_1'' - \pi^2\omega_1) - \sigma R\theta_1' - \sigma\zeta Q\pi\left((1+A_0')(\pi^2 A_1 - A_1'') + A_0'''A_1\right) \\ \frac{\partial\theta_1}{\partial t} &= \theta_1'' - \pi^2\theta_1 + \psi_1' + \pi\psi_1'\theta_2 + \frac{\pi\psi_1\theta_2'}{2} \\ \frac{\partial\theta_2}{\partial t} &= \theta_2'' - 4\pi^2\theta_2 + \frac{\pi\psi_1\theta_1'}{2} - \frac{\pi\psi_1'\theta_1}{2} \\ \frac{\partial A_0}{\partial t} &= \zeta A_0'' + \frac{\pi\psi_1 A_1'}{2} + \frac{\pi\psi_1' A_1}{2} \\ \frac{\partial A_1}{\partial t} &= \zeta(A_1'' - \pi^2 A_1) + \pi\psi_1 + \pi\psi_1 A_0' \end{aligned} \tag{3.12}$$

with $\omega_1 = -(\psi_1'' - \pi^2\psi_1)$. Primes indicate partial differentiation with respect to x.

These are solved using a pseudo-spectral method in x, and a second-order Adams-Bashforth scheme for timestepping. The horizontal resolution is varied according to the aspect ratio, but 32 mesh intervals proves to be sufficient in the majority of cases.

§3.2. *Linear Theory*

Before I solve the model derived above it is useful to first obtain several key results from linear theory (Chandrasekhar 1961). The linear stability problem is studied by further truncating the expansion (3.11) in the horizontal direction, using the fifth order truncation:

$$\begin{aligned} \psi &= a(t) \sin \alpha x \sin \pi z \\ \theta &= b(t) \cos \alpha x \sin \pi z + c(t) \sin 2\pi z \\ A &= e(t) \sin 2\alpha x + d(t) \sin \alpha x \cos \pi z \end{aligned} \tag{3.13}$$

For a solution with m pairs of rolls in the box, $\alpha = \frac{2m\pi}{\lambda}$ where λ is the usual aspect ratio.

Substitution into (3.1) results in an equation for the evolution of each of these modes, which were first given in Knobloch *et al.* (1981).

$$\begin{pmatrix} \dot{a} \\ \dot{b} \\ \dot{c} \\ \dot{d} \\ \dot{e} \end{pmatrix} = \mathbf{L} \begin{pmatrix} a \\ b \\ c \\ d \\ e \end{pmatrix} + \mathbf{n} \tag{3.14}$$

where the linear and nonlinear terms are given by

$$\mathbf{L} = \begin{pmatrix} -\frac{\sigma\pi^2}{\lambda^2}(\lambda^2 + 4m^2) & \frac{2\sigma R m \lambda}{\pi(\lambda^2+4m^2)} & 0 & -\sigma\zeta Q\pi & 0 \\ \frac{2m\pi}{\lambda} & -\frac{\pi^2}{\lambda^2}(\lambda^2 + 4m^2) & 0 & 0 & 0 \\ 0 & 0 & -4\pi^2 & 0 & 0 \\ \pi & 0 & 0 & -\frac{\zeta\pi^2}{\lambda^2}(\lambda^2 + 4m^2) & 0 \\ 0 & 0 & 0 & 0 & -\frac{16\zeta m^2\pi^2}{\lambda^2} \end{pmatrix} \tag{3.15}$$

$$\mathbf{n} = \frac{m\pi^2}{\lambda} \begin{pmatrix} \frac{2\zeta Q\pi^2}{\lambda^2}(12m^2 - \lambda^2)de \\ 2ac \\ ab \\ -2ae \\ ad \end{pmatrix} \tag{3.16}$$

respectively. To find where the primary bifurcations occur, it is easiest to linearise by ignoring $\mathbf{n}$. It is clear that, after linearising, c and e will play no part in determining the location of any bifurcations, so only the 3×3 submatrix of a, b & d is considered.

Usually in magnetoconvection, systems such as I am considering here are studied by holding Q fixed and varying R. An equivalent approach, more appropriate for my investigations, is to hold R fixed and instead to vary Q. I shall begin by giving the results for both methods, but will then concentrate solely on the latter method.

A pitchfork bifurcation to a solution consisting of m pairs of steady rolls occurs when the linear (3×3 sub-) matrix of (3.14) has a zero eigenvalue. For the case where Q is held fixed this is at

$$R_m^{(e)} = \frac{\pi^4}{4m^2\lambda^4}(4m^2+\lambda^2)^3 + \frac{\pi^2}{4m^2}(4m^2+\lambda^2)Q \tag{3.17}$$

or inverting this to give the result for the case where Q is varied gives

$$Q_m^{(e)} = \frac{4m^2}{\pi^2(4m^2+\lambda^2)}R - \frac{\pi^2}{\lambda^4}(4m^2+\lambda^2)^2 \tag{3.18}$$

Similarly, a Hopf bifurcation to m oscillatory cells occurs when the same matrix has purely imaginary eigenvalues. For the two cases described above, this happens respectively at

$$R_m^{(o)} = \frac{\pi^2(\sigma+\zeta)}{4m^2\lambda^4}(4m^2+\lambda^2)\left(\frac{\pi^2(1+\zeta)}{\sigma}(4m^2+\lambda^2)^2 + \frac{\zeta\lambda^4}{(1+\sigma)}Q\right) \tag{3.19}$$

provided that $\zeta < 1$ and $Q > Q_c$ where

$$Q_c = \frac{\zeta(1+\sigma)}{\sigma(1-\zeta)}\frac{\pi^2}{\lambda^4 m^2}(4m^2+\lambda^2)^2 \tag{3.20}$$

and

$$Q_m^{(o)} = \frac{(1+\sigma)}{\zeta\pi^2\lambda^4(4m^2+\lambda^2)}\left(\frac{4m^2\lambda^4}{(\sigma+\zeta)}R - \frac{(1+\zeta)\pi^4}{\sigma}(4m^2+\lambda^2)^3\right) \tag{3.21}$$

provided that $\zeta < 1$ and $R > R_c$ where

$$R_c = \frac{\sigma+\zeta}{\sigma(\zeta-1)}\frac{\pi^4}{4m^2\lambda^4}(4m^2+\lambda^2)^3 \tag{3.22}$$

R	1	2	3	4	5	6	7	8
5000	*38.5*	*135.3*	213.8	248.1	231.7	158.6	18.1	-
	653	2381	3737	**4220**	3674	1941	-	-
10000	*89.1*	*291.2*	467.1	572.3	604.2	563.8	446.1	239.0
	1574	5215	8342	10115	**10447**	9309	6546	1866
20000	*190.5*	*602.9*	973.7	1220.8	1349.2	1374.4	1302.1	1127.3
	3416	10884	17554	21905	23992	**24047**	22109	18017
50000	*494.4*	*1538.2*	2493.6	3166.1	3584.2	3806.1	3870.1	3792.2
	8943	27889	45187	57275	64629	68260	**68800**	66469
100000	*1001.0*	*3097.0*	5026.6	6408.4	7309.2	7859.0	8150.0	8233.6
	18154	56230	91242	116226	132357	141948	146617	**147223**

Table 3.1. $\lambda = 6$, $\zeta = 0.1$, $\sigma = 1$. *Each value of the Rayleigh number R considered has two rows. The first row gives the value of the Chandrasekhar number $Q_m^{(e)}$ at which the bifurcation to m pairs of steady rolls occurs for $m = 1 \ldots 8$. The second row gives the corresponding positions of the Hopf bifurcations $Q_m^{(o)}$. In each case $Q_{max}^{(o)}$ is given in bold, and any bifurcations that are subcritical close to the bifurcation point are italicised. No entry implies that the mode does not exist for any positive Q.*

So for the case $\zeta > 1$ (or $\zeta < 1$, $R < R_c$) overstability never occurs and convection begins at a pitchfork bifurcation. For the case when R is being held constant and Q is decreased from infinity, this will occur at the maximum value $Q_{max}^{(e)}$ of $Q_m^{(e)}$ as m ranges over the positive integers. If $\zeta < 1$ and $R > R_c$ then the maximum value $Q_{max}^{(o)}$ of $Q_m^{(e)}$ will satisfy $Q_{max}^{(o)} > Q_{max}^{(e)}$ and the onset of convection occurs as overstability at the Hopf bifurcation at $Q = Q_{max}^{(o)}$.

Similarly, for the case when Q is held constant and R increased from zero, there is a transfer of stability to steady convection if $\zeta > 1$ or if $\zeta < 1$ and $Q < Q_c$, occuring at $R_{min}^{(e)}$. Finally oscillatory convection will occur first (at $R_{min}^{(o)}$) if $\zeta < 1$.

From here on, apart from §3.3.1 in which the model is tested against existing results, I will assume that R is being held fixed, while Q is is taken as the fundamental variable, and in the analysis of the next section only this case will be considered.

λ	1	2	3	4	5	6	7	8	15
1	1374	–	–	–	–	–	–	–	–
	24047	–	–	–	–	–	–	–	–
2	974	1374	837	–	–	–	–	–	–
	17554	**24047**	11447	–	–	–	–	–	–
4	*390*	974	1299	1374	1228	837	141	–	–
	7030	17554	23214	**24047**	20349	11447	–	–	–
6	*191*	*603*	974	1221	1349	1374	1302	1127	–
	3416	10884	17554	21905	23992	**24047**	22109	18017	–
8	*108*	*390*	*705*	974	1171	1299	1365	1374	–
	1922	7030	12734	17554	21040	23214	**24191**	24047	–
16	*21*	*108*	*237*	*390*	*550*	705	848	974	1376
	343	1922	4260	7030	9930	12734	15300	17554	**24257**

Table 3.2. $R = 20000$, $\zeta = 0.1$, $\sigma = 1$. *As in Table 3.1, for each aspect ratio the first row gives the value of the Chandrasekhar number $Q_m^{(e)}$ at which the bifurcation to m pairs of steady rolls occurs for $m = 1 \ldots 8$, (plus $m = 15$ the wavenumber at onset for $\lambda = 16$). The second row gives the corresponding positions of the Hopf bifurcations $Q_m^{(o)}$. Again $Q_{max}^{(o)}$ is given in bold, and any bifurcations that are subcritical close to the bifurcation point are italicised. No entry implies that the mode does not exist for any positive Q.*

§3.2.1. Modified perturbation theory

Perturbation theory for the case of convection in a vertical magnetic field was first studied in Knobloch *et al.* (1981), and allows us to determine whether the bifurcation to finite-amplitude convection is subcritical or supercritical. (also Veronis (1959))

First consider the simple bifurcation at $Q = Q_m^{(e)}$. Given a small-amplitude (steady) solution in the neighbourhood of $Q_m^{(e)}$ we may investigate the bifurcating branch by expanding the Chandrasekhar number in terms of the amplitude a as

$$Q = Q_m^{(e)} + q_m^{(e)} a^2 + O(a^4)$$

for $a^2 \ll 1$. Solving for a nonlinear steady solution of (3.14) and expanding in

powers of a^2 gives

$$q_m^{(e)} = \frac{\pi^2(4m^2-\lambda^2)}{4\lambda^2\zeta^2} - \frac{m^2}{(4m^2+\lambda^2)^3\pi^2\zeta^2}\left(2m^2\zeta^2(4m^2+\lambda^2)+\lambda^2(4m^2-\lambda^2)\right)R \tag{3.23}$$

From this we can deduce that this steady bifurcation is supercritical (close to the bifurcation point) if $q_m^{(e)} < 0$ and subcritical otherwise.

In Table 3.1 these results are applied to the situation that will be discussed in §3.7. For five different values of the Rayleigh number, the position of both the steady and Hopf bifurcations are given for modes with wavenumbers $m = 1 \ldots 8$. Similarly, the positions of the bifurcations to the main steady and oscillatory are given in Table 3.2 for several values of the aspect ratio to be discussed in §3.5.

§3.3. *The model system*

In order to ascertain whether similar bifurcations may be obtained to those seen in Chapter 2 I conducted numerous numerical experiments for different values of key parameters. A rough parameter sweep was performed through variation of the field strength and superadiabatic temperature gradient, achieved by varying Q and R respectively, and also through testing how the convective pattern is altered by increasing and decreasing the aspect ratio of the box λ.

For $\zeta \geq 1$ the convective instability always sets in as stationary convection. For a given value of R, (3.18) allows us to calculate the preferred wavenumber at which convection first occurs in a box of width λ, and the value of $Q_{max}^{(e)}$ at which this happens.

As a measure of the strength of the convection the Nusselt number N_u was calculated in each case, where

$$N_u = -\left\langle \frac{\partial T}{\partial z} \right\rangle \Bigg|_{z=0} = 1 - \pi\langle\theta_1\rangle - 2\pi\langle\theta_2\rangle \tag{3.24}$$

The angled brackets represent taking a horizontal average. In the case of oscillatory or time-dependent behaviour, a suitable time average was also taken to calculate a characteristic Nusselt number. In order to determine the number of cells in each solution, the number of the largest Fourier mode was found. This is by no means assured of describing the pattern of convection accurately, but was found to give the correct answer in almost all cases.

r	Veronis	Rucklidge	results	$3-\frac{2}{r}$
1.0	1.00	1.0000	1.000	1.000
1.1	1.18	1.1848	1.182	1.182
1.2	1.34	1.3440	1.333	1.333
1.4	1.61	1.6067	1.571	1.571
2.0	2.14	2.1424	2.000	2.000
3.0	2.68	2.6784	2.333	2.333
4.0	3.04	3.0402	2.500	2.500
6.0	3.55	3.5535	2.667	2.667
8.0	3.93	3.9337	2.751	2.750
10.0	4.24	4.2435	2.801	2.800
20.0	5.33	5.3333	2.903	2.900
40.0	6.68	6.7404	(2.716)	2.950

Table 3.3. *Comparing the results of our model with Veronis (1966) and Rucklidge (1991). The Nusselt number N_u is given as a function of $r = R/R_0$, where R_0 is the value of the Rayleigh number at which the convective instabililty first sets in. In this case $Q = 0$, $\sigma = 6.8$, $\zeta = 0.5$ and $\lambda = 2\sqrt{2}$. Veronis used 10x10 modes and Rucklidge 24x24. The bracketed entry indicates that the solution was oscillatory, and the long time average is given.*

§3.3.1. Testing the model

As a test some preliminary results were performed in the absence of a magnetic field, and compared to established results (Rucklidge 1991, Veronis 1966) which set the Prandtl number $\sigma = 6.8$ and the ratio of the magnetic and thermal diffusivities $\zeta = 0.5$. These are shown in Table 3.3. As expected the results give comparatively poor accuracy due to the limitations of the low order truncation. I also found that the flow saturates for high values of Rayleigh number, hence the discrepancy between the values for $r = 40$ in the table. However, given that I am primarily interested in studying the types of convection that may be produced by our low-order model simply in an attempt to reproduce those seen in §2.2 and §2.3, these quantitative limitations are unimportant and to be expected.

Using for the moment the full truncation given in (3.13), a static solution to (3.14) is easily found. In the absence of a magnetic field, the Nusselt number can be explicitly calculated from this to be $3 - 2/r$, where $r = R/R_0$ and $R_0 \approx 657.5$, the value of the Rayleigh number at which convection first sets in.

Comparison of the Nusselt number found in our numerical experiments and this theoretical value is given in Table 3.3, and they agree to high accuracy. This shows that although up to 32 modes are being retained in the horizontal direction, almost all of the contribution to the heat flux comes from the lowest mode, a result that is not unexpected. The agreement fails for $r > 30$, as the solutions are oscillatory in these cases.

§3.4. *Varying the field strength*

I began by observing the range of possible behaviour obtained when varying the magnetic field strength for fixed aspect ratio $\lambda = 6$, and superadiabatic temperature gradient $R = 20000$. These values were chosen as they were found to give representative behaviour, and the box is sufficiently wide that the flow is able to select its preferred lengthscale, whilst not being restricted by the constraints of the computational box.

The ratio of the magnetic to the thermal diffusivity ζ plays a crucial role in the determination of the range of behaviour observed in numerical simulations of convection. For $\zeta < 1$ we obtain oscillatory convection at onset, and behaviour in the nonlinear regime is similarly affected. For example, in §2.2–§2.4 the simulations all held $\zeta_0 = 0.2$, $\sigma = 1.0$, giving rise to the full range of convective behaviour: small-scale steady and oscillatory convection giving way to flux separation and the rapid change of scale seen as Q was reduced. Accordingly I chose to hold the diffusivities fixed at $\zeta = 0.1$, and $\sigma = 1$, until I finally study the effects of altering ζ in §3.11.

The experiments were performed by starting from the initial static state given by (3.10) representing a stationary fluid in a uniform, vertical magnetic field, and introducing small random temperature fluctuations as before. This was done for $Q = 0$ and continued until a steady solution was obtained (or terminated after a time if the flow were found to be time dependent). Q was then increased by a small amount ΔQ (usually $\Delta Q = 10$) and another solution found. This was continued until the magnetic field was strong enough to suppress all convection. To reduce calculation time and for ease of comparison, the run for each value of Q was begun from the final state of the previous value of Q. This method also has

the advantage of following a particular solution branch until it becomes unstable, thereby determining the extent of a particular pattern. This approach of holding R fixed and increasing Q is equivalent to the more usual method of holding Q fixed and *decreasing* R, however given that the study is investigating the effects of regions of concentrated magnetic flux and how they develop this method was deemed more appropriate.

The results are shown in Figure 3-1–Figure 3-5. In Figure 3-1 a measure of the convective flux at the surface dT/dz is plotted (horizontally) for the final state of each value of Q. In each case the flow settled down to a steady state, and no permanent time dependent behaviour was observed, though near values of Q for which a change of pattern occurred it took considerably longer to reach steady state. As before, brighter areas indicate high values of heat flux, and dark areas are regions in which heat flow is suppressed. Accordingly, it is easy to see the different types of behaviour that are obtained as Q is varied. For very low field strengths the solution is dominated by the fluid flow, and eight steady circular rolls are seen forming four identical, symmetric plumes in which hot fluid rises in the middle moves horizontally outwards and falls again at the outside as it cools (Figure 3-2(a)). These are qualitatively similar to those seen in Figure 2-13, for example, although the scale of convection is clearly different and there is no time dependence. The magnetic field occupies the small spaces at the centre and the edges of each plume, held there by the flow to either side of it and is only slightly distorted from the vertical. As in Figure 2-13 there is an area of high field strength near the surface at the edge of each plume, where two neighbouring outflows meet. Similarly we can see a region of high magnetic flux near the base at the centre of each plume, at the confluence of two inflows. The fact that we have only one vertical magnetic mode in addition to the mean field prevents further similarity. The flow is also restricted by the symmetry of the equations (3.1), in that the solution bears the standard Boussinesq symmetry; the symmetries of the governing Boussinesq equations immediately imply the existence of the alternative solutions obtained via

$$(x, z) \to (x, 1 - z), \quad (\psi, \theta, A) \to (-\psi, -\theta, A)$$

or

$$(x, z) \to (\Gamma - x, 1 - z), \quad (\psi, \theta, A) \to (\psi, -\theta, -A) \tag{3.25}$$

where Γ is the width of a roll – in essence turning the page upside-down and reversing the arrows and colour scheme.

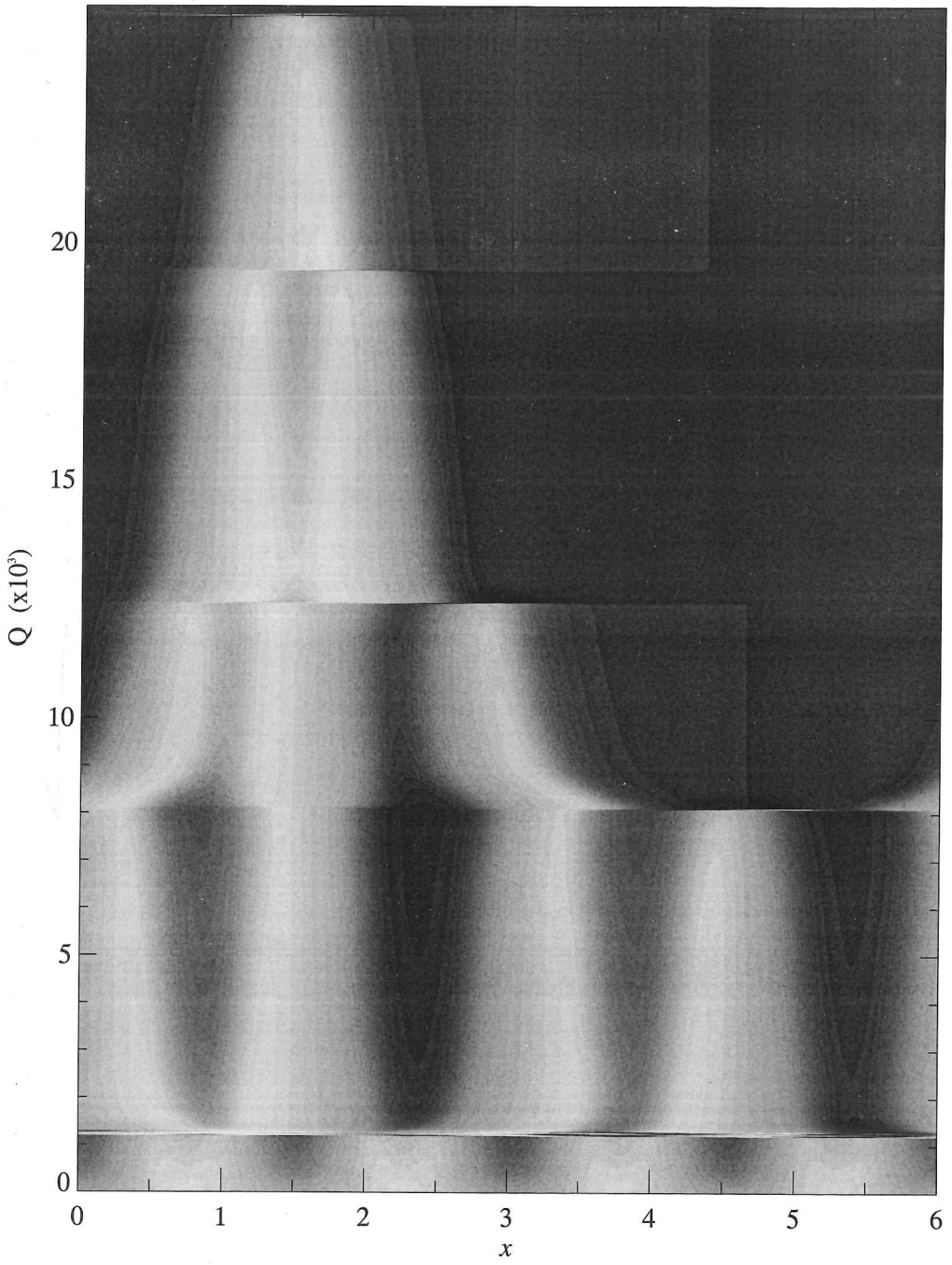

Figure 3-1. *Surface dT/dz for the final solution state of each value of Q, with $\lambda = 6$, $R = 20000$ ($\zeta = 0.1$, $\sigma = 1$). This method of plotting the data allows the convective pattern found in each case to be determined at a glance, and the values of Q at which key bifurcations occur. For example, for $Q < 1300$ a solution consisting of 4 steady plumes is obtained, whereas for $1300 < Q < 8000$ there are 2 steady plumes each with a central region of high field strength which increases in size as Q is increased. For higher Q the number of rolls is reduced to 3 then 2 and finally for $Q > 19400$ only a single isolated roll is seen which then shrinks slowly in size before dying out abruptly at $Q \approx 24800$.*

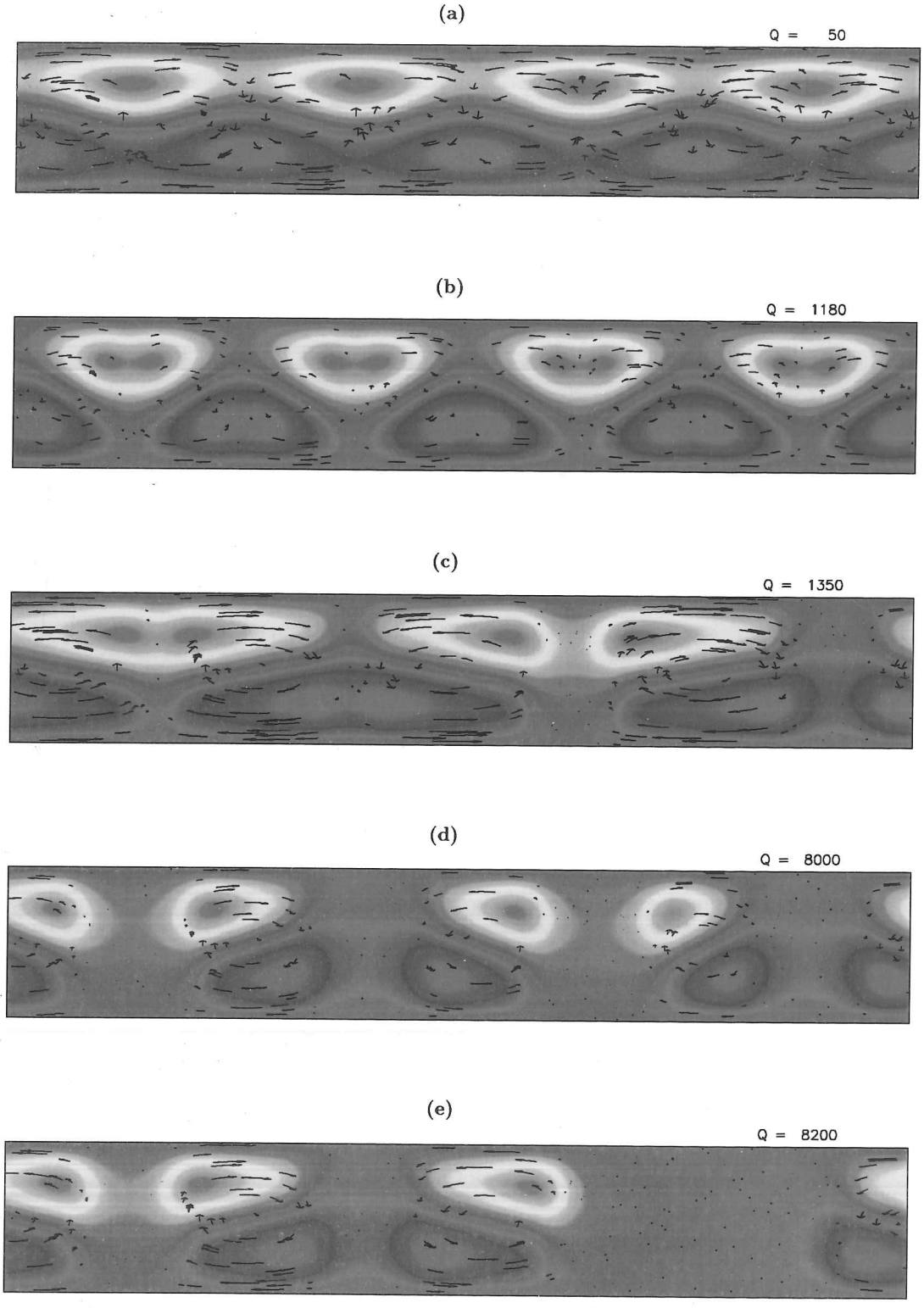

Figure 3-2. *Solutions found by increasing the field strength in small steps of for* $\lambda = 6$, $R = 20000$ ($\zeta = 0.1$, $\sigma = 1$). *Again temperature deviations* θ *from the static solution (3.10) are shaded with red hot and violet cold, as ever, and super-imposed velocity arrows.*

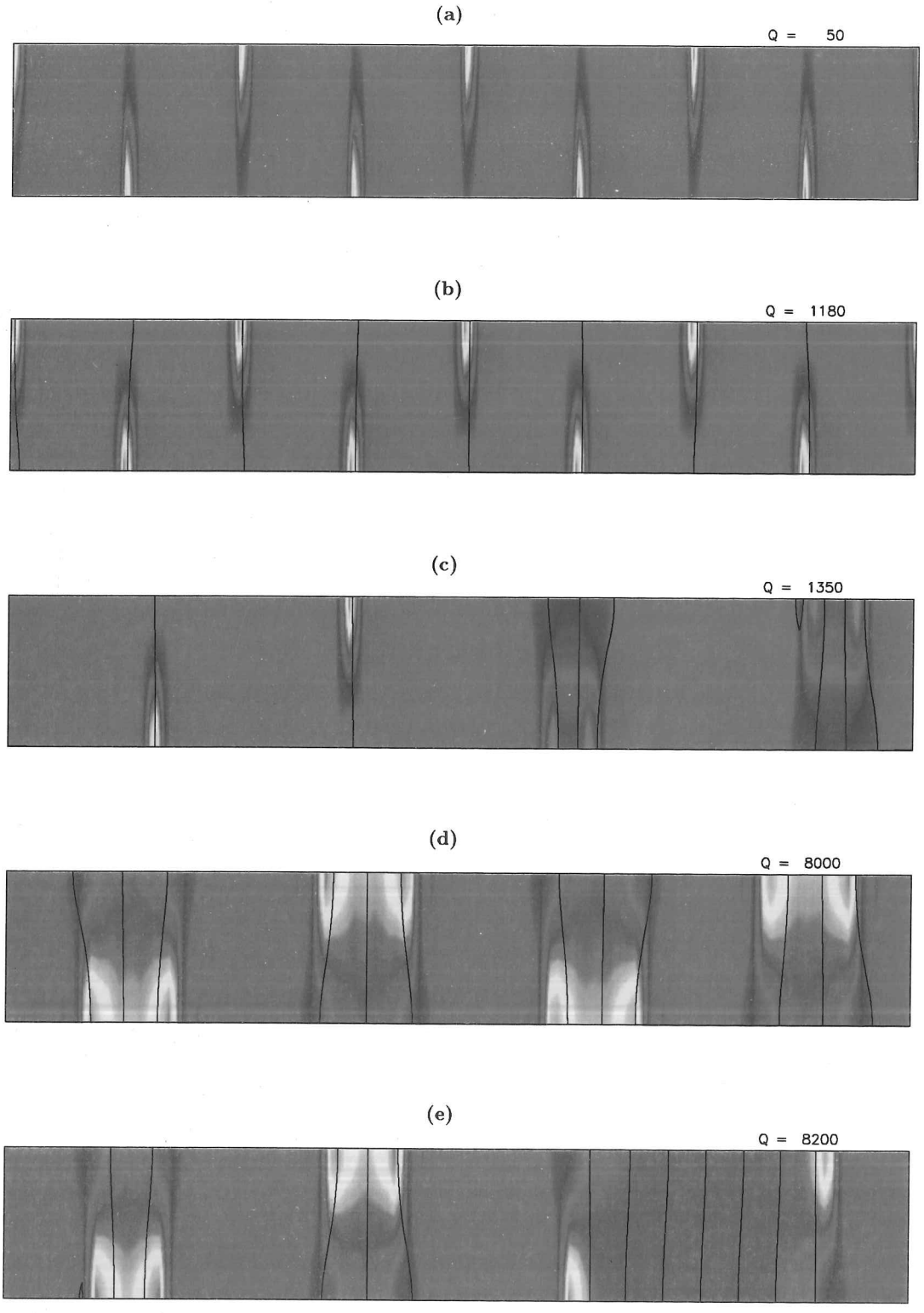

Figure 3-3. *As in Figure 3-2 except that the shading is the magnetic field strength B^2 and magnetic field lines are shown.*

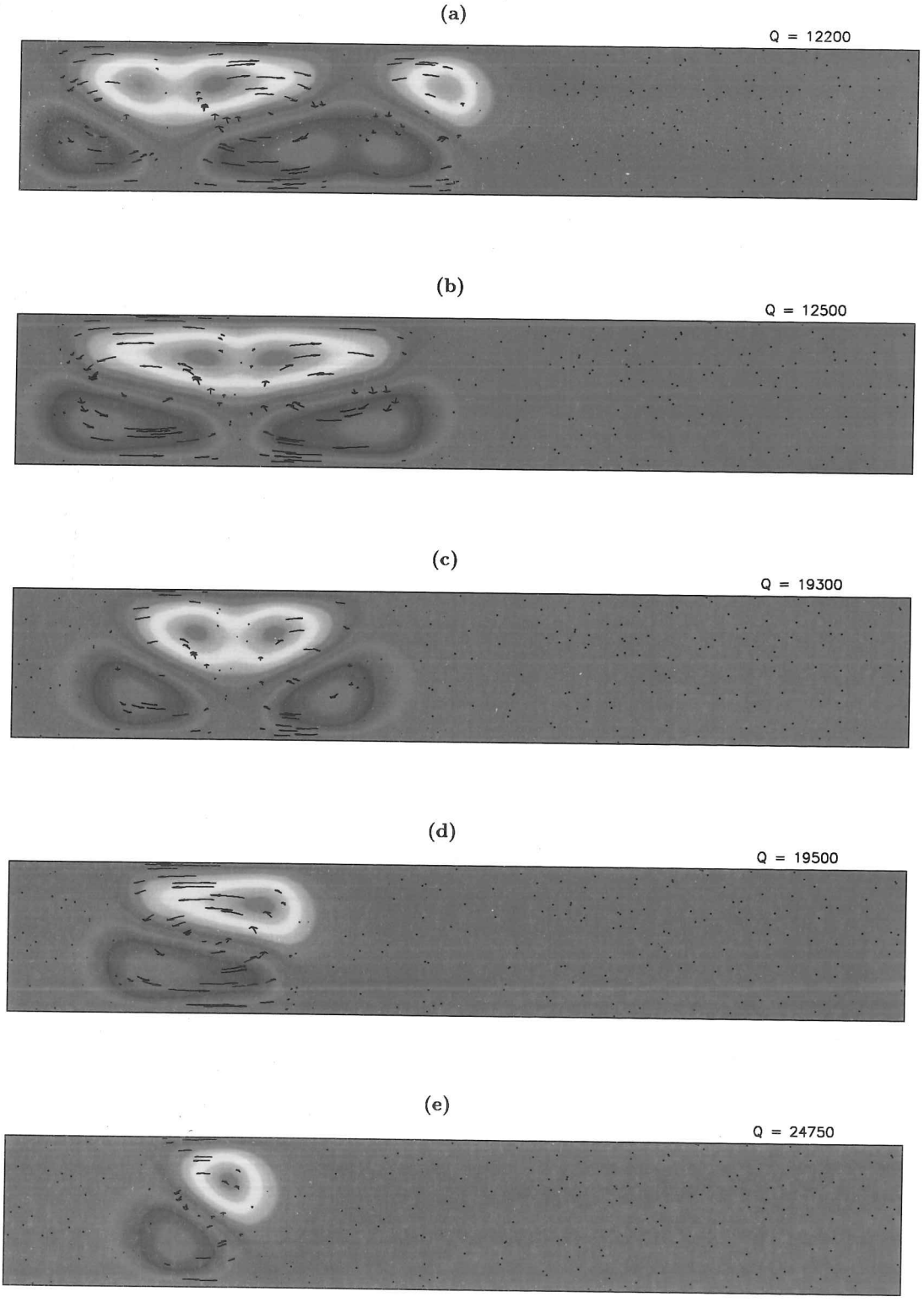

Figure 3-4. *A continuation of Figure 3-2.*

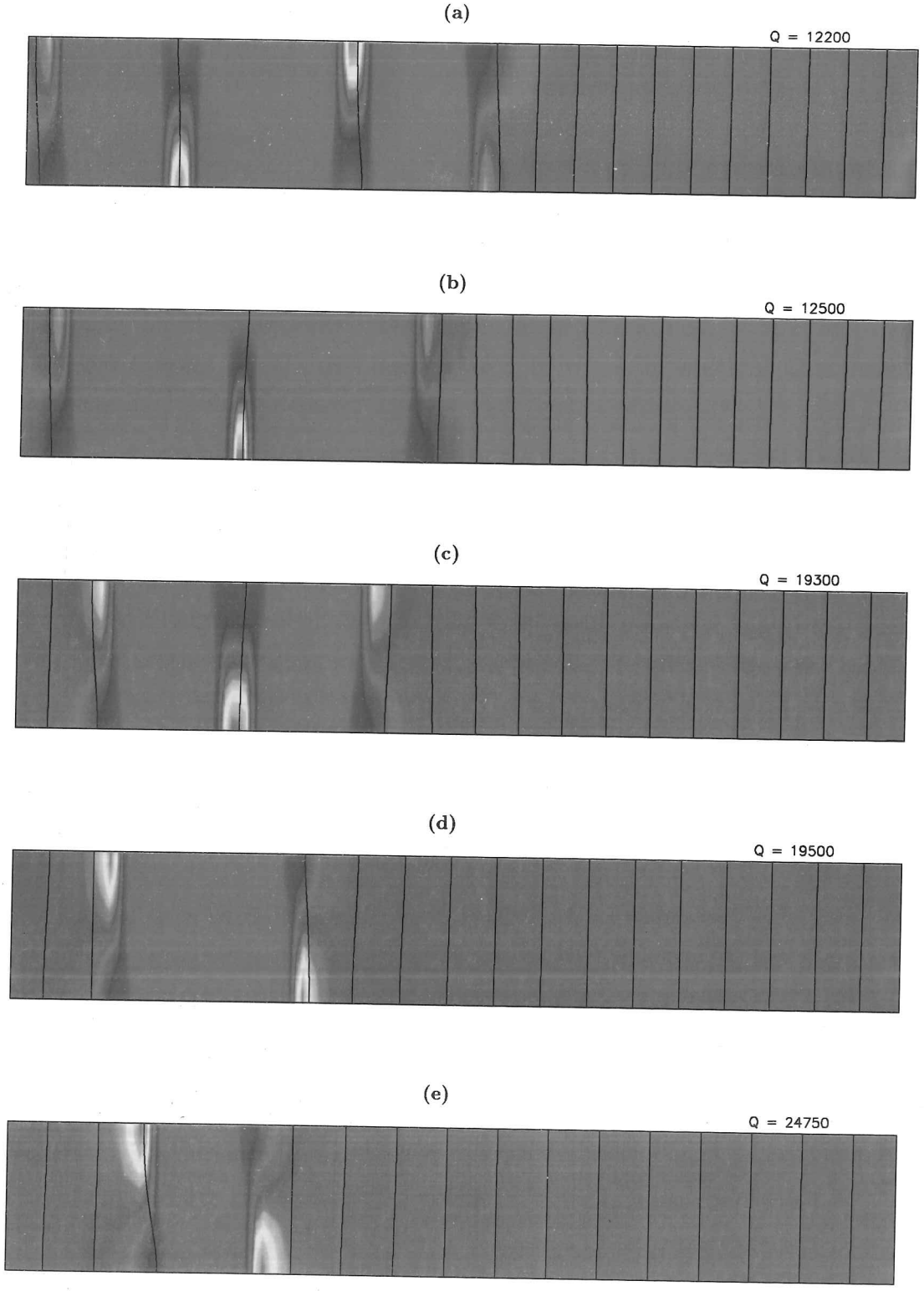

Figure 3-5. *A continuation of Figure 3-3.*

At $Q \approx 1300$ there is a sudden change in the pattern of convection. As is clear from Figure 3-2(c) there are now only four rolls instead of six. There are now two narrow regions in which convection has been completely suppressed, corresponding to regions of high field strength into which almost all of the magnetic field has been swept.

As the field strength is further increased, the two magnetic regions grow in size, and two further regions of high field strength grow to a similar size (Figure 3-3(d)), until at $Q \approx 8100$ one of the rolls is rapidly suppressed. Here a crucial mirror symmetry within each plume has been broken and there are now three rolls, an odd number for the first time. The region of magnetic field is now much more pronounced (Figure 3-3(e)), and once again it increases in width as Q is increased further.

The system next bifurcates at $Q \approx 12400$ when the magnetic field is sufficiently strong to suppress another of the rolls. From 3 rolls of width ≈ 0.9 the system bifurcates to 2 rolls with width ≈ 1.2. This increase in roll size reflects a more fundamental consideration; the width of the convective region is a result of a balance between the pressure gradients of the fluid flow pushing outwards and the Lorentz forces of the magnetic wall at its edge. The two rolls are able to keep the magnetic field at bay by convecting a little more vigorously than the three rolls were able to, with only a small reduction in the size of the convective region. Increasing Q once again increases the size of the Lorentz forces, and the width of the two rolls decreases accordingly until at around $Q = 19000$ the width is ≈ 0.9 once more (Figure 3-4(c)).

Then, at $Q \approx 19400$ the final stage of this new sequence of bifurcations takes place and the last remaining mirror symmetry is broken leaving the state shown in Figure 3-4(d). The majority of the box remains in the basic state of strong, almost vertical magnetic field in which all convection is suppressed; however, a small region remains in which the flow is again able to expel virtually all the magnetic flux, creating an isolated island consisting of a single narrow convective roll. Final increases in field strength cause convection to be completely suppressed, leaving the basic conducting state after $Q \approx 24800$. This single isolated roll seen above raises many important questions; I have called such rolls *convectons*, and they will be discussed at greater length in §3.6.

§3.5. *Varying the aspect ratio*

I next conducted a brief investigation of how the above results changed as the width of the box was altered. The results of §2.2 showed that the convective patterns were simpler the smaller the box width, due to the restrictions on the possible wavenumbers, and none of the flux separation discussed in §2.2.3 for lower aspect ratios. These results also demonstrated the importance of ensuring that the experimental domain is sufficiently wide to allow the preferred convective behaviour for the case of fully compressible magnetoconvection, and there is every reason to expect that the same is true in the low order system studied here.

§3.5.1. $\lambda = 1$

In the case of $\lambda = 1$, the box is sufficiently small that the wave number $m = 1$ dominates for all values of Q. Nevertheless, we still see a variety of different results. Again for low field strength we are in a kinematic regime and obtain steady symmetric convection. However, as we increase Q the flow quickly becomes time dependent. For $Q = 1200$ the pattern is that of periodic oscillations, shown in Figure 3-8(b), displayed at an interval of about half a period, in which plumes alternately wax and wane. At $Q \approx 4200$ we see the formation of a more permanent flux sheet strong enough to resist being torn apart by the flow. This results in a drop in convective efficiency, seen in Figure 3-6(a) as a sudden reduction in the Nusselt number. Increasing Q further causes the magnetic field to dominate convection within the box, and from $Q \approx 8500$ the field strength is more or less uniform across the whole domain. Prior to this there existed regions in which the fluid flow was able to expel the magnetic flux completely, whereas in Figure 3-8(d), say, deviations from the uniform field strength are small ($\approx 20\%$). Eventually for higher and higher values of Q, the flow becomes increasingly feeble until it eventually ceases at $Q \approx 24000$.

§3.5.2. $\lambda = 2$

Doubling the aspect ratio to 2 allows the flow considerably more freedom and we naturally see a greater variety of behaviour. An overview of the types of convection seen is given in Figure 3-7(a), and snapshots of representative behaviour are displayed in Figure 3-9. For moderate values of Q we observe two steady symmetric cells (Figure 3-9(a)), analogous to those seen in the case of $\lambda = 6$ (Figure 3-2(a)), in which the meagre magnetic field is clustered into the two small regions where horizontal flows meet. At $Q \approx 3800$ the system bifurcates and the pattern becomes unsteady. This aperiodic region is merely transitional, though results in

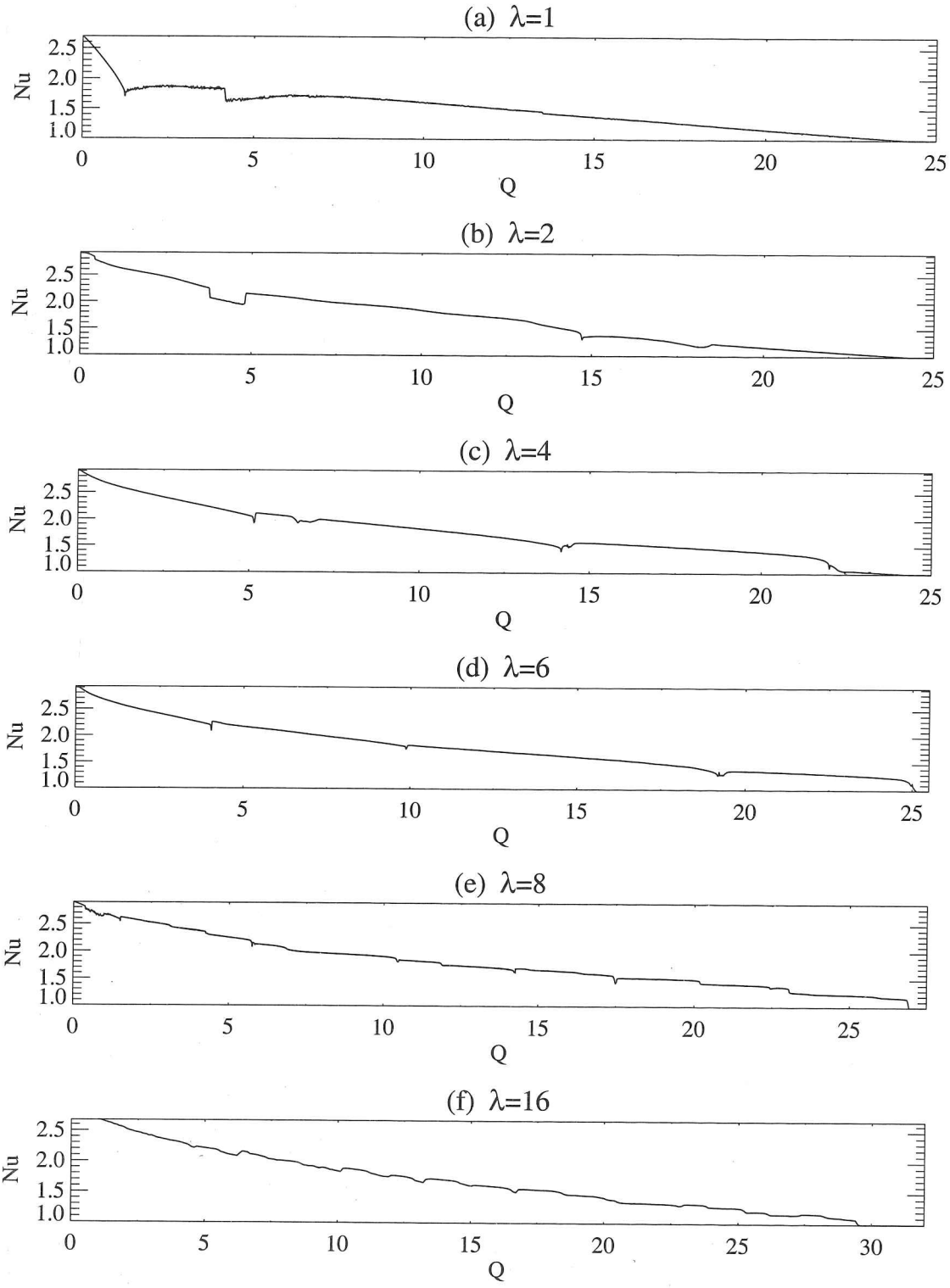

Figure 3-6. *The Nusselt number plotted as a function of Q as the field strength is increased in small steps for different values of the aspect ratio.*

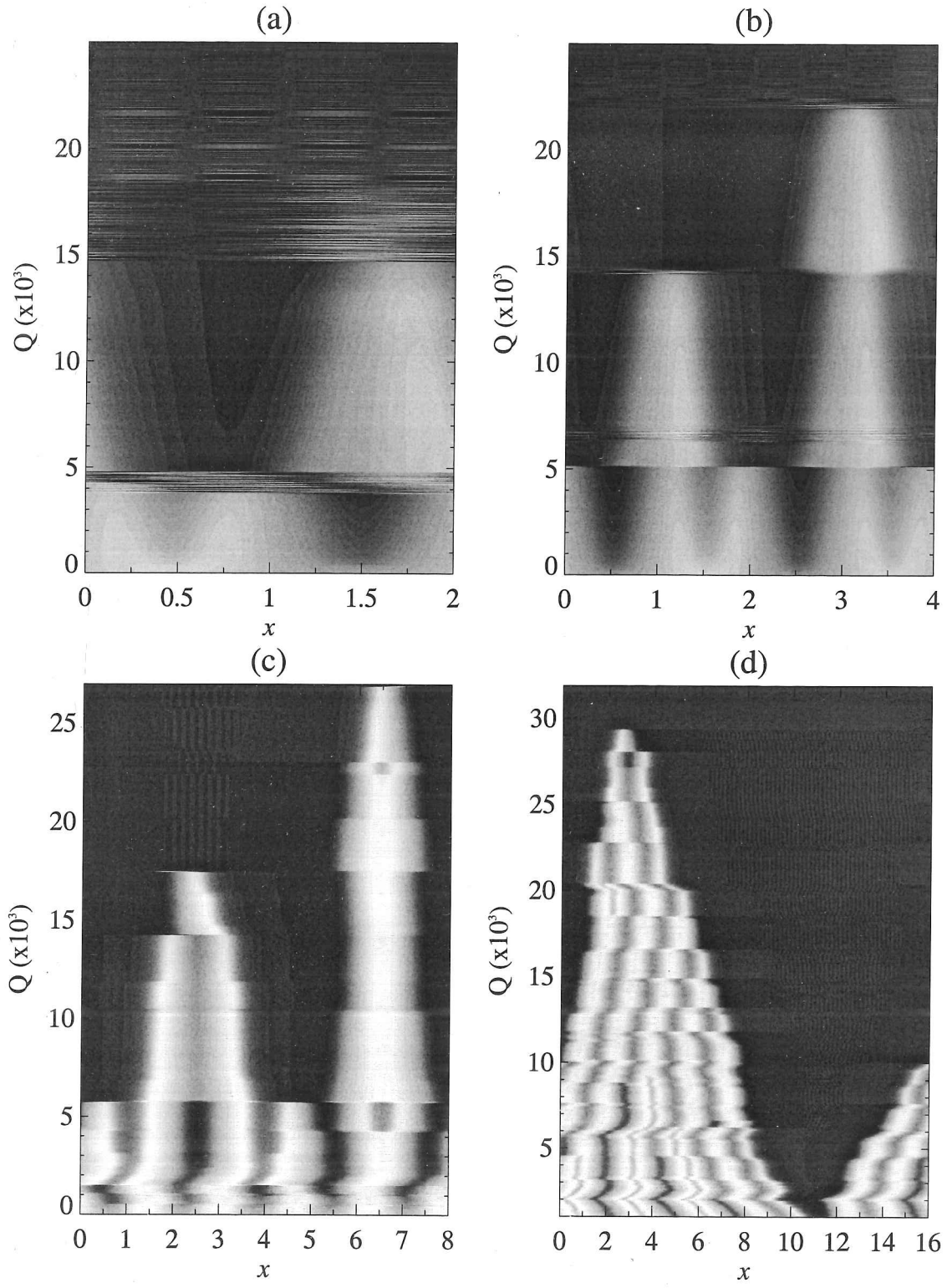

Figure 3-7. *Surface dT/dz for the final solution state of each value of Q as Q is increased in small steps, for $R = 20000$ and (a) $\lambda = 2$, (b) $\lambda = 4$, (c) $\lambda = 8$, (d) $\lambda = 16$. For each Q the final solution is used as the initial state for the next value of Q.*

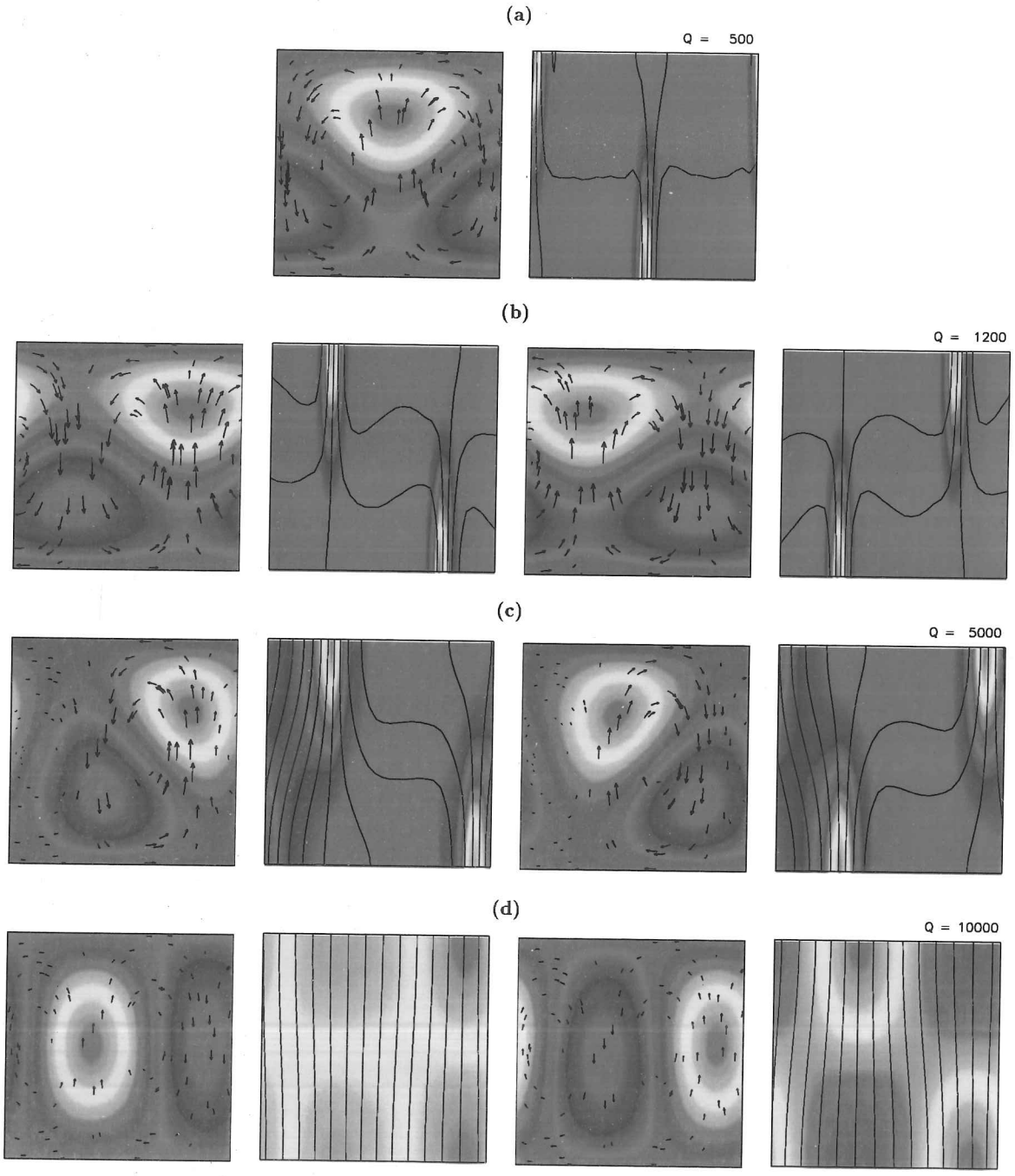

Figure 3-8. *Observed patterns of convection for the case* $\lambda = 1$, $R = 20000$ *as the field strength is varied. In (a) the solution is steady, but in (b),(c),(d) oscillatory convection is obtained. For each pair of images, the lefthand one shows temperature deviations* θ *with velocity arrows, and the righthand one shows the magnetic field strength* B^2 *with field lines. For the time dependent cases (b),(c),(d) two pairs of images are given to show the oscillations at opposite phase.*

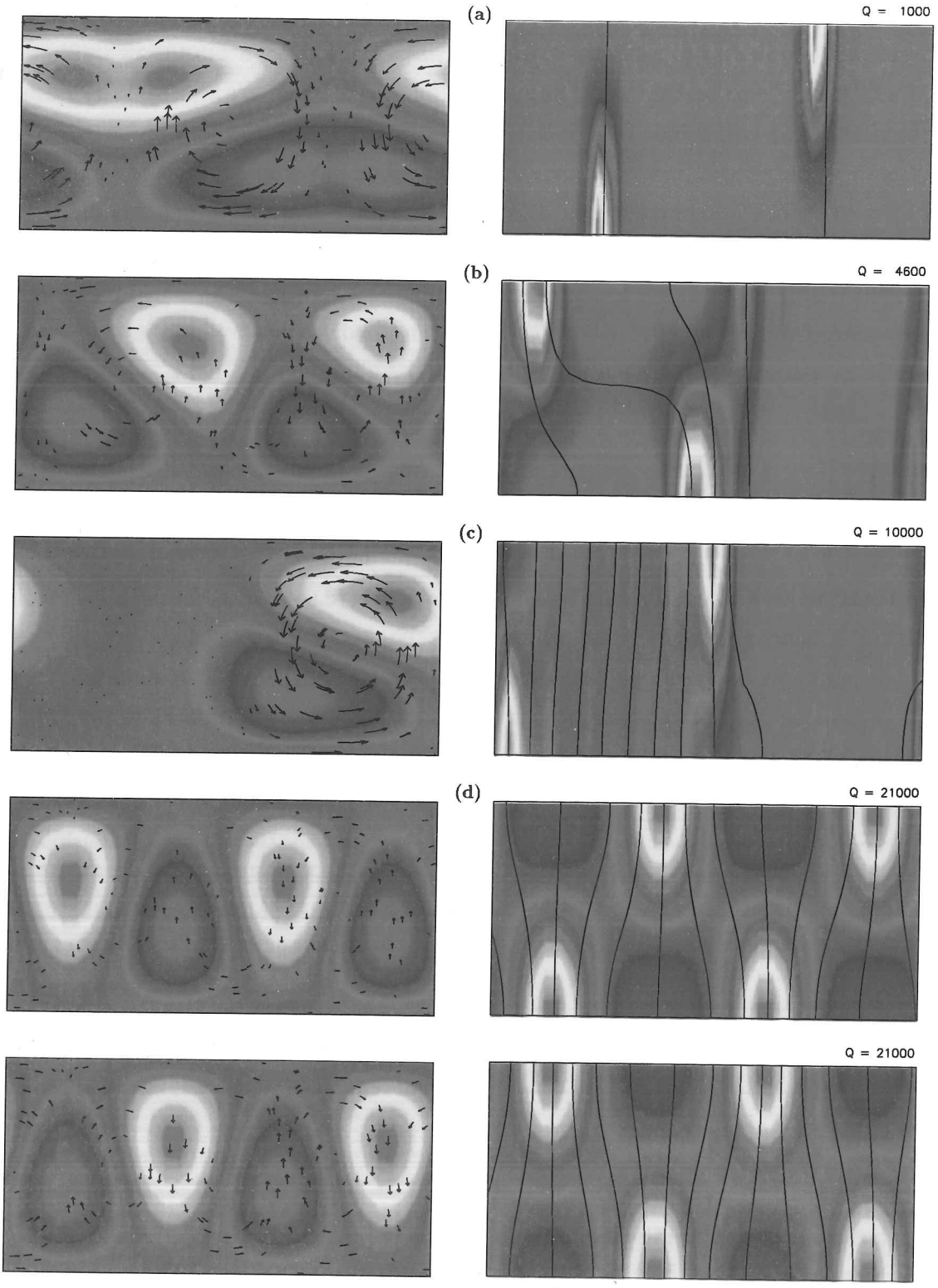

Figure 3-9. *Observed patterns of convection for the case $\lambda = 2$, $R = 20000$ as the field strength is varied. (a) & (c) are steady, and (b) shows a snapshot as the flow is irregular. (d) gives pairs of snapshots with the oscillations at opposite phase. The figures are as described in Figure 3-8.*

a temporary reduction in the transport of heat flux (see Figure 3-6(b)), and at $Q \approx 4800$ we obtain a secondary steady solution comprising of a single roll or convecton (Figure 3-9(c)). The roll occupies around one third to one half of the box, with the remainder of the box free from convection and containing practically all of the magnetic field. Again as the field strength is increased the region of magnetic flux expands, compressing the increasingly feeble convective roll, until at $Q \approx 14600$ we move onto a stable unsteady branch and we see periodic oscillations in which two pairs of identical plumes wax and wane alternately. Two shots of this, taken half a period apart, may be seen in Figure 3-9(d). Finally, all convection is suppressed at $Q \approx 24400$, with the flow dying very gradually rather than abruptly as seen for some other values of the aspect ratio.

§3.5.3. $\lambda = 4$

The case of $\lambda = 4$ is qualitatively very similar to that of $\lambda = 6$ described above (§3.4)(see Figure 3-7(b)). For low values of the magnetic field strength two steady double plumes are obtained, and remain until dropping onto a different steady branch at $Q \approx 5100$. Here we observe two separate convectons, though having retained some of the symmetries of the previous solutions, separated by a wavelength of $\bar{\lambda} = 2$. This symmetry is once again broken at $Q \approx 14200$ and the familiar single roll solution is obtained. Unlike $\lambda = 6$, however, we move onto an oscillatory branch at around $Q = 22000$ and four pairs of oscillatory plumes fade gradually until dying away completely at the linear stability boundary of $Q \approx 24000$.

§3.5.4. $\lambda = 8$

The case of $\lambda = 8$ is qualitatively similar to that of $\lambda = 6$ discussed in §3.4. The sequence of patterns obtained as Q was increased may be seen in Figure 3-7(c). Convection finally dies out at $Q = 26950$.

§3.5.5. $\lambda = 16$

In order to verify that the experimental box in the case $\lambda = 6$ is indeed wide enough to accommodate the full range of convective patterns, I repeat the calculations in an extremely wide box $\lambda = 16$. As expected, the extra width of the box is conducive to more complicated flow and indeed, as may be seen in Figure 3-7(c), the number and types of bifurcations are more complex than in the cases studied for narrower boxes. However, closer inspection reveals that the sequence of changes and the types of convective behaviour observed are the same as was seen for $\lambda = 6$ (see

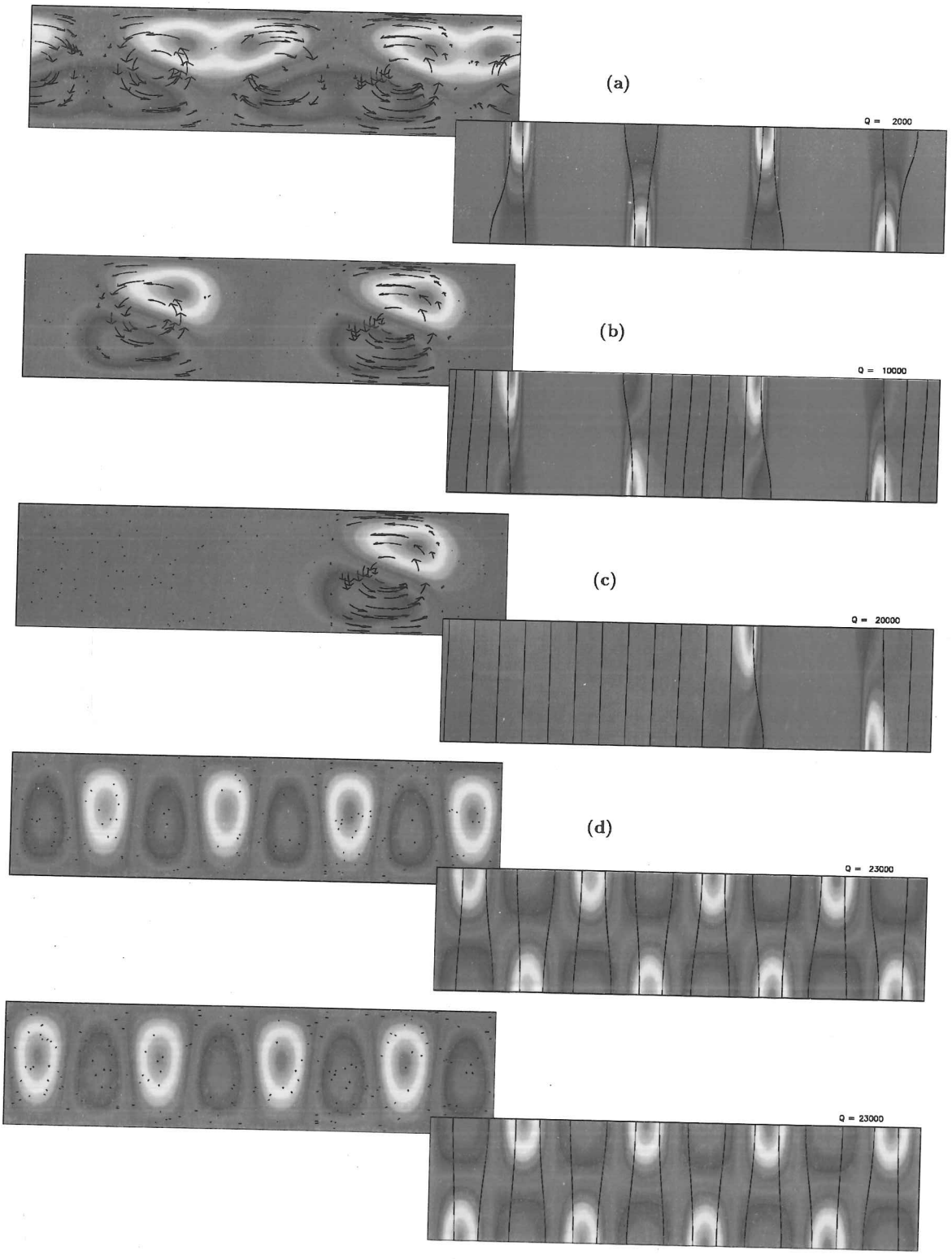

Figure 3-10. *Observed patterns of convection for the case $\lambda = 4$, $R = 20000$ as the field strength is varied. Only (d) is time-dependent and two pairs of snapshots are given. The figures are as described in Figure 3-8.*

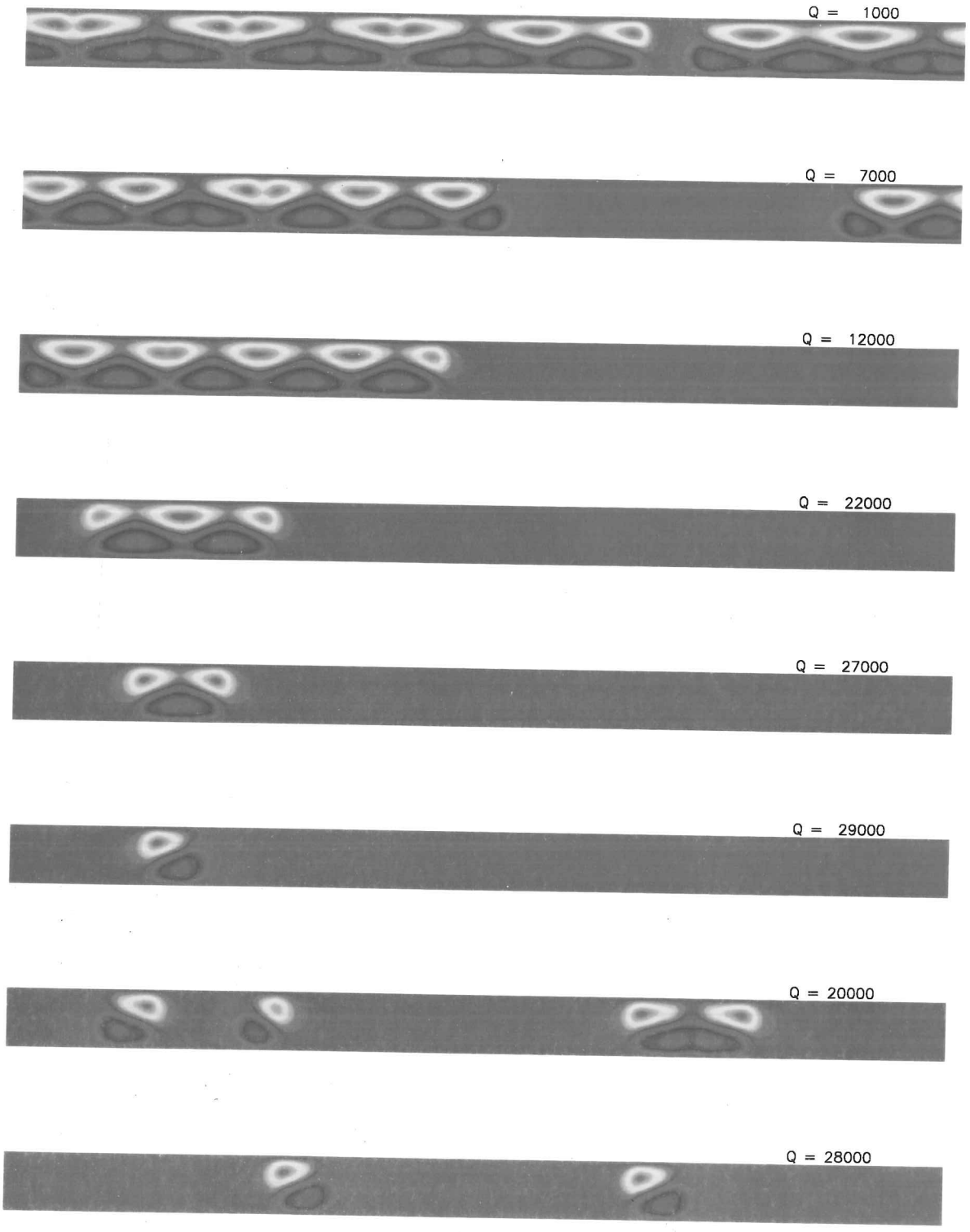

Figure 3-11. *Observed patterns of convection for the case* $\lambda = 16$, $R = 20000$ *as the field strength is increased in small steps. Here all figures show temperature deviations* θ.

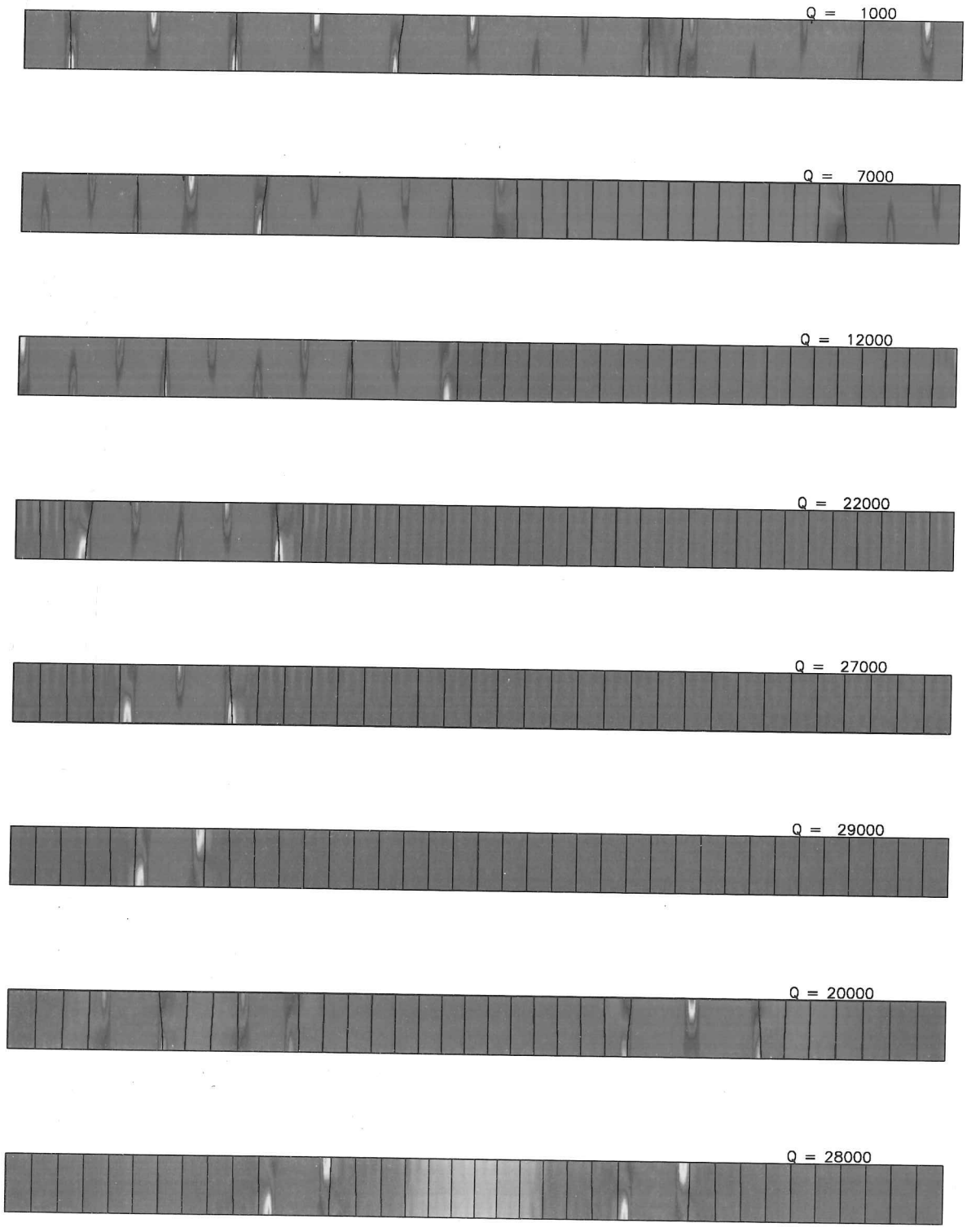

Figure 3-12. $\lambda = 16$, $R = 20000$. *As for Figure 3-11 except the shading is magnetic field strength, and field lines are shown.*

Figure 3-11). Increasing Q from zero once again, we initially see 18 rolls in the form of nine steady, regularly-spaced plumes. The symmetry is soon lost as the magnetic field is allowed to form small regions between some of the plumes and from here onwards the magnetic field begins a gradual quest to reduce the number of rolls one by one. The increased freedom of the wide box allows the mirror symmetry of an individual plume to be broken much more readily and by $Q = 1000$ the number of rolls has already been restricted to 13. By $Q = 7000$ there are 12 rolls and at $Q = 11000$ still 10, though they are significantly smaller than those at low Q, cramped into about half of the box with strong magnetic field occupying the remainder. As Q is increased further the number of rolls reduces sequentially until finally at $Q = 28200$ only one fully isolated convecton remains before even this is suppressed at $Q = 29500$.

Further investigation of flow in boxes with $\lambda = 16$ reveals a bewildering variety of possible patterns. Steady solutions are found containing any number of rolls, and beyond $Q = 15000$ the rolls are no longer usually found in bound pairs but exist essentially independently of one another with several scattered across the box (Figure 3-11(g),(h)).

Although linear theory (§3.2) predicts that, for the case $\lambda = 16$, the trivial solution is stable for $Q > Q^{(o)}_{max} = 24267$, stable convective solutions are observed in the range $20300 < Q < 29500$. As may be seen in Figure 3-11 the individual rolls show less variance in size than for the case $\lambda = 6$ as the change in Lorentz force acting on each roll as the increase in Q is effected is smaller. For the convecton, the maximum width is $\bar{\lambda} \approx 1.6$ (at $Q = 20300$) and the minimum is $\bar{\lambda} \approx 1.0$ (at $Q = 29500$).

A single convecton was also found in a box of aspect ratio $\lambda = 32$ with a width of $\bar{\lambda} \approx 1$, and in the next section I will argue that any number of convectons with $\bar{\lambda} = O(1)$ may be located in arbitrarily wide boxes.

§3.6. *Convectons*

In their papers Galloway & Weiss (1981) and Weiss (1981) considered two-dimensional Boussinesq magnetoconvection in comparatively narrow boxes with imposed mirror (Z_2) symmetry. Their results appear to show single isolated rolls separated by regions of magnetic flux, but the imposed symmetries mean that they are in fact pairs of rolls. Figure 3 of Galloway & Weiss does however show an important departure from previously observed behaviour in that the two rolls are both

convecting in an anti-clockwise sense, demonstrating the ability of the intermediate magnetic field to absorb the pressure gradients.

These results suggest that if the width of the box were increased and the imposed symmetry removed then an important development might occur, resulting in a single, fully isolated roll, unconstrained by the dimensions of the computational domain. In boxes with fairly small aspect ratio single convectons are seen for $Q < Q_{max}^{(o)}$ as in forcing all the magnetic field into one region the flow increases the effective field strength there so that $Q_{eff} > Q_{max}^{(o)}$. In arbitrarily large boxes convectons should still be possible, but will only be seen for $Q > Q_{max}^{(o)}$, and indeed for $\lambda = 16$ ($Q_{max}^{(o)} = 24267$) single convectons are only stable in the range $26000 < Q < 30000$. This is because for $\lambda \gg 1$ a single convecton will only increase the effective field strength in the magnetic region by a very small amount, and so for $Q < Q_{max}^{(o)}$ this region will be unstable to perturbations and oscillations will be seen. It is this bistability in very wide boxes, or coexistence of stable trivial and nonlinear solutions for $Q > Q_{max}^{(o)}$, that is associated with isolated states.

In Figure 3-13 we may see the isolated nature of the convecton by examining the magnetic field, temperature and velocity of such a solution. In particular the horizontal velocity is essentially only non-zero in a very localized region. Similarly, the horizontal magnetic field strength B_x shows clear peaks at either end of the roll. Either of these quantities may be used to define the width $\bar{\lambda}$ of the convecton, and both give practically identical values. The magnetic field is predominantly vertical, and the shape of the vertical field B_z is reproduced in the overall field strength B^2. Both show peaks at the right hand side of the convecton, showing a small region of higher field strength on that side near the surface. This is clearly due to the fact that the velocity near the surface carries any residual field from within the convecton to the right hand edge, where it remains slowly diffusing outwards. The same may be seen at the lower left of the convecton in the second frame of Figure 3-13.

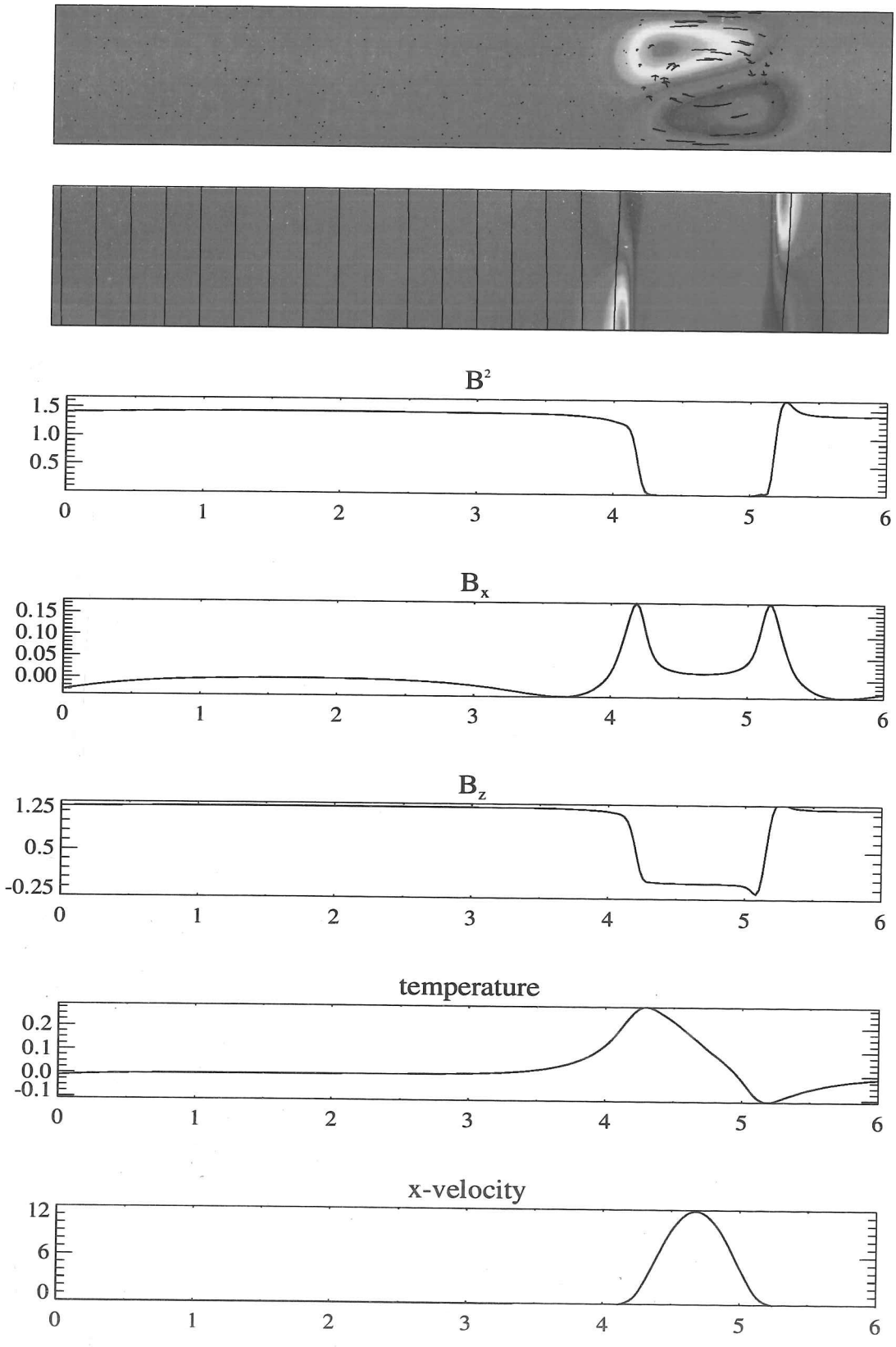

Figure 3-13. *A typical convecton solution, $\lambda = 6$, $R = 20000$, $Q = 22000$, together with various physical quantities, plotted near the surface.*

R	Q_{min}	Q_{max}	$Q_{max}^{(o)}$	$\bar{\lambda}_{min}$	$\bar{\lambda}_{max}$
5000	2000	5200	4220	0.9	1.65
10000	5500	12000	10448	0.7	1.65
20000	13700	26500	24047	0.65	1.5
50000	52000	70000	68800	0.47	0.85
100000	114000	130000	147223	0.47	0.75

Table 3.4. *For a given value of the Rayleigh number R, a single roll (convecton) solution is stable in the range (Q_{min},Q_{max}). Also given is the linear stability boundary $Q_{max}^{(o)}$, the minimum value of Q for which the static conducting solution is stable to perturbations of all wavelengths. Finally, $\bar{\lambda}_{min}$ and $\bar{\lambda}_{max}$ are the minimum and maximum widths of convectons found for each R. In all cases here, $\lambda = 6$, $\sigma = 1$ and $\zeta = 0.1$.*

§3.7. *Varying the Rayleigh Number*

In many cases in theoretical studies of magnetoconvection asymptotic models may be derived which model the behaviour of the system as the Rayleigh number R and the Chandrasekhar number Q tend to infinity together. With this in mind I investigated the circumstances under which convectons might occur as R is varied, for fixed values of the diffusivities $\sigma = 1$ and $\zeta = 0.1$, and the aspect ratio $\lambda = 6$.

Numerical experiments were performed for various values of the Rayleigh number. For a given R the field strength was varied until a single roll, convecton solution was obtained. Q was then increased by a small amount and the experiment repeated using the previous solution as a starting point. The new size and nature of the convecton were noted and Q was increased further. This was continued until the convecton solution was no longer stable. This whole sequence of steps was then repeated, except that the field strength was decreased sequentially until the single roll solution lost stability. In this way, for a given R, the full range of values of Q at which a single convecton is stable was found. The results are given in Table 3.4.

For each of the cases $R \leq 50000$ the convecton solutions end when the solution suddenly falls onto the (stable) trivial state at $Q = Q_{max}$. Consequently, in these cases $Q_{max} > Q_{max}^{(o)}$. However, for $R = 100\,000$ the single roll branch terminates at $Q_{max} < Q_{max}^{(o)}$ when the convecton is swamped by the magnetic field and several weak oscillations replace it filling approximately half of the box. Experiments were

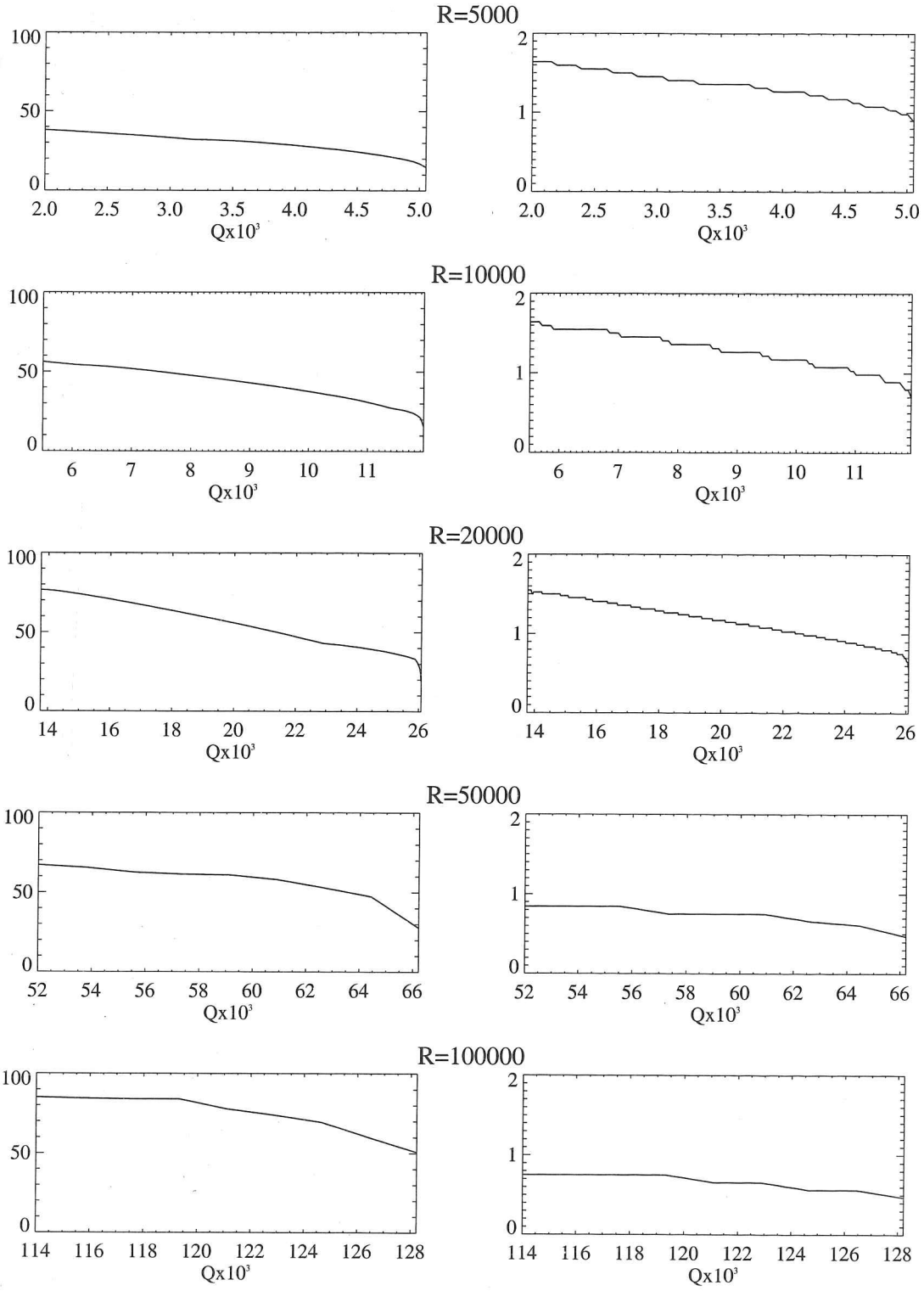

Figure 3-14. *The maximum velocity (left) and width of convecton (right) over the whole range of Q for which the single convecton solution is stable. The graphs are given for five different values of the Rayleigh number R, and $\lambda = 6$ throughout. Both the velocity and width are given in dimensionless units.*

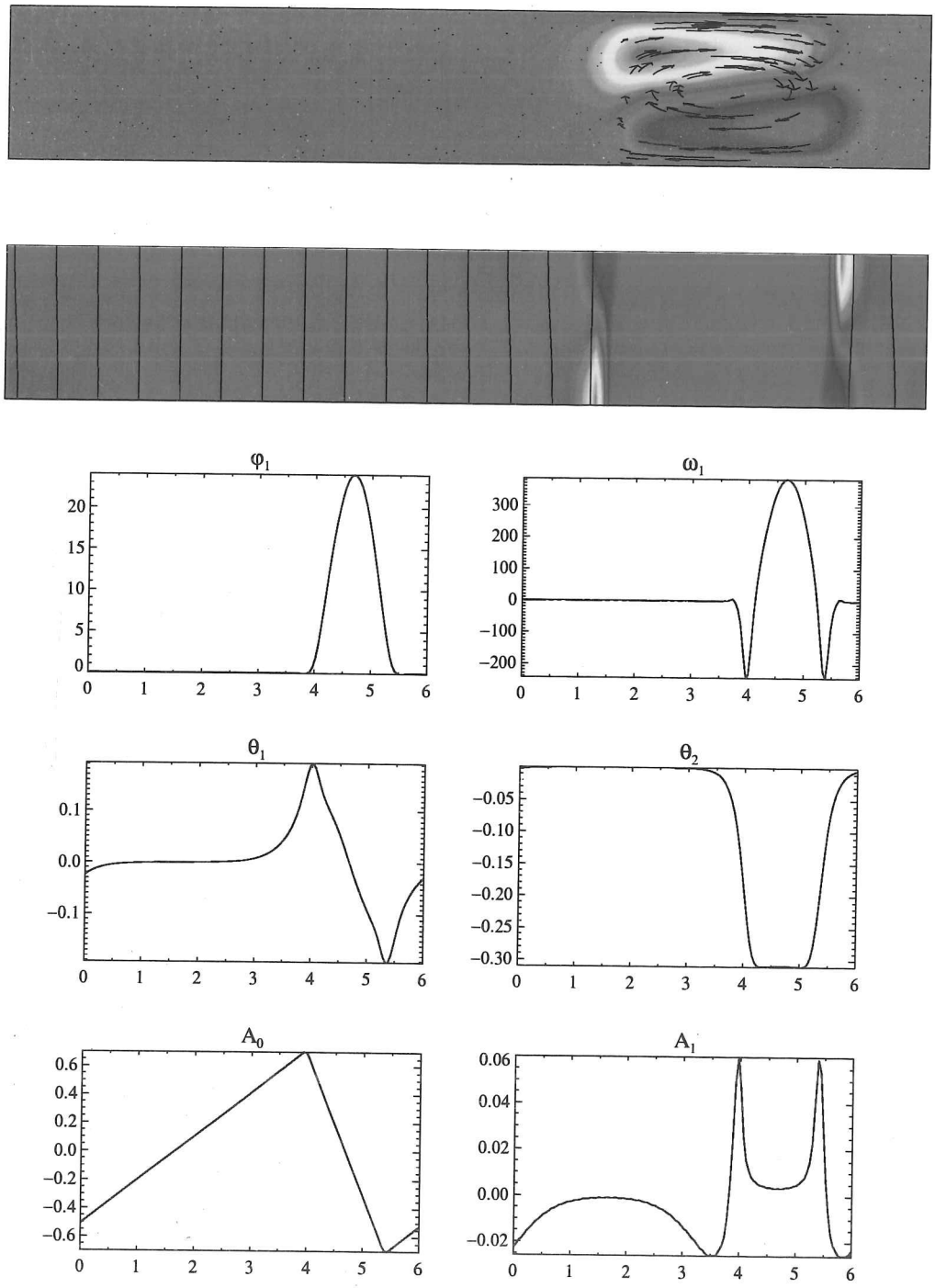

Figure 3-15. *One of the widest convectons ($\bar{\lambda} \approx 1.5$) found in the numerical runs. Here, $R = 20000$, $Q = 14000$, $\lambda = 6$. The top frame shows temperature deviation θ with velocity arrows, the second gives magnetic field strength with field lines, and below the modes (defined in §3.1) are plotted.*

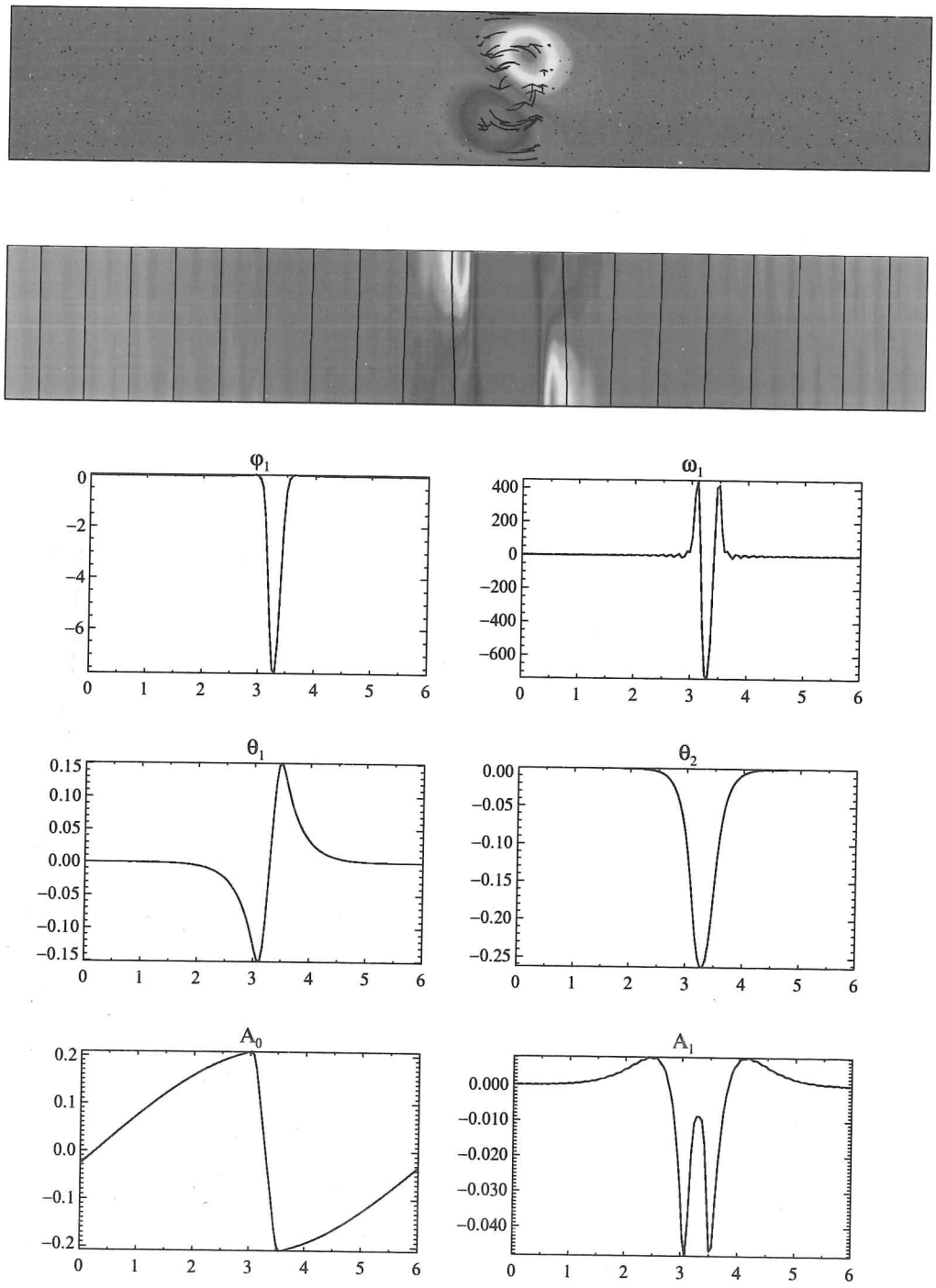

Figure 3-16. *One of the smallest convectons* ($\bar{\lambda} \approx 0.47$) *found in the numerical runs. Here,* $R = 100\,000$, $Q = 130\,000$, $\lambda = 6$. *For explanation see Figure 3-15.*

also conducted for $R > 100\,000$ but no fully isolated states were found, as some residual weak unsteady convection always occupies the region of highest magnetic field strength. Numerical resolution is of course increased accordingly as R is increased to ensure that all important features were fully resolved. For $R < 5000$ isolated convectons were also found right down to $R = 1500$, but convection is extremely feeble, and the extent of the roll is poorly defined. Their width is $\bar{\lambda} \approx 1.85$.

At the other end of the range, as Q is decreased, the isolated convecton solution always ends when weak, low wavelength oscillations appear in the static magnetic region. If Q is decreased further, these oscillations grow in amplitude and then encroach upon, and finally destroy the steady convecton. Prior to the appearance of these oscillations, their onset may be predicted as follows. If the convecton has width $\bar{\lambda}$ all the magnetic field is collected into a region of width $\lambda - \bar{\lambda}$. As Q scales as the square of the magnetic field strength (3.8), the effective field strength in this magnetic region is thus $Q_{\text{eff}} = Q\lambda^2/(\lambda - \bar{\lambda})^2$. While $Q_{\text{eff}} > Q^{(o)}_{max}$ no convection will occur in this region, but when Q is reduced so that $Q_{\text{eff}} < Q^{(o)}_{max}$ weak oscillations will occur with the preferred wavelength. This happens at a value of $Q = Q^{(o)}_{max}(\lambda - \bar{\lambda})^2/\lambda^2$. In practice the width of the convecton actually increases as the field strength is decreased. This may be seen in Figure 3-14. For $\lambda = 6$ and $R = 20000$ a typical value for the width for low values of Q is $\bar{\lambda} \approx 1.5$, which predicts that the oscillations will begin at $Q \approx 13500$, relatively close to the observed value of $Q_{min} \approx 13700$.

The graphs in Figure 3-14 show how the width of convectons varies with field strength for various values of R. In each case we can see that the width of the roll varies by a factor of around 2. For $R = 20000$, for example, the maximum and minimum widths are approximately 1.5 and 0.65 which occur at Q_{min} and Q_{max} respectively. These values are also given in Table 3.4.

Also shown in Figure 3-14 is the maximum velocity within the convective roll as a function of Q. As expected, this measure of convective efficiency decreases significantly as Q increases and the roll is slowly squeezed out of existence by the magnetic field.

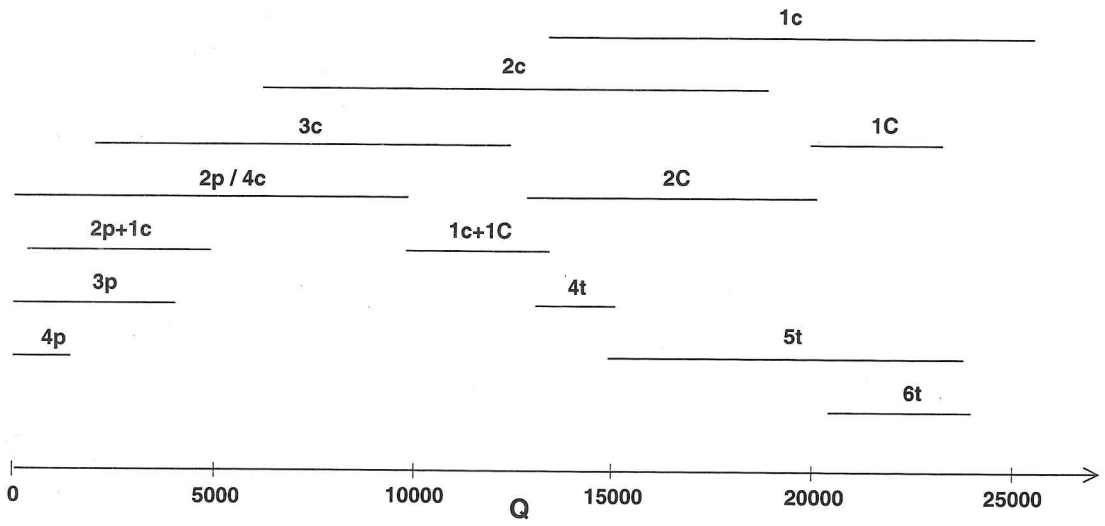

Figure 3-17. *The range of Q over which various solutions are stable for the case $\lambda = 6$, $R = 20000$ ($Q_{max}^{(o)} = 24047$) demonstrating that several convective patterns coexist at any parameter value. 'p' represents (non-isolated) steady plumes, 'c' steady convectons, 'C' oscillatory convectons, and 't' (non-isolated) oscillatory cells. For example, '2p+1c' shows the range of stability of the branch consisting of two plumes (wavenumber $m = 2$; 4 rolls) and one steady convecton. There are many more solution branches, and only the most important have been plotted.*

§3.8. *Existence of multiple solutions*

The results of the last section make it clear that convectons are associated with hysteresis; for fixed values of the parameters several different stable solutions may be obtained depending on the initial state. For $R = 20000$ I have already established (in §3.7) that at $Q = 16000$ the solutions consisting of a single convecton, and that with two convectons are both stable. Moreover if the experiment is performed with the initial state being random small perturbations of varying wavelengths then the time-dependent solution with 5 pairs of oscillating plumes ($m = 5$) is obtained. Investigations were made to try to establish the full range of convective patterns that coexist at a particular value of Q. In each case, when a solution was found, the run was repeated with a slightly higher value of Q, and using the previous final solution as the starting point. This was repeated until the solution was no longer stable. Having done this, the same process was followed except that Q was decreased. In this way Figure 3-17 was constructed, which shows the main convective patterns for the case $\lambda = 6, R = 20000$, and the range of values of Q for which they are found to be stable. The figure is of course incomplete, as there are many more complicated irregular solutions particularly for low values of the field strength ($Q < 10000$),

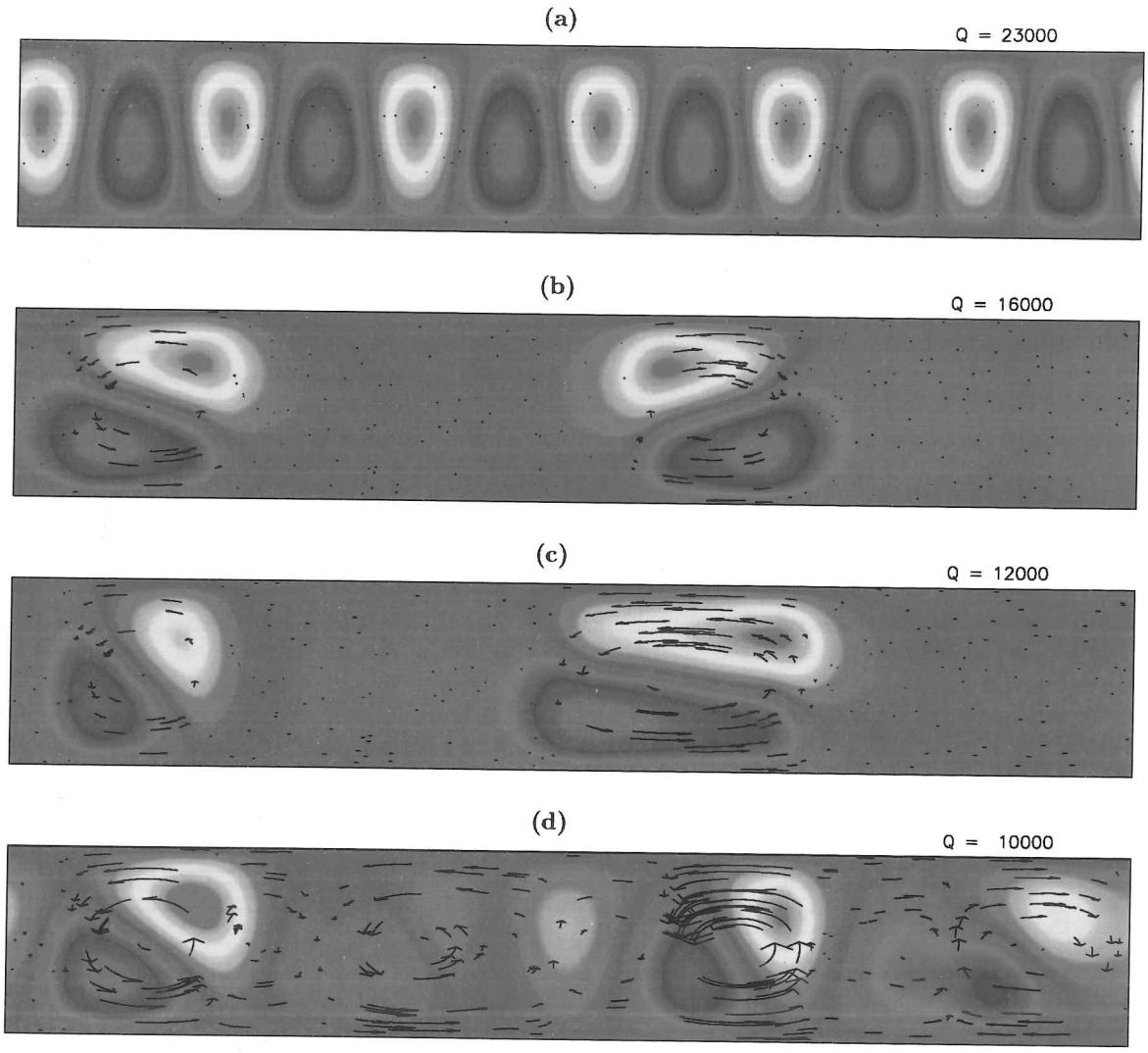

Figure 3-18. *Several more convective patterns found in investigations of the case $\lambda = 6$, $R = 20000$. (a) low amplitude periodic oscillations of wavenumber $m = 6$ (the 6t branch), (b) two symmetric (steady) convectons (the $2c_o$ branch), (c) one steady convecton (right) and one oscillatory convecton $(1c + 1C)$, (d) irregular unsteady convection.*

mainly consisting of a number of steady rolls of differing sizes filling one region of the box, and another number of oscillatory cells in the remainder.

The observed states fall into three main categories, isolated states, non-isolated steady states and non-isolated oscillatory states, although the boundaries between the three are at best unclear. The non-isolated steady states occur at low field strength ($Q < 5000$ say), and are associated with the pitchfork bifurcations to pairs of steady rolls. For example the $4p$ solution of four pairs of steady rolls (see Figure 3-2(a),(b)) has its origins at the (supercritical) pitchfork bifurcation at $Q_4^{(e)} = 1221$. As Q is increased symmetry-breaking bifurcations cause some of the rolls to be suppressed, and we undergo a transition to the isolated states, and convectons. The bifurcation sequence that may lead to the stability of convectons is discussed in §3.10. Non-isolated oscillatory states, on the other hand, are stable only for high values of the field strength. Linear theory (§3.2) predicts that the trivial state first becomes unstable (as Q is decreased for constant R) at $Q_6^{(o)} = 24047$ to perturbations with $m = 6$. This results in the solution with six pairs of oscillatory standing wave rolls (Figure 3-18(a)) labelled $6t$ in Figure 3-17. Again these solutions can undergo bifurcations that break the translational and reflectional symmetries to lead to isolated oscillatory states (labelled $1C, 2C$) which are discussed in the next section.

Comparing Nusselt numbers for the different states, the steady convecton solutions have a higher Nusselt number than isolated oscillatory rolls for a given value of Q (where the peak Nusselt number N is taken in the time-dependent case). Similarly, all the isolated states are convectively more efficient than the non-isolated standing wave solutions. For the case of convectons, the Nusselt number increases with the number of convectons present, for fixed Q, as one might expect (velocities in each convecton of a $2c$ solution are comparable to those in a $1c$). Conversely, for the non-isolated steady states N is greater when there are fewer pairs of rolls, as there are fewer stagnant flux sheets.

When starting from an isolated solution and decreasing Q, the solutions always end with weak oscillations appearing in the region of high magnetic field strength. The value of Q at which this occurs is consistent with the discussion of Q_{eff} in §3.7.

If an experiment is commenced from the trivial static state with small random perturbations added then the outcome is generally the solution with the lowest Nusselt number that exists for that particular value of Q. For high Q (> 14000) this is the non-isolated oscillatory states ('t') and for low Q (< 2000) the steady plumes ('p'). At intermediate values a turbulent mix of steady and time-dependent

rolls is obtained which interact in an irregular way. No isolated states are formed in this way.

The calculations reproduce some of the behaviour seen in the full compressible case; one sees both steady and oscillatory convection for certain values of Q close to onset, and in these cases the flow is in the form of a number of convective cells. The field is predominantly uniform, with only small fluctuations from its initial vertical state, and areas of high field strength are associated with regions of weaker convection as before. As in the compressible case, stable 'flux-separated' states have been located, and although they are manifestations of the same physical phenomenon, they seem to occur in different sections of parameter space; the flux-separated states of §2.2.3 occur at low values of Q whereas convectons in the incompressible case are found at higher values of the imposed field strength.

§3.9. *Oscillatory Convectons*

Among the new types of behaviour seen during the investigations in §3.8 is a single isolated *oscillatory* roll (Figure 3-19). Much like the convecton it is fully isolated from the magnetic field with no convection occurring in the region of high field strength. A typical example at $Q = 22000$ has a width of $\bar{\lambda} \approx 0.9$ and Nusselt number equal to 1.20 at the peak of the oscillation. By way of comparison, for a steady convecton at $Q = 22000$, $\bar{\lambda} \approx 1.0$ and the Nusselt number is 1.31.

§3.10. *Discussion of the bifurcation sequence*

Ordinarily in thermal convection steady fluid flow occurs as a number of *plumes* which consist of fluid rising (or falling) and moving horizontally outwards in both directions seen as two roughly circular rolls. They are characterised by horizontal mirror symmetry about their centre and examples may be seen in Figure 3-2(a)–(c). *Convectons* are a novel and important departure from this in that the system has undergone a bifurcation that removes the final reflection symmetry so that flow consists solely of a single roll, whilst retaining the usual Boussinesq point symmetry.

Some results are developed in Figure 3-20 which shows the sequence of bifurcations which may give rise to convectons. Very many more solution branches exist within the problem, but only a few key branches have been included. There are pitchfork bifurcations at $Q_1^{(e)} = 190$ and $Q_2^{(e)} = 603$ (among others) corresponding to steady convection of two (wavenumber $m = 1$) and four ($m = 2$) rolls (Figure 3-2(b)) respectively. Due to the ability of a conducting fluid to expel magnetic flux, which leads to regions of reduced effective field strength, these branches

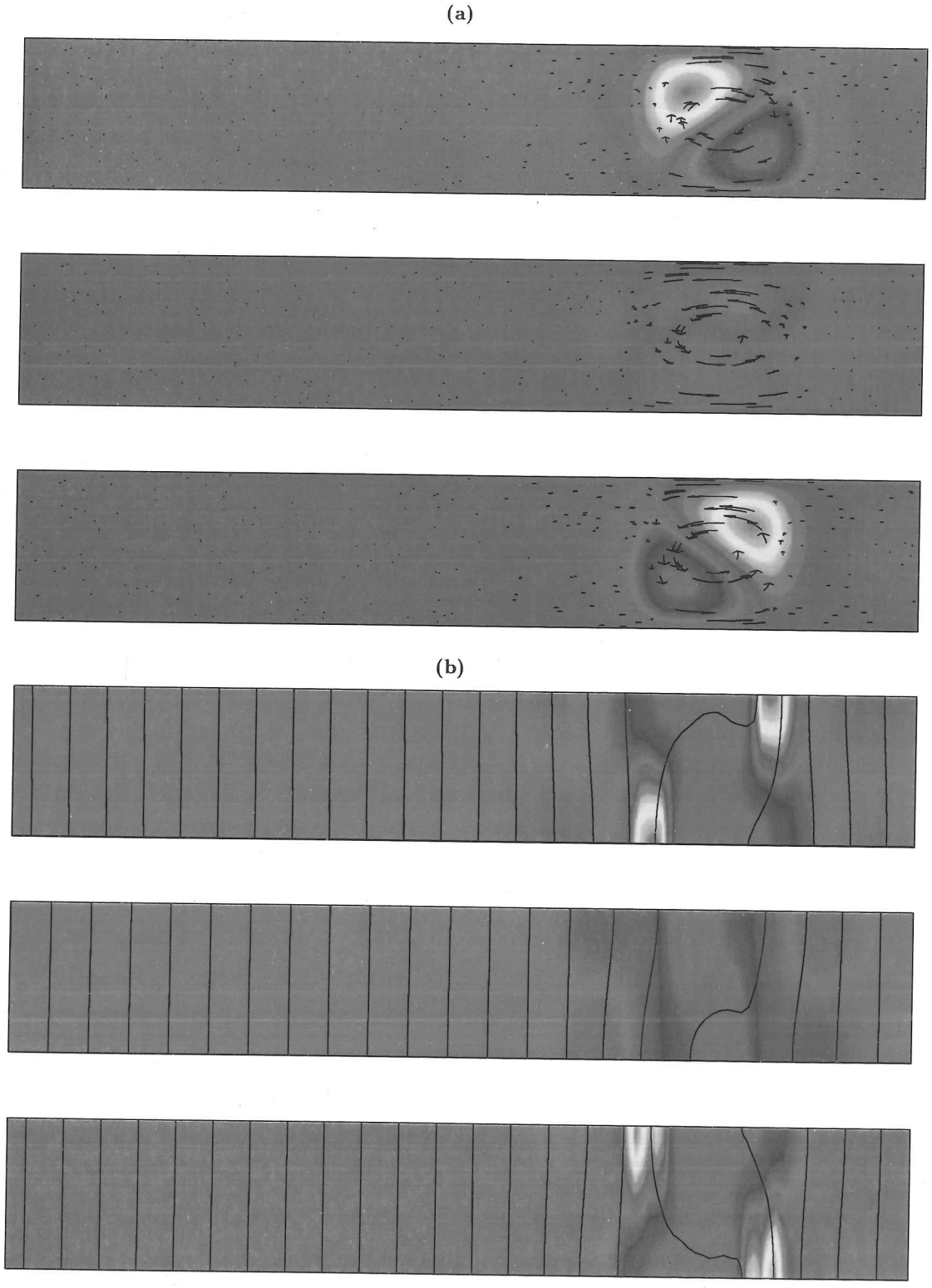

Figure 3-19. *An example of an oscillatory convecton for the case* $\lambda = 6$, $R = 20000$, $Q = 22000$. *(a) shows temperature deviations* θ *at times* $t = 0, T/4, T/2$ *where* T *is the period of oscillation. (b) shows magnetic field strength* B^2 *and field lines for the snapshots in (a).*

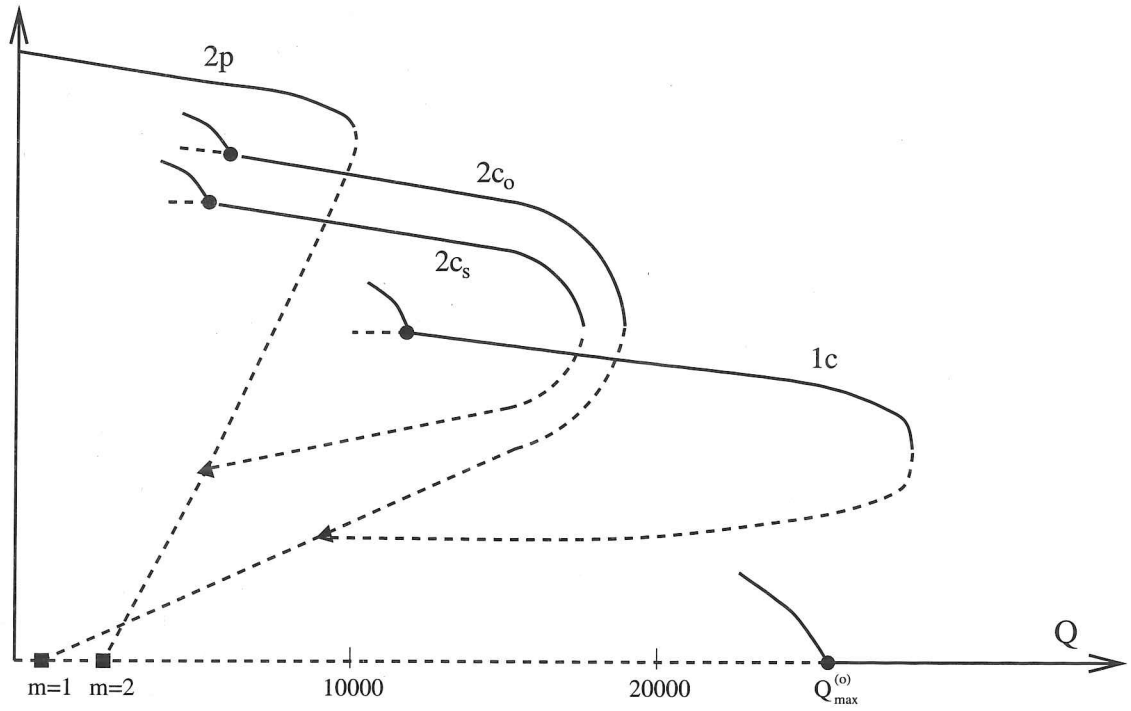

Figure 3-20. *A schematic representation of part of the bifurcation sequence leading to the production of convectons for $\lambda = 6$. Field strength is plotted horizontally and a measure of the amplitude of convection vertically. Solid lines represent observed stable solutions, and dashed lines are conjectural unstable branches. Squares, circles, and triangles show 'steady', 'Hopf', and 'symmetry-breaking' bifurcations (as discussed in the text) respectively. The number of convective rolls on each branch is shown.*

show subcriticality (Proctor & Weiss 1990), and eventually gain stability at saddle-node bifurcations. The $m = 1$ branch results in two isolated convectons whose vorticities have opposite signs (labelled $2c_o$), as in Figure 3-4(b) or Figure 3-18(b). Steady solutions of two isolated convectons with vorticities of the same sign ($2c_s$) are also found, which result from a symmetry breaking of the $m = 2$ branch (see Figure 3-10(b) or Figure 3-11(h)). The key bifurcation occurs as a symmetry breaking of the $m = 1$ branch, in which the Z_2 reflection symmetry is lost, whilst retaining point symmetry. This branch gives rise to the single convecton solution and such a bifurcation has not been previously observed in studies of convection. Previously, all isolated states found in two-dimensional magnetoconvection have been part of a system of two or more dependent rolls. For example in Weiss (1981) the imposed mirror (Z_2) symmetry of the problem means that Figure 8(d) of Weiss (1981) shows a solution lying on the steady $m = 1$ branch, lacking the extra symmetry breaking required to produce a convecton. Branches arising via a primary pitchfork bifurcation from the trivial solution necessarily retain reflection symmetry (Crawford

& Knobloch 1991), so the branch which gives rise to the single convecton solution can only occur as a secondary bifurcation; Figure 3-20 gives the simplest way in which this can occur. Finally, all three isolated steady branches ($1c$, $2c_o$, $2c_s$) undergo Hopf bifurcations, as the reduction in effective field strength if Q is decreased allows weak oscillations to occur in the magnetic region.

The bistability of trivial and nonlinear solutions is often associated with isolated states, as was discussed in §3.6. This argument carries to the case of $\lambda = 6$; if the *effective* field strength in the magnetic region is plotted on the horizontal axis instead of Q in Figure 3-20 then the Hopf bifurcation at the lower end of the single convecton ($1c$) branch occurs at $Q^{(o)}_{max}$, and convectons always 'coexist' (in terms of *effective* Q) with a stable trivial solution.

§3.11. *Varying the diffusivity*

As is shown in §3.2 the values of the diffusivity ratios ζ and σ do not affect the values $Q^{(e)}_{max}$ below which the steady modes become stable. One would therefore expect that convectons would exist for values of the diffusivities other than those used in §3.4–§3.7 ($\zeta = 0.1$, $\sigma = 1$). Of these, varying ζ should have the greater effect, as its value determines whether the trivial solution first becomes unstable to steady or oscillatory modes. It is also expected, however, that for $\zeta > 1$ the dynamic and time-dependent solutions of the previous and following sections will not be seen as the oscillatory modes never bifurcate from the trivial solution, unlike the case $\zeta = 0.1$.

I repeated the calculations of §3.4 with $\zeta = 1$ (with other parameters unchanged $R = 20000$, $\lambda = 6$, $\sigma = 1$), and the results may be seen in Figure 3-21(a). As expected a similar sequence of patterns is seen, with non-isolated plumes giving way to isolated rolls which reduce in number until only a single convecton remains ($Q > 1280$) before this too is rapidly suppressed by the marauding magnetic field at $Q = 1580$. For comparison, the value of Q below which the trivial solution is unstable is $Q^{(e)}_{max} = 1374$. Similar results are obtained for a much wider box ($\lambda = 16$) in that the number of steady rolls reduces as the magnetic field is increased, with the flux increasingly able to form intermediate regions of high field strength (Figure 3-21(b)). One difference that occurs for both values of λ, however, is that the first bifurcation ($Q \approx 360$ for $\lambda = 6$, and $Q \approx 260$ for $\lambda = 16$) immediately breaks the reflectional (Z_2) symmetry of the system, leaving only a cyclic translational symmetry that was only rarely observed in the earlier case of $\zeta = 0.1$.

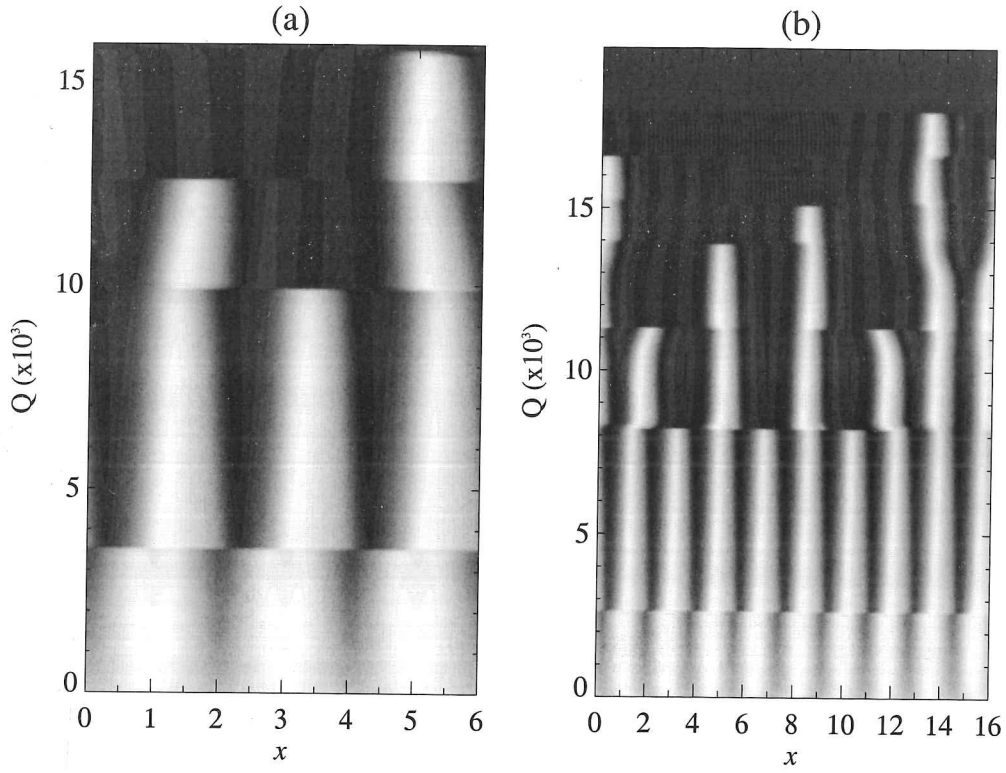

Figure 3-21. *Surface dT/dz for the final solution state of each value of Q, again with $R = 20000$ and $\sigma = 1$, but with $\zeta = 1$. (a) $\lambda = 6$, (b) $\lambda = 16$. In both cases, as Q is increased the convective patterns show similar changes to the case $\zeta = 0.1$ shown in Figure 3-1 and Figure 3-7, with the number of steady rolls decreasing until only one isolated convecton remains.*

The transition from one convective pattern occurs both rapidly and cleanly, with essentially no intermediate transitory period. This is to be expected, given the complete absence of any unsteady modes, as is always true when $\zeta \geq 1$.

§3.12. *Fully resolved case*

Having established the existence of isolated rolls in the truncated model described in §3.1, it is important to verify that they are not a result of the restricted number of modes. There are many examples of convective patterns or regimes in low order models of Rayleigh-Bénard convection that do not translate to the fully resolved case (Curry *et al.* 1984). Numerical experiments were thus repeated for the full nonlinear Boussinesq equations (3.1) in an attempt to reproduce the above behaviour for the case $\lambda = 6$, again fixing $\sigma = 1, \zeta = 0.1$. A pseudo-spectral code due to A.M. Rucklidge was used with periodic horizontal boundary conditions, and the spatial resolution was 256×33 modes in the horizontal and vertical respectively.

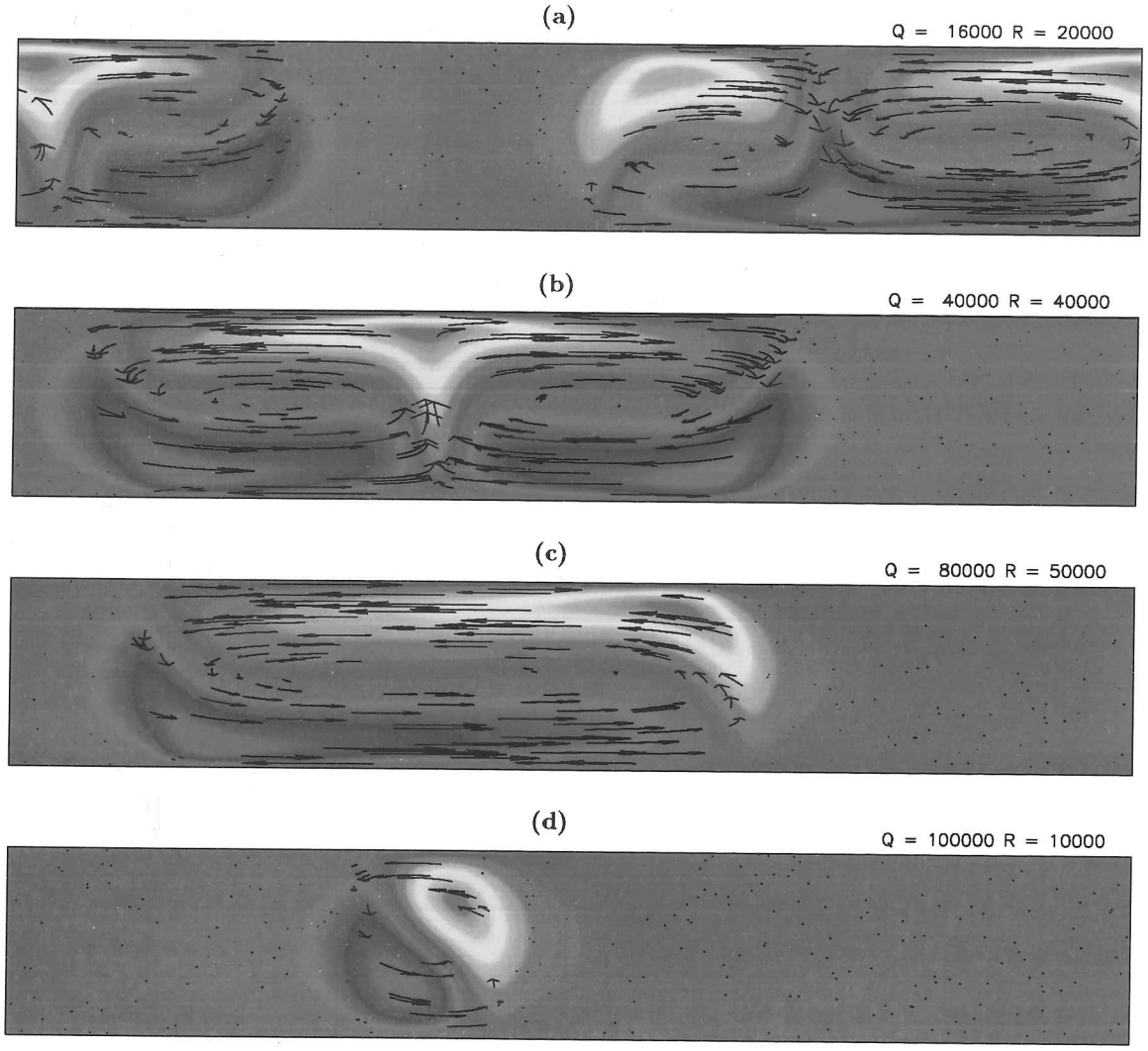

Figure 3-22. *Flux separated states obtained for fully resolved 2-d Boussinesq magnetoconvection. (a) three rolls of different sizes, (b) a single large plume, (c) the largest convecton found, (d) the smallest convecton found. Once again, shading is the temperature deviation from the static background state θ (red-hot, violet-cold), and velocity arrows are shown.*

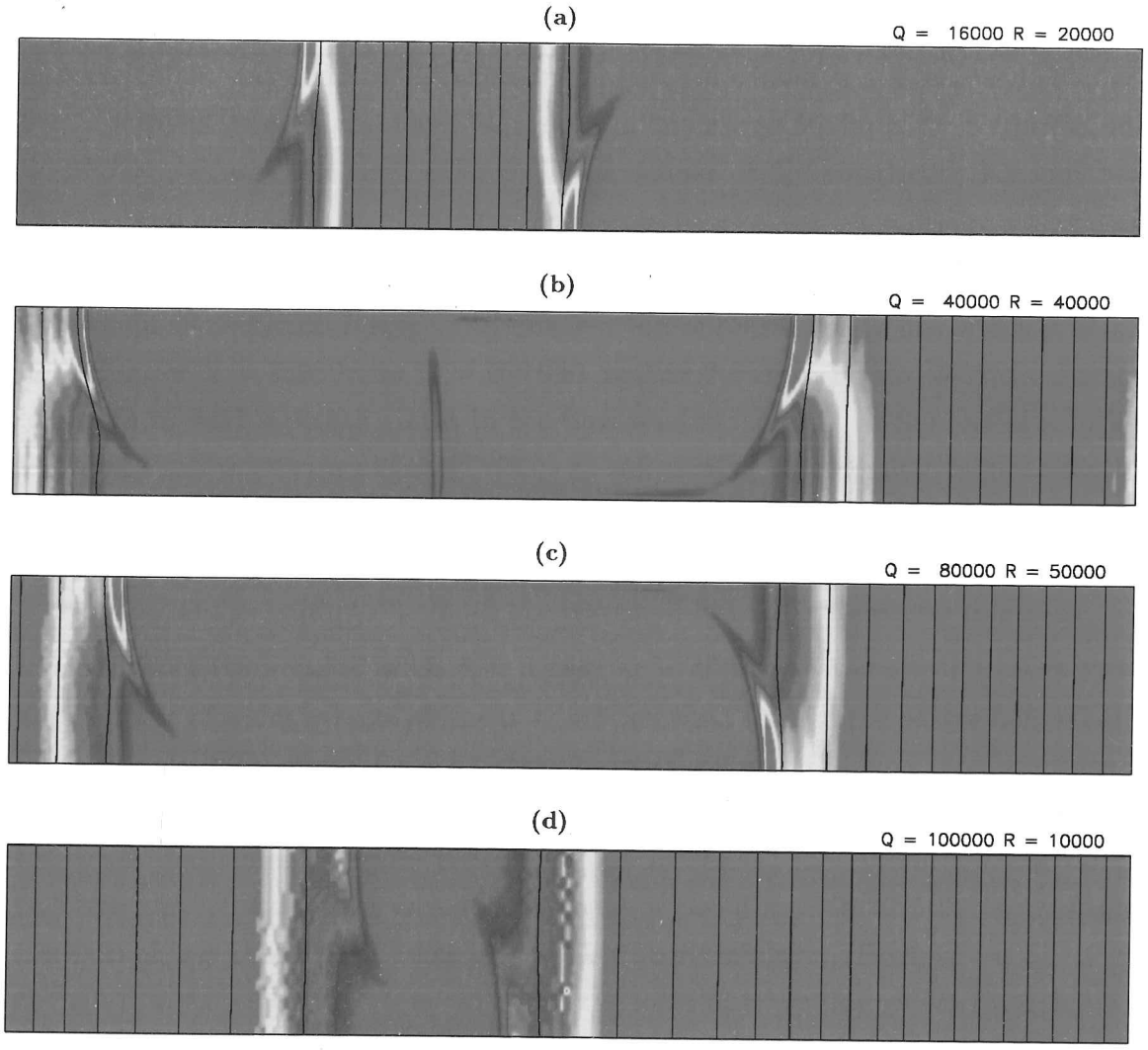

Figure 3-23. *As for Figure 3-22 except that shading is the magnetic field strength and lines of magnetic flux are shown.*

Commencing with a fairly high field strength $Q = 16000, R = 20000$ the flow settled into a state with three convective rolls of differing sizes and an intermediate region of strong magnetic field, even when the earlier 'convecton' state was used as an initial condition (Figure 3-22(a)). However, it was predicted that if this state were used as the starting point for a run with higher Rayleigh number and field strength, weaker rolls would be subsumed into the magnetic region. Thus, for $R = 50000, Q = 80000$ a single convecton was obtained (Figure 3-22(c)). The convection is highly efficient at expelling flux; within the convecton the field strength is again reduced to around a thousandth of its original value. The Nusselt number in this case is 3.51 and the width $\bar{\lambda} \approx 3.2$, the largest so far obtained and much larger than is possible in the truncated case.

As before, the extent of the stability of the convecton can be found by increas-

ing and decreasing the field strength. For $R = 50000$ single convectons are stable for at least $50000 < Q < 150\,000$, before eventually all convection dies away. Similarly for $R = 10000$ convectons have been seen in the range $50000 < Q < 100\,000$, and in addition almost certainly exist for lower values of Q though this has not been investigated.

Increasing field strength and reducing the Rayleigh number both cause a reduction in the convecton size. The smallest roll obtained so far has width $\bar{\lambda} \approx 0.75$ for values of $R = 10000$ and $Q = 100\,000$, and is shown in Figure 3-22(d). Further increases in field strength result in the flow tending rapidly to the trivial solution. Even so, the convectons obtained occur at values of Q significantly higher than the linear stability boundary (for $R = 10000$, $Q^{(o)}_{max} = 10447$). This seems to go against results published by Galloway & Weiss (1981) in which they found that limiting the number of modes tends to increase the extent of linearly subcritical solutions.

Another state found with $R = 40000$, $Q = 40000$ is shown in Figure 3-22(b), and consists of a single large plume in which hot fluid rises in the centre before being forced horizontally outwards. This state is very similar to the 'flux-separated' states seen in §2.2.3, and lacks the exact mirror-symmetry of such plume states seen in the truncated model (Figure 3-4(b)). This increases our confidence that single isolated convectons will be found in the case of two-dimensional fully compressible convection, especially for studies in a weakly stratified layer (Hurlburt *et al.* 1989), though it is expected that they will take the form of travelling waves (Matthews *et al.* 1993).

Increasing ζ to 1 has little effect on the outcome. Convectons are found, however, at lower values of Q than for $\zeta = 0.1$. With $\zeta = 1$ and $R = 30000$, $Q^{(o)}_{max} = 2185$ and convectons are found at $Q = 2000$, the first example of convectons found in the fully resolved case at values of Q for which the trivial state is unstable. The flow is considerably less vigorous ($N_u = 1.93$) than for $\zeta = 0.1$ and the convecton relatively narrow given the low magnetic field strength ($\bar{\lambda} \approx 1.8$). Convectons in fully resolved Boussinesq magnetoconvection have also recently been found independently by P.C. Matthews (private communication) for the case $\zeta = 1$, but they are essentially identical to those found here.

Chapter 4.

Low order models

The full nonlinear partial differential equations of hydrodynamics generally resist attempts to investigate them analytically in all but the most restrictive of circumstances. If we are to apply much of the modern theory of dynamical systems it is first necessary to simplify the equations whilst attempting to retain aspects of the behaviour that we wish to investigate. The usual method is to derive appropriate 'low order' models by removing some of the variables or neglecting various effects to obtain equations simple enough to yield to analysis. In this Chapter I derive two such models for magnetoconvection to try to study the localized states of Chapter 3 in more detail. Firstly, I present a Swift-Hohenberg model via an order expansion of the field variables, and secondly I present an asymptotic model by considering the behaviour as the Rayleigh number becomes arbitrarily large. The work in this Chapter is still under study, and only preliminary results are given.

§4.1. *Swift-Hohenberg type models*

The original Swift-Hohenberg equation (Swift & Hohenberg 1977),

$$\frac{\partial \psi}{\partial t} = r\psi - (1 + \frac{\partial^2}{\partial x^2})^2 \psi - \psi^3 \tag{4.1}$$

was derived as an order parameter equation near the onset of convection in the Rayleigh-Bénard problem. Since then (4.1) and many models derived from it have been studied in great depth, particularly in the ever-expanding field of pattern formation (Cross & Hohenberg 1993). One of its strengths lies in the fact that at a particular parameter value there is a whole band of modes that are simultaneously stable. For a finite domain, this represents only a finite number of stable modes, but as the computational domain becomes arbitrarily large the range of stable modes

becomes a continuous interval. Moreover, through a further reduction in order, the celebrated Landau-Ginzburg equation (Stewartson & Stuart 1971) may be derived from the Swift-Hohenberg model, and which has itself formed the basis of a whole field of study.

An analogue of the standard equation (4.1) has also been derived for the case of rotating convection (Ponty *et al.* 1997). In this section I shall derive a similar equation for the case of convection in a vertical magnetic field, in the hope of using it to locate isolated states, analogous to those seen in Chapter 3.

§4.1.1. *Derivation of model*

I begin once again with the standard two dimensional Boussinesq equations of magnetoconvection that were used in Chapter 3 (Knobloch *et al.* 1981).

$$\frac{\partial \Delta\psi}{\partial t} + \frac{\partial(\psi, \Delta\psi)}{\partial(x,z)} = \sigma\Delta^2\psi + \sigma R\frac{\partial\theta}{\partial x} + \sigma\zeta Q\left(\frac{\partial \Delta A}{\partial z} + \frac{\partial(A, \Delta A)}{\partial(x,z)}\right) \tag{4.2}$$

$$\frac{\partial\theta}{\partial t} + \frac{\partial(\psi,\theta)}{\partial(x,z)} = \Delta\theta + \frac{\partial\psi}{\partial x} \tag{4.3}$$

$$\frac{\partial A}{\partial t} + \frac{\partial(\psi, A)}{\partial(x,z)} = \zeta\Delta A + \frac{\partial\psi}{\partial z} \tag{4.4}$$

where the Jacobian is defined in (3.2) and the Laplacian

$$\Delta \equiv \nabla^2.$$

As in Chapter 3 I have defined θ, A and ψ via (3.3)–(3.5). All other quantities are defined in §3.1. I now eliminate all linear terms in θ and A.

Firstly eliminating θ via $[(\partial_t - \Delta) \times (4.2) - (\sigma R\partial_x) \times (4.3)]$ gives

$$\partial_{tt}\Delta\psi - (1+\sigma)\partial_t\Delta^2\psi + \sigma\Delta^3\psi - \sigma R\partial_{xx}\psi = \sigma\zeta Q\partial_z\Delta(\partial_t - \Delta)A + N_1 \tag{4.5}$$

where N_1 is a nonlinear term in ψ, θ, and A. Now similarly eliminate the linear term in A. $[(\partial_t - \zeta\Delta) \times (4.5) - \sigma\zeta Q\partial_z\Delta(\partial_t - \Delta) \times (4.4)]$ results in

$$\begin{aligned}\partial_{ttt}\Delta\psi - (1+\sigma+\zeta)\partial_{tt}\Delta^2\psi + (\sigma+\zeta+\sigma\zeta)\partial_t\Delta^3\psi - \sigma R\partial_t\partial_{xx}\psi \\ - \sigma\zeta Q\partial_t\partial_{zz}\Delta\psi - \sigma\zeta\Delta^4\psi + \sigma\zeta R\partial_{xx}\Delta\psi + \sigma\zeta Q\partial_{zz}\Delta^2\psi + N_2 = 0\end{aligned} \tag{4.6}$$

in which the nonlinear contributions are given by

$$\begin{aligned} N_2 =& \sigma\zeta Q\partial_z\Delta(\partial_t-\Delta)\frac{\partial(\psi,A)}{\partial(x,z)}+\sigma R\partial_x(\partial_t-\zeta\Delta)\frac{\partial(\psi,\theta)}{\partial(x,z)} \\ &+(\partial_t-\Delta)(\partial_t-\zeta\Delta)\frac{\partial(\psi,\Delta\psi)}{\partial(x,z)}-\sigma\zeta Q(\partial_t-\Delta)(\partial_t-\zeta\Delta)\frac{\partial(A,\Delta A)}{\partial(x,z)}. \end{aligned} \tag{4.7}$$

Now, developing a method introduced in Ponty *et al.* (1997), and assuming that the Prandtl number exceeds the minimum value for which convection is stationary at onset, I define the stress parameter $\epsilon = (R - R_c)/R_c$, for R_c the critical Rayleigh number. Analysis obtained from invoking the standard boundary conditions (3.9) and examining an expansion of the form

$$\psi(x,z,t) = \epsilon^{\frac{1}{2}}\psi_1(x,z,t) + \epsilon\psi_2(x,z,t) + \epsilon^{\frac{3}{2}}\psi_3(x,z,t) + \ldots \tag{4.8}$$

(with similar expansions for θ and A) gives the familiar result (Knobloch *et al.* 1981) that $\psi_2 = \partial_z A_2 = \partial_x\theta_2 = 0$, and

$$\begin{aligned} \psi(x,z,t) &= \epsilon^{\frac{1}{2}}\psi_1(x,t)\sin\pi z + \epsilon^{\frac{3}{2}}\psi_{31}(x,t)\sin\pi z + \epsilon^{\frac{3}{2}}\psi_{33}(x,t)\sin 3\pi z + \ldots \\ \theta(x,z,t) &= \epsilon^{\frac{1}{2}}\theta_1(x,t)\sin\pi z + \epsilon\theta_2(t)\sin 2\pi z + \epsilon^{\frac{3}{2}}\theta_{31}(x,t)\sin\pi z \\ &\qquad + \epsilon^{\frac{3}{2}}\theta_{33}(x,t)\sin 3\pi z + \ldots \\ A(x,z,t) &= \epsilon^{\frac{1}{2}}A_1(x,t)\cos\pi z + \epsilon A_0(x,t) + \epsilon^{\frac{3}{2}}A_{31}(x,t)\cos\pi z \\ &\qquad + \epsilon^{\frac{3}{2}}A_{33}(x,t)\cos 3\pi z + \ldots \end{aligned} \tag{4.9}$$

This Galerkin expansion may now be substituted into (4.2)–(4.4) and (4.6). It is assumed that time derivatives are $O(\epsilon)$ and that the convective pattern is dominated by slowly modulated rolls with wave number equal to k_c. This implies that the operator ∂_{xx} will reduce to multiplication by $-k_c^2$ at leading order. However, when ∂_{xx} acts on slowly varying quantities it will result in a contribution of $O(\epsilon^{\frac{1}{2}})$. For example, the substitution $\partial_{xx}\psi_1 = (-k_c^2 + \epsilon^{\frac{1}{2}}\mathcal{L})\psi_1$ my be made. In this way subdominant terms may be retained at higher orders in epsilon.

Firstly, substituting (4.9) into (4.6) and projecting onto the $\sin\pi z$ mode, results at $O(\epsilon^{\frac{1}{2}})$ in the familiar dispersion relation of linear theory (§3.2),

$$R_c = (k_1^6 + \pi^2 k_1^2 Q)/k_c^2, \tag{4.10}$$

where $k_1^2 = k_c^2 + \pi^2$. Minimizing this over k_c gives

$$(k_c^2 + \pi^2)^2(2k_c^2 - \pi^2) = \pi^4 Q. \tag{4.11}$$

Moreover, substitution of (4.9) into (4.3) and (4.4) give, at leading order, (primes represent derivatives in the x-direction)

$$\psi_1' - k_1^2\theta_1 = 0 \tag{4.12}$$

$$\pi\psi_1 - \zeta k_1^2 A_1 = 0. \tag{4.13}$$

Projection of (4.3) onto the second Galerkin mode $\sin 2\pi z$ at $O(\epsilon)$ gives an equation for θ_2 in terms of ψ_1 and θ_1

$$2k_2^2\theta_2 + \pi(\psi_1'\theta_1 - \psi_1\theta_1') = 0, \tag{4.14}$$

where $k_2^2 = k_c^2 + 4\pi^2$. This combined with (4.12) gives that

$$\theta_2 = -\frac{\pi}{2k_1^2k_2^2}(k_1^2\psi_1^2 + \psi_1'^2), \tag{4.15}$$

which is consistent with the fact that $\theta_2' = 0$. Nextwise, projection of (4.4) onto the constant mode at $O(\epsilon)$ results in a similar equation for A_0, the mean field contribution to A.

$$2\zeta k_c^2 A_0 - \pi(\psi_1' A_1 + \psi_1 A_1') = 0 \tag{4.16}$$

which with (4.13) becomes

$$A_0 = \frac{\pi^2}{\zeta^2 k_c^2 k_1^2}\psi_1\psi_1' \tag{4.17}$$

Similarly projection of (4.2) and (4.3) onto $\sin 3\pi z$ and (4.4) onto $\cos 3\pi z$ give, after substitution, formulae for half of the third order modes.

$$\psi_{33} = \frac{R_c\pi^2 k_c^2}{\mu(k_c)}(k_c^2\psi_1^3 + \psi_1\psi_1'^2) \tag{4.18}$$

$$\theta_{33} = \frac{\pi^2}{\mu(k_c)}(k_3^4 + 9\pi^2 Q)(\psi_1'^3 + k_c^2\psi_1^2\psi_1') \tag{4.19}$$

$$A_{33} = \frac{3\pi^3 R_c k_c^2}{\zeta k_3^2 \mu(k_c)}(k_c^2\psi_1^3 + \psi_1\psi_1'^2) \tag{4.20}$$

where $k_3^2 = k_c^2 + 9\pi^2$ and

$$\mu(k_c) = 2k_1^2 k_2^2 (k_3^6 + 9\pi^2 k_3^2 Q - k_c^2 R_c) \tag{4.21}$$

No equivalent formulae are available for ψ_{31}, θ_{31}, and A_{31}, as projecting onto $\sin \pi z$ or $\cos \pi z$ at $O(\epsilon^{\frac{3}{2}})$ includes terms involving the time-derivatives of ψ_1, θ_1, and A_1. However, if (4.6) is projected onto $\sin \pi z$ at $O(\epsilon^{\frac{3}{2}})$ then all terms in ψ_{31} cancel and find

$$\begin{aligned}[\sigma k_c^2 R_c - \sigma\zeta\pi^2 k_1^2 Q - k_1^6(\sigma + \zeta + \sigma\zeta)]\dot{\psi}_1 + \sigma\zeta[k_c^2 k_1^2 R_c + (R_c - \pi^2 Q - 6k_1^4)\mathcal{L}^2]\psi_1 \\ + \sigma\zeta\pi k_1^2[k_c^2 R_c \psi_1 \theta_2 - \pi k_1^2 Q A_0'(\psi_1 + \zeta\pi A_1)] = 0,\end{aligned} \tag{4.22}$$

where the dot indicates differentiation by slow time variable, $\tau = \epsilon t$. Finally, substitution of (4.13), (4.15), (4.17), and using the fact that $\epsilon^{\frac{1}{2}}\mathcal{L}\psi_1 = (\partial_{xx} + k_c^2)\psi_1$, leads us to a closed evolution equation for ψ_1,

$$\kappa\dot{\psi}_1 = (k_c^2 R_c - \nu(\partial_{xx} + k_c^2)^2)\psi_1 - c_1\psi_1^3 - c_2\psi_1\psi_1'^2 \tag{4.23}$$

with

$$\begin{aligned}\kappa &= k_1^4(1 + \sigma^{-1}) + \pi^2 Q(1 - \zeta^{-1}) \\ \nu &= \frac{(6k_1^4 + \pi^2 Q - R_c)}{\epsilon} \\ c_1 &= \frac{\pi^2}{2\zeta^2 k_1^2 k_2^2}(\zeta^2 k_c^4 R_c - 2\pi^2 k_2^2(k_1^2 + \pi^2)Q) \\ c_2 &= \frac{\pi^2}{2\zeta^2 k_c^2 k_1^2 k_2^2}(\zeta^2 k_c^4 R_c + 2\pi^2 k_2^2(k_1^2 + \pi^2)Q)\end{aligned} \tag{4.24}$$

The equation (4.23) is an example of the much studied Swift-Hohenberg type (Swift & Hohenberg 1977). Much of the study of the equation (eg Manneville 1990) has been in the context of infinite Prandtl number flow (in the absence of a magnetic field). In this case, if the equivalent of (4.23) is derived using a similar method, the analysis results in

$$\dot{\psi}_1 = \left[k_1^2 - \frac{3}{\epsilon k_1^2}(\partial_{xx} + k_c^2)^2\right]\psi_1 - \frac{\pi^2}{2k_2^2}[k_c^2\psi_1^3 + \psi_1\psi_1'^2] \tag{4.25}$$

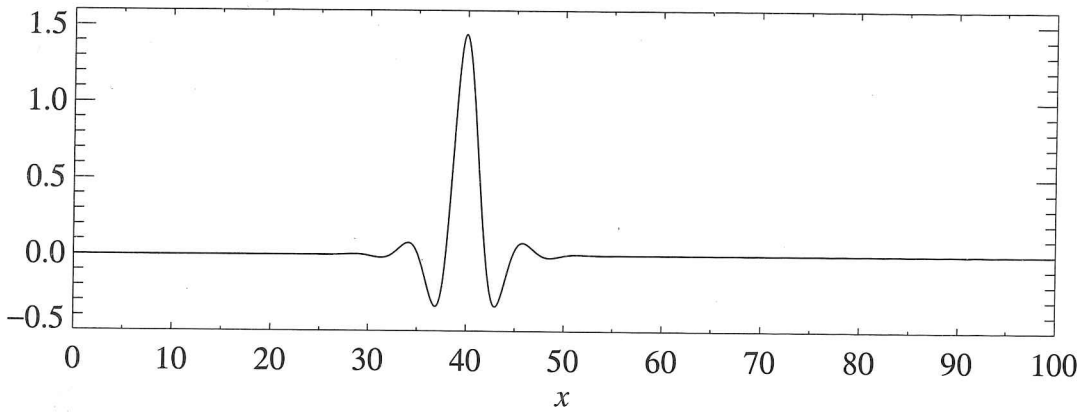

Figure 4-1. *A localized solution found for the quintic Swift-Hohenberg equation, with parameters* $a = -1.4, b = 3, c = 1, d = 1$, *and width* 100.

§4.1.2. Results

Several previous studies have located isolated states in Swift-Hohenberg type models (Sakaguchi & Brand 1996, 1997, 1998). However, these all require the inclusion of a quintic term, with a coefficient chosen to be stabilizing, in order to add hysteretic behaviour of two stable coexisting spatially homogeneous states - the trivial solution and a constant finite solution. Further investigations conclude that the cubic term of the form $\psi\psi'^2$ has only a minor effect on the range of solutions. The appropriate equation to study here is one of the form,

$$\dot{\psi} = a\psi + b\psi^3 + c\psi^5 + d(\partial_{xx} + 1)^2\psi \tag{4.26}$$

after rescaling. Sakaguchi & Brand (1996) obtained stable isolated solutions with parameter values $a = -1.4, b = 3, c = 1, d = 1$. Using Fourier Transform methods in a periodic box of width 100 and implicit timestepping, I have obtained similar isolated states at these values, and a typical state may be seen in Figure 4-1.

My work with Swift-Hohenberg type models is still incomplete, but the hope is to derive a two field model in which one field represents the stream function and the second the magnetic flux function. Interaction will come through gradient coupling representing advection, a process which often leads to the formation of stable localized solutions (Riecke 1998).

In many circumstances simplified models may be derived from complicated systems through considering the behaviour of the system in the limit as one of the parameters becomes arbitrarily large or small (Busse & Clever 1981, etc).

For the case of two-dimensional magnetoconvection under the Boussinesq approximation a common simplification is to consider the behaviour for infinite Prandtl number ($\sigma \to \infty$). In addition it is often useful to derive an asymptotic model as the Rayleigh number or Chandrasekhar number is allowed to tend to infinity (Umemura & Busse 1989, Matthews 1999).

Following a derivation of M.R.E. Proctor (private communication), I present such an asymptotic model for the case of steady convection with infinite Prandtl number. I begin once again with the equations of two-dimensional Boussinesq convection in the presence of an imposed vertical magnetic field,

$$\begin{aligned} &\psi_{xxxx} + 2\psi_{xxzz} + \psi_{zzzz} + R\theta_x \\ &\quad + \zeta Q \left(A_{xxz} + A_{zzz} + A_x A_{xxz} + A_x A_{zzz} - A_z A_{xxx} - A_z A_{xzz}\right) = 0 \end{aligned} \tag{4.27}$$

$$\psi_x \theta_z - \psi_z \theta_x = \theta_{xx} + \theta_{zz} + \psi_x \tag{4.28}$$

$$\psi_x A_z - \psi_z A_x = \zeta(A_{xx} + A_{zz}) + \psi_z \tag{4.29}$$

where subscripts denote partial differentiation in the usual way, and all quantities are defined in §3.1. Now consider the case $\zeta \ll 1$ and let R and Q become arbitarily large whilst the ratio R/Q remains constant. I thus introduce a small parameter ϵ defined via

$$R = \epsilon^{-4}, \quad Q = q\epsilon^{-4}. \tag{4.30}$$

Attempting to locate an isolated solution in an arbitrarily wide computational box, it is thus necessary to rescale the horizontal variable x so that the new variable X may vary on a length scale of $O(1)$. Accordingly, define

$$x = \epsilon X. \tag{4.31}$$

The appropriate rescalings for the dynamic variables are

$$\begin{aligned} A &= \epsilon \tilde{A} \\ \psi &= \zeta \epsilon^{-1} \tilde{\psi} \\ \theta &= \zeta \tilde{\theta}. \end{aligned} \tag{4.32}$$

Substituting (4.30)–(4.32) into (4.28) and taking the leading order in ϵ results in

$$\tilde{\theta}_{XX} + \tilde{\psi}_X = 0 \tag{4.33}$$

from which it may be assumed that

$$\tilde{\theta}_X = -\tilde{\psi}. \tag{4.34}$$

Finally, substitution of (4.30)–(4.32) into (4.27) & (4.29), and using (4.34) gives, at leading order,

$$\begin{aligned} \tilde{\psi} - \tilde{\psi}_{XXXX} + q\left(\tilde{A}_z\tilde{A}_{XXX} - \tilde{A}_{XXz}(1+\tilde{A}_X)\right) &= 0 \\ \tilde{\psi}_X\tilde{A}_z - \tilde{\psi}_z\tilde{A}_X &= \tilde{A}_{XX} + \tilde{\psi}_z \end{aligned} \tag{4.35}$$

For an isolated solution we must impose the boundary condition that the flow approximates to the trivial solution far away from the region of convection,

$$\tilde{\psi} \to 0\,, \quad \tilde{A}_X \to 0 \quad \text{as } X \to \pm\infty. \tag{4.36}$$

It is hoped that the solution of (4.35) in very wide boxes will succeed in locating stable isolated solutions analogous to the convectons of Chapter 3. The reduction in complexity of the equations may permit a more detailed analysis of the process that results in the formation of localized solutions, and exhibit the behaviour of such solutions as the Rayleigh number becomes arbitrarily large.

My work in investigating the phenomenon of localized solutions through the use of low order 'toy' models is still ongoing, but forms a very important area of my studies. There is clearly much that is not known about the processes involved in the production of stable, fully-isolated states, particularly with respect to magnetoconvection, but chances are that analytic investigations of an appropriate low order model will hold many of the answers.

Chapter 5.

A three-dimensional truncation

§5.1. Derivation of the model

In Chapter 3 I investigated the range of spatial patterns that may be obtained in a two-dimensional box. In particular it was observed that in the presence of a magnetic field in a sufficiently wide box, the flow is able to sweep the magnetic flux into a separate static region, leaving a steady convecting field-free region. A key example of this is the convecton seen in §3.6. These 2D investigations do improve our understanding of the interaction between magnetic fields and convection at the surfaces of stars like the Sun, but they should really be regarded as necessary preliminaries to more realistic 3D experiments. It is thus natural to ask how such isolated states would translate to the case of three spatial dimensions, and indeed what form such states would take.

Following the example of Chapter 3, consider once again a perfect conducting fluid under the standard Boussinesq approximation. The computational domain is now the cuboid with square planform defined by $\{0 \leq x \leq \lambda,\, 0 \leq y \leq \lambda,\, 0 \leq z \leq 1\}$, where again $z = 0$ at the base of the box.

The three-dimensional equations of magnetoconvection under the Boussinesq approximation, with a uniform vertical background magnetic field, are (Knobloch *et al.* 1981)

$$\begin{aligned} \frac{\partial \mathbf{u}}{\partial t} + (\mathbf{u}.\nabla)\mathbf{u} &= \sigma\nabla^2\mathbf{u} - \nabla p + \sigma R(1-(T-T_0))\mathbf{e_z} + \sigma\zeta Q(\nabla\wedge\mathbf{B})\wedge\mathbf{B} \\ \frac{\partial T}{\partial t} &= \nabla^2 T - (\mathbf{u}.\nabla)T \\ \frac{\partial \mathbf{B}}{\partial t} &= \zeta\nabla^2\mathbf{B} + \nabla\wedge(\mathbf{u}\wedge\mathbf{B}) \end{aligned} \tag{5.1}$$

where once again σ and ζ are the Prandtl and magnetic Prandtl numbers (2.19). R and Q are defined in §3.1.

As usual, take the curl of the equation of motion above to derive the vorticity equation:

$$\frac{\partial \omega}{\partial t} = \sigma \nabla^2 \omega + \sigma \zeta Q \nabla \wedge \big((\mathbf{B}.\nabla)\mathbf{B} \big) + (\omega.\nabla)\mathbf{u} - (\mathbf{u}.\nabla)\omega + \sigma R \left(\frac{\partial T}{\partial y}, -\frac{\partial T}{\partial x}, 0 \right) \tag{5.2}$$

where $\omega = \nabla \wedge \mathbf{u}$ and I have used the facts that

$$\begin{aligned} (\nabla \wedge \mathbf{B}) \wedge \mathbf{B} &= (\mathbf{B}.\nabla)\mathbf{B} - \nabla(\mathbf{B}^2) \\ \mathbf{u} \wedge (\nabla \wedge \mathbf{u}) &= -(\mathbf{u}.\nabla)\mathbf{u} \\ \nabla \wedge (\mathbf{u} \wedge \omega) &= (\omega.\nabla)\mathbf{u} - (\mathbf{u}.\nabla)\omega \end{aligned} \tag{5.3}$$

As before, all coordinates have been scaled by the depth of the box d, and time t has been scaled by the thermal conduction time d^2/κ, κ being the thermal diffusivity. Retaining the boundary conditions of §3.1, we have that

$$u_z = 0, \quad B_x = B_y = 0 \quad \text{at } z = 0,\, 1. \tag{5.4}$$

We may see that equations (5.1) have a static conducting solution satisfying

$$\mathbf{u} = \mathbf{B} = 0, \quad T = 1 - z \tag{5.5}$$

corresponding to a stationary fluid with an imposed, uniform, vertical magnetic field. As before, all quantities are constrained to be periodic in the x and y directions, with period λ.

As in Chapter 3 it is hoped to truncate each of the variables in the vertical direction. To this end, and in order to satisfy the above boundary conditions (5.4), expand each of the variables in the vertical direction as a Fourier series. Next, project onto the lowest vertical mode and truncate the series, retaining the 11 modes required for consistency:

$$\mathbf{u} = \begin{pmatrix} u_0(x,y,t) + u_1(x,y,t)\cos \pi z \\ v_0(x,y,t) + v_1(x,y,t)\cos \pi z \\ w_1(x,y,t)\sin \pi z \end{pmatrix} \tag{5.6}$$

$$\mathbf{B} = \begin{pmatrix} B_{x_1}(x,y,t)\sin \pi z \\ B_{y_1}(x,y,t)\sin \pi z \\ 1 + B_{z_0}(x,y,t) + B_{z_1}(x,y,t)\cos \pi z \end{pmatrix} \tag{5.7}$$

$$T = 1 - z + T_1(x, y, t) \sin \pi z + T_2(x, y, t) \sin 2\pi z \tag{5.8}$$

Note that in three dimensions 'mean flow' modes are required in the expansions of the horizontal velocity that were not present in our system of two spatial dimensions. Using $\omega = \nabla \wedge \mathbf{u}$ we obtain the corresponding expansion for the vorticity:

$$\omega = \begin{pmatrix} \omega_{x_1}(x, y, t) \sin \pi z \\ \omega_{y_1}(x, y, t) \sin \pi z \\ \omega_{z_0}(x, y, t) + \omega_{z_1}(x, y, t) \cos \pi z \end{pmatrix} = \begin{pmatrix} (\partial_y w_1 + \pi v_1) \sin \pi z \\ -(\partial_x w_1 + \pi u_1) \sin \pi z \\ (\partial_x v_0 - \partial_y u_0) + (\partial_x v_1 - \partial_y u_1) \cos \pi z \end{pmatrix} \tag{5.9}$$

Here ∂_x and ∂_y are the usual symbols for partial differentiation with respect to x and y. Furthermore, the fact that $\mathbf{u}$, ω, and $\mathbf{B}$ are divergence-free in our system results in the following additional conditions:

$$\partial_x u_0 + \partial_y v_0 = 0 \tag{5.10}$$

$$\partial_x u_1 + \partial_y v_1 + \pi w_1 = 0 \tag{5.11}$$

$$\partial_x \omega_{x_1} + \partial_y \omega_{y_1} - \pi \omega_{z_1} = 0 \tag{5.12}$$

$$\partial_x B_{x_1} + \partial_y B_{y_1} - \pi B_{z_1} = 0\,. \tag{5.13}$$

Now substituting (5.6)–(5.8) into (5.1)–(5.2) and projecting onto the appropriate vertical modes we obtain the partial differential equations that govern the evolution of the 10 remaining modes.

$$\begin{aligned} \frac{\partial T_1}{\partial t} &= \partial_{xx} T_1 + \partial_{yy} T_1 - \pi^2 T_1 + w_1(1 + \pi T_2) \\ &\quad - u_0 \partial_x T_1 - v_0 \partial_y T_1 - \frac{1}{2}(u_1 \partial_x T_2 + v_1 \partial_y T_2) \end{aligned} \tag{5.14}$$

$$\begin{aligned} \frac{\partial T_2}{\partial t} &= \partial_{xx} T_2 + \partial_{yy} T_2 - 4\pi^2 T_2 - \frac{\pi}{2} w_1 T_1 \\ &\quad - u_0 \partial_x T_2 - v_0 \partial_y T_2 - \frac{1}{2}(u_1 \partial_x T_1 + v_1 \partial_y T_1) \end{aligned} \tag{5.15}$$

$$\begin{aligned} \frac{\partial B_{x_1}}{\partial t} &= \zeta(\partial_{xx} B_{x_1} + \partial_{yy} B_{x_1} - \pi^2 B_{x_1}) - \pi u_1(1 + B_{z_0}) \\ &\quad + B_{x_1} \partial_x u_0 + B_{y_1} \partial_y u_0 - u_0 \partial_x B_{x_1} - v_0 \partial_y B_{x_1} \end{aligned} \tag{5.16}$$

$$\frac{\partial B_{y_1}}{\partial t} = \zeta(\partial_{xx}B_{y_1} + \partial_{yy}B_{y_1} - \pi^2 B_{y_1}) - \pi\, v_1(1+B_{z_0}) + B_{x_1}\partial_x v_0 + B_{y_1}\partial_y v_0 - u_0\partial_x B_{y_1} - v_0\partial_y B_{y_1} \tag{5.17}$$

$$\frac{\partial B_{z_1}}{\partial t} = \zeta(\partial_{xx}B_{z_1} + \partial_{yy}B_{z_1} - \pi^2 B_{z_1}) + \pi w_1(1+B_{z_0}) - u_1\partial_x B_{z_0} - v_1\partial_y B_{z_0} - u_0\partial_x B_{z_1} - v_0\partial_y B_{z_1} \tag{5.18}$$

$$\frac{\partial B_{z_0}}{\partial t} = \zeta(\partial_{xx}B_{z_0} + \partial_{yy}B_{z_0}) + \pi w_1 B_{z_1} + \frac{1}{2}(B_{x_1}\partial_x w_1 + B_{y_1}\partial_y w_1) - \frac{1}{2}(u_1\partial_x B_{z_1} + v_1\partial_y B_{z_1}) - u_0\partial_x B_{z_0} - v_0\partial_y B_{z_0} \tag{5.19}$$

$$\frac{\partial \omega_{x_1}}{\partial t} = \sigma(\partial_{xx}\omega_{x_1} + \partial_{yy}\omega_{x_1} - \pi^2\omega_{x_1}) + \sigma R\partial_y T_1 - \pi u_1\omega_{z_0} - u_0\partial_x\omega_{x_1} - v_0\partial_y\omega_{x_1} + \omega_{x_1}\partial_x u_0 + \omega_{y_1}\partial_y u_0 + \sigma\zeta Q\Big(\pi^2 B_{y_1}(1+B_{z_0}) - \pi\partial_y B_{z_1}(1+B_{z_0}) - \pi B_{z_1}\partial_y B_{z_0} + B_{x_1}\partial_{xy}B_{z_0} + B_{y_1}\partial_{yy}B_{z_0} + \partial_y B_{y_1}\partial_y B_{z_0} + \partial_y B_{x_1}\partial_x B_{z_0}\Big) \tag{5.20}$$

$$\frac{\partial \omega_{y_1}}{\partial t} = \sigma(\partial_{xx}\omega_{y_1} + \partial_{yy}\omega_{y_1} - \pi^2\omega_{y_1}) - \sigma R\partial_x T_1 - \pi v_1\omega_{z_0} - u_0\partial_x\omega_{y_1} - v_0\partial_y\omega_{y_1} + \omega_{x_1}\partial_x v_0 + \omega_{y_1}\partial_y v_0 - \sigma\zeta Q\Big(\pi^2 B_{x_1}(1+B_{z_0}) - \pi\partial_x B_{z_1}(1+B_{z_0}) - \pi B_{z_1}\partial_x B_{z_0} + B_{y_1}\partial_{xy}B_{z_0} + B_{x_1}\partial_{xx}B_{z_0} + \partial_x B_{x_1}\partial_x B_{z_0} + \partial_x B_{y_1}\partial_y B_{z_0}\Big) \tag{5.21}$$

$$\frac{\partial \omega_{z_1}}{\partial t} = \sigma(\partial_{xx}\omega_{z_1} + \partial_{yy}\omega_{z_1} - \pi^2\omega_{z_1}) + \pi w_1\omega_{z_0} - u_0\partial_x\omega_{z_1} - v_0\partial_y\omega_{z_1} - u_1\partial_x\omega_{z_0} - v_1\partial_y\omega_{z_0} + \sigma\zeta Q\pi\Big((\partial_x B_{y_1} - \partial_y B_{x_1})(1+B_{z_0}) + B_{y_1}\partial_x B_{z_0} - B_{x_1}\partial_y B_{z_0}\Big) \tag{5.22}$$

$$\begin{aligned}\frac{\partial \omega_{z_0}}{\partial t} &= \sigma(\partial_{xx}\omega_{z_0} + \partial_{yy}\omega_{z_0}) + \pi w_1 \omega_{z_1} - u_0 \partial_x \omega_{z_0} - v_0 \partial_y \omega_{z_0} \\ &\quad - \frac{1}{2}(u_1 \partial_x \omega_{z_1} + v_1 \partial_y \omega_{z_1}) + \frac{1}{2}(\omega_{x_1} \partial_x w_1 + \omega_{y_1} \partial_y w_1) \\ &\quad + \sigma\zeta Q\Big(\pi B_{z_1}(\partial_x B_{y_1} - \partial_y B_{x_1}) + \frac{1}{2}(B_{x_1}\partial_{xx}B_{y_1} + B_{y_1}\partial_{xy}B_{y_1} \\ &\quad - B_{x_1}\partial_{xy}B_{x_1} - B_{y_1}\partial_{yy}B_{x_1}) + \frac{\pi}{2}(B_{y_1}\partial_x B_{z_1} - B_{x_1}\partial_y B_{z_1})\Big)\end{aligned} \tag{5.23}$$

§5.2. *The model system*

As we saw in Chapter 3, for the case of two-dimensional Boussinesq magnetoconvection the existence and use of the stream function and the magnetic flux function ensure that both the velocity and magnetic field are solenoidal. In three dimensions these luxuries are no longer available and alternative methods must be employed.

A convenient method here owes its existence to the fact that truncating occurs in the z-direction, thus simplifying greatly the calculation of any vertical derivatives. For example if we solve (5.16) and (5.17), we may then calculate B_{z_1} by simply invoking the condition for zero divergence (5.13). This was in fact done when finding both B_{z_1} and ω_{z_1}. At a given timestep the vorticity must also be inverted to obtain the velocity. To do this employ (5.9)–(5.11) and invert using Fourier transforms. The details involve lengthy and tedious algebra and we need not include them here.

As before, in solving equations (5.14)–(5.23) I exploit the horizontal periodicity by using pseudo-spectral methods for both x- and y-derivatives, and use the same second order Adams-Bashforth scheme for timestepping.

§5.3. *Isolated States*

Convective patterns in three-dimensional magnetoconvection in the presence of an imposed vertical magnetic field have been extensively studied. In the fully compressible case two approaches have been attempted. The first, and more ambitious, models the solar atmosphere as accurately as possible, including the effects of ionization and radiative transfer (Nordlund & Stein 1989). A second approach, and the one that I have pursued in this dissertation, is to construct more idealized systems in order that the key features might be observed and analysed more readily. Three-dimensional equivalents of the principal patterns reported in Chapter 2 have been found (Weiss *et al.* 1996), and the phenomenon of flux separation that was

discovered in wide boxes and described in §2.2.3 has also been studied in 3D (Tao *et al.* 1998).

In the case of Boussinesq magnetoconvection only a few studies have been published (Cox & Matthews 1997). The truncated model described in §5.1 should be able to reproduce the vast majority of the patterns found in previous studies, and exploiting its reduced numerical complexity one could undertake a thorough investigation of parameter space. However, these are not my main concern and instead I merely aim to locate stable isolated states, and consequently tailor any numerical experiments to this goal.

In my studies of isolated states in two dimensions (Chapter 3), convective patterns that might be considered as 'fundamental' came in two main varieties. Firstly §3.6 describes the *convecton*, a single steady isolated roll, and secondly §3.9 describes an equivalent *oscillatory cell*. One might expect, therefore, that such three-dimensional states could exist either as steady or time-dependent solutions.

Although the isolated states of Chapter 3 were discovered through investigations of non-isolated states by carefully following particular solution branches, the additional computational complexity of including the third spatial dimension renders this approach impractical, even with current advances in processing speed. Moreover, one of the reasons for studying two-dimensional fluids is to gain an insight into their behaviour that should prove incisive when taking the step up to three dimensions. The presence of such isolated convective states was not predicted prior to the investigations of Chapter 3, but had it been known that they existed then locating them would have proved significantly simpler. Consequently, setting up a plausible isolated three-dimensional state to be used as the initial state for a numerical run should enable any such stable states to be conveniently located.

It is difficult to imagine an elegant three-dimensional analogue of the convecton. One fairly suggestive possibility is a toroidal convective cell, equivalent to an axisymmetric version of the two-dimensional plume seen in Figure 3-4(b). In this, hot fluid would rise (or equivalently cold fluid fall, due to standard Boussinesq point symmetry (3.25)) in the centre before moving radially outwards, meeting the wall of the region of high magnetic field strength and falling (or rising) again. A second possibility is a single roll in the form of a short horizontal tube which tapers off at either end. The fact that such a tube possesses a 'preferred direction' means that it is not simple to construct a sequence of bifurcations that might lead to such a state. Nonetheless, the possibility cannot be discounted.

As a test of the model, a two-dimensional convecton solution from Chapter 3 was extended infinitely in the y-direction to give a single tubular roll with $O(2)$

symmetry. Several tests demonstrated that my three-dimensional code correctly reproduces previously obtained two-dimensional results, and agrees with the linear theory expounded in §3.2.

§5.3.1. Preliminary Results

Following the results and conclusions of Chapter 2 and Chapter 3 numerical experiments are conducted in a box with aspect ratio $\lambda = 6$ ($\{0 \leq x \leq 6,\ 0 \leq y \leq 6,\ 0 \leq z \leq 1\}$), wide enough that isolated states should be possible. Initially, a relatively low value ($R = 5000$) for the Rayleigh number is chosen and the diffusivities (see (2.19)) are again fixed at $\sigma = 1$ and $\zeta = 0.1$. I found that a greater horizontal resolution than in two dimensions is required to resolve all structures, and so 256 modes are used in both horizontal directions.

As was observed in Chapter 3 isolated states tend to occur for Q in the neighbourhood of $Q^{(o)}_{max}$, the value of Q below which the trivial state becomes unstable. For an isolated state, the majority of the magnetic flux must be collected in a region small enough that the *effective* value of Q is greater than $Q^{(o)}_{max}$, ensuring that the region is stable to small perturbations and remains free from convection. In two dimensions, for $\lambda = 6$ and $R = 20000$ ($Q^{(o)}_{max} \approx 24000$), this meant that single convectons could be found as low with Q as low as 13600. In three spatial dimensions, however, if an analogous circular convecton were found with a characteristic width $\bar{\lambda} = 1$, the field would only be compressed into a region making up 35/36 of the box, as opposed to 5/6 of the box in two dimensions. This in turn implies that the effective field in the magnetic region would be considerably less in 3D for a given value of Q than in 2D. It is therefore natural to expect that isolated states should exist for values of Q only slightly less than $Q^{(o)}_{max}$, or in fact values of Q that are linearly subcritical ($Q > Q^{(o)}_{max}$).

For the initial case of $R = 5000$ and $\zeta = 0.1$, $Q^{(o)}_{max} = 4220$. Runs are therefore carried out first with $Q = 4200$. The run is repeated with two initial states; firstly an artificial toroidal 'plume', and secondly a short tubular roll. Both are described above. Both solutions remain in a transitory state for a considerable period before settling down to a stable state, with the toroidal run proving particularly slow, but eventually both exhibit stable solutions. The 'toroidal' case proved unable to retain its isolated nature, and eventually filled the box with irregular time-dependent convection. The 'tubular' case, however, remained in a partially isolated periodic state. The planform may be seen in Figure 5-1 and is the first time that such localized states have been observed in three dimensional convection. Here, the flow alternates in direction, whilst retaining horizontal mirror symmetry (about a plane

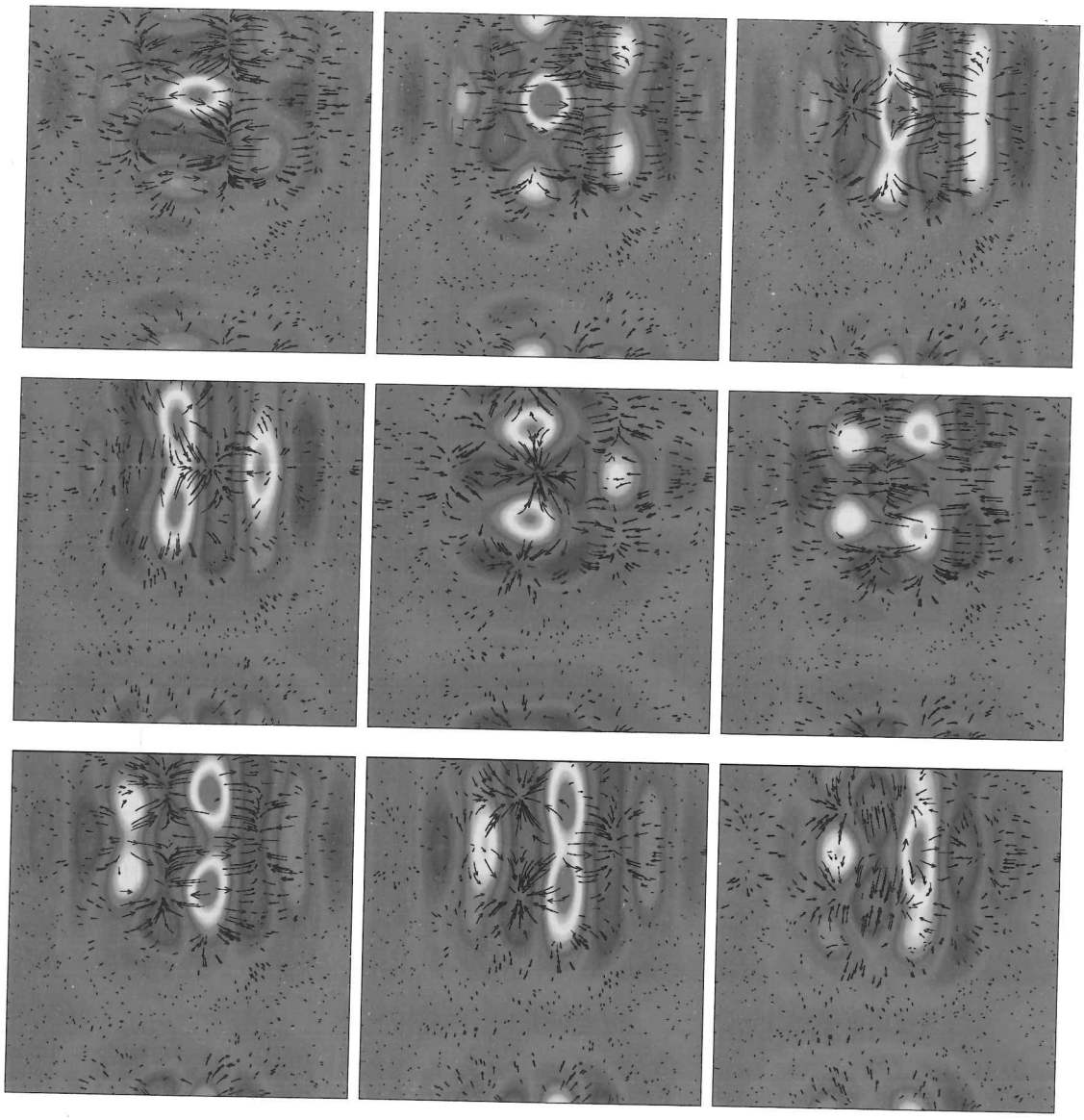

Figure 5-1. *$R = 5000$, $Q = 4200$ in a three-dimensional box $6 \times 6 \times 1$. Each image is taken after an equal time interval and shows a horizontal cross-section taken just below the surface. The shading shows temperature deviations θ and velocity arrows are superimposed. The total time that elapses is approximately one period.*

at $y \approx 4.5$), as flux collected between regions of hot upflow is suddenly squeezed out to either side, causing the upflow to occur in a perpendicular direction. Unlike in the case of convectons in two dimensions, the magnetic field strength in the convective region is only reduced to around half of its value in the surrounding magnetic region, illustrating the ability of the flux to creep back in around the sides of horizontal flows that act to expel it. It is reasonable to expect that the solution shown here has bifurcated from a qualitatively similar one in which there is D_4 spatial symmetry about an axis in the y-direction as well as the x-direction, which also has an additional temporal symmetry in which the velocity and temperature deviations are reversed after half a period has elapsed. In some ways the convective region may be considered as existing in a computational box of its own, of size $\lambda \approx 4$, and will represent a solution to a similar problem in a box of this size with rigid boundaries and greatly reduced magnetic field strength. As in two dimensions, these isolated solutions separate the computational domain into two distinct regimes and the solution in each is essentially independent of the other.

Although there is a clear and permanent region of strong magnetic field in which convection is suppressed, the flow cannot be considered to be fully isolated. Indeed the convective region has a width of around 4, and the convective region will be influenced by the periodic nature of the boundary conditions. However, (as in two dimensions) if the magnetic field strength is increased, the convective region should decrease in size accordingly. A run was therefore carried out with the same 'tubular' initial conditions for the linearly subcritical value of $Q = 4500$. The convection is again restricted to only part of the experimental domain and, as predicted, is smaller. The increased field strength has overwhelmed one of the rolls and the solution is essentially a smaller version of that seen for $Q = 4200$. Figure 5-2 shows how the flow varies over one period. The mirror symmetry in a vertical plane is again retained, and symmetry in another perpendicular vertical plane is only slightly broken. This again may be considered as a solution with rectangular D_2 symmetry that has undergone mild symmetry breaking in one axis.

Increasing the magnetic field yet further induces a more dramatic change. The size of the convective region is again reduced, and now has a width (in the x-direction) of $\bar{\lambda}_x \approx 2$. An additional symmetry breaking has occurred, and the only spatial symmetry is now the Z_2 mirror symmetry in the vertical x-z plane through the centre of the convective region. Snapshots of the solution may be seen in Figure 5-3.

Finally, increasing the magnetic field strength yet further results in the state shown in Figure 5-4. The flow has settled into a periodic solution consisting of a

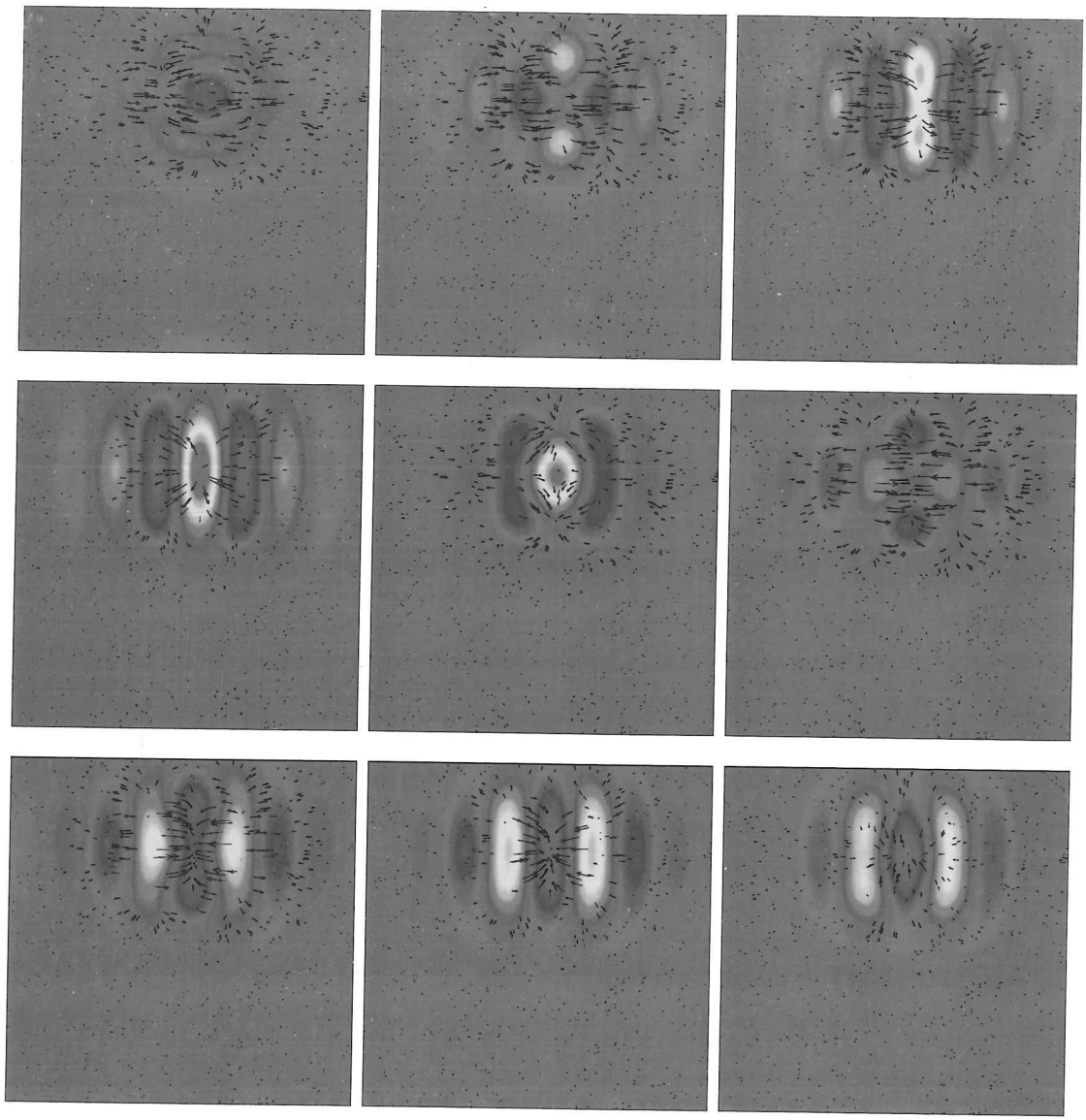

Figure 5-2. *As in Figure 5-1 but with* $Q = 4500$. *The frames again cover approximately one period.*

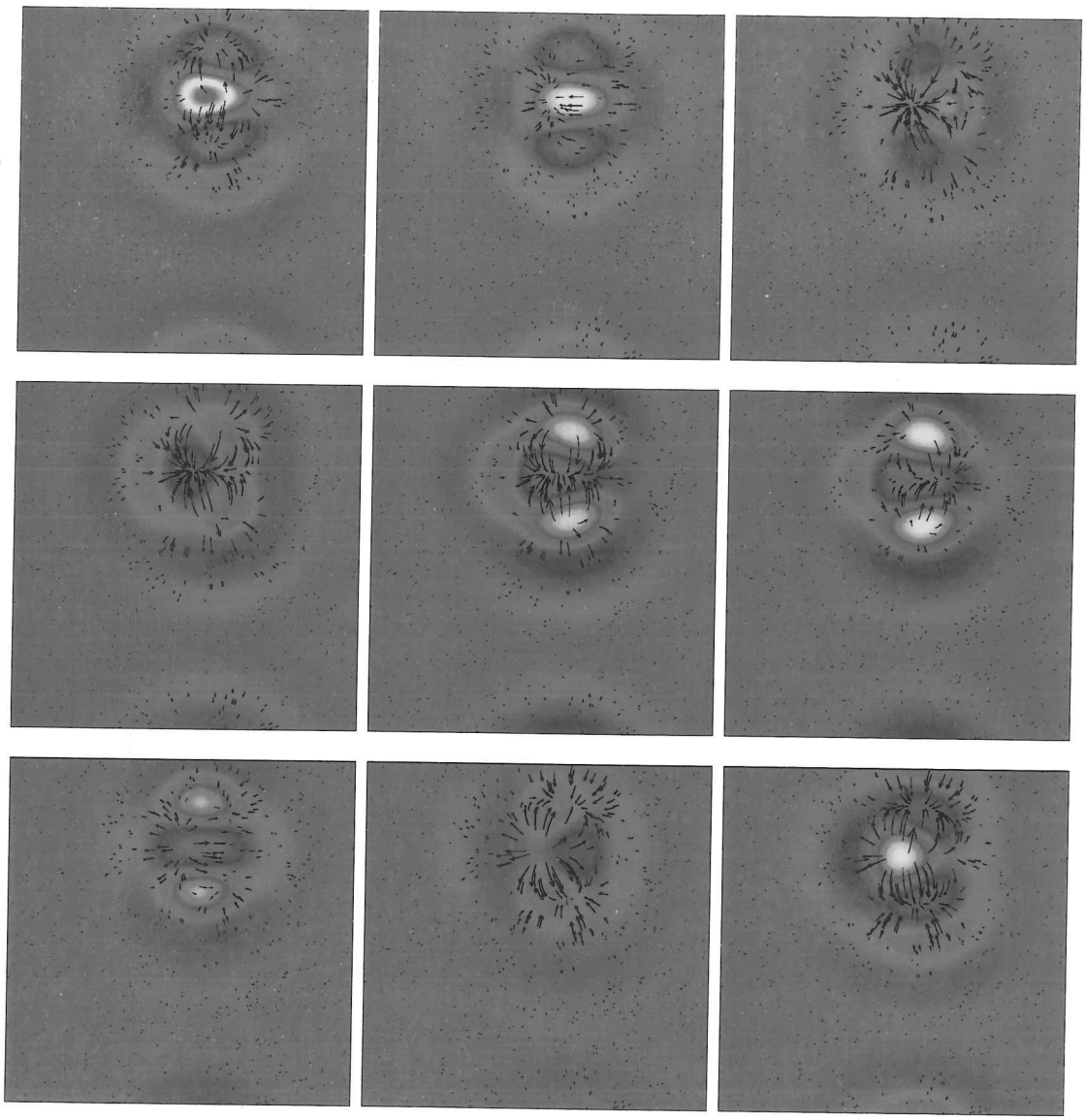

Figure 5-3. *As in Figure 5-1 but with* $Q = 5000$. *The frames again cover approximately one period.*

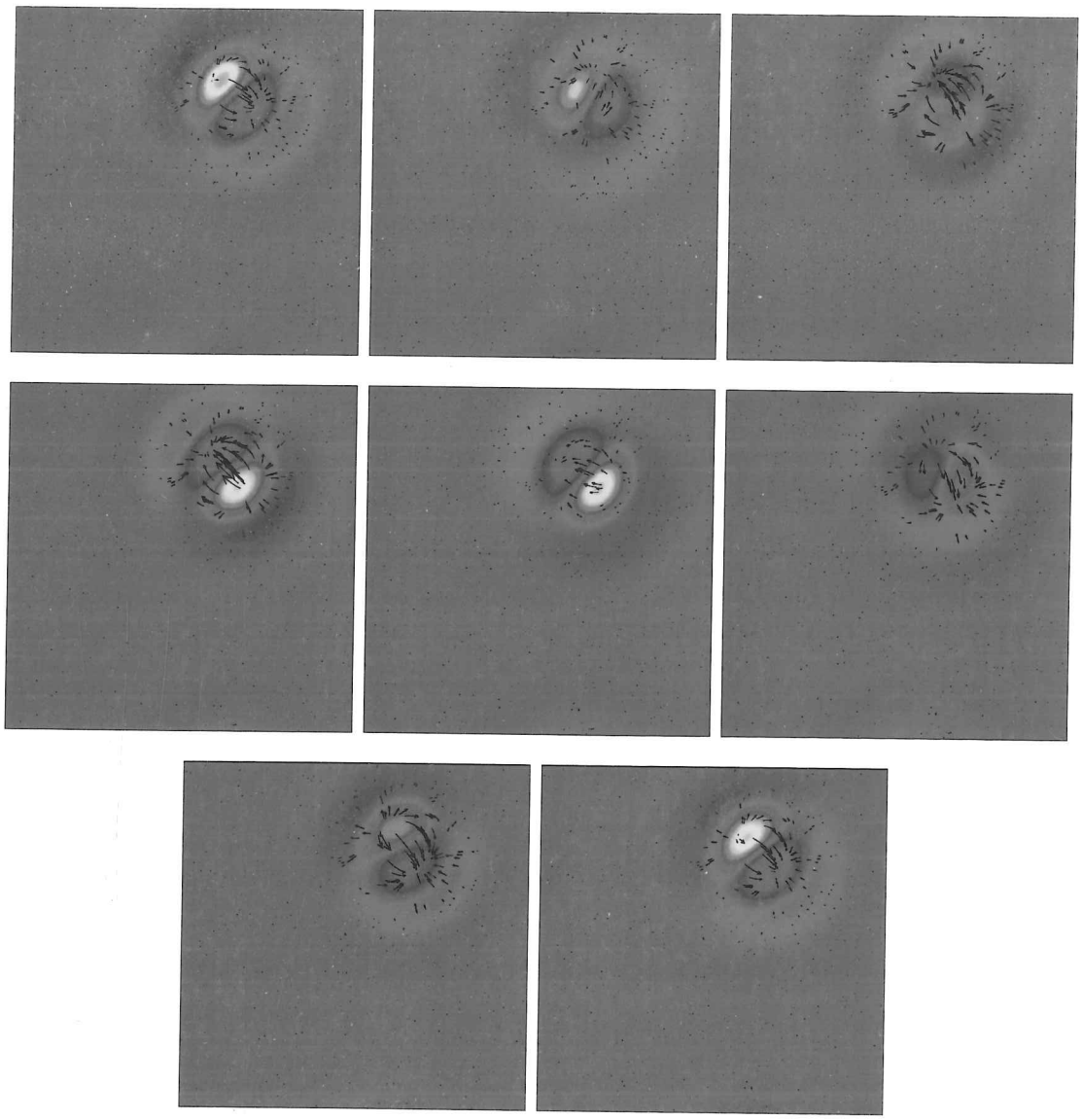

Figure 5-4. *As in Figure 5-1 but with $Q = 5500$. Here we see the fundamental 3D isolated convective cell, pulsating as it rotates. The frames again cover approximately one period.*

region of rising hot fluid which is forced horizontally in one direction upon hitting the surface, before cooling and falling once again. The convecting region is essentially a spherical version of the two-dimensional convecton that was reported in Chapter 3. However, the whole cell is also pulsating and rotating. The maximum value of the temperature rises and falls periodically, yet the rotation is not uniform: the cell pulses whilst there is almost no rotation, then the whole cell rotates through 180 degrees before the rotation almost ceases and the cell pulses once again. This may be explained by considering the effect of the magnetic field within the small convective region. The horizontal motion of the rising fluid upon hitting the surface collects any nearby magnetic field into the cooler half of the convective region. This builds up until it is strong enough to counter the motion of the horizontal flow. The magnetic field escapes, causing the cell to rotate, and momentarily fills the convective region. Hot fluid now rises in the other half of the cell and the whole process repeats. The total time elapsed in Figure 5-4 is approximately 0.15 dimensionless time units, and represents one period of the solution.

Animations of all the solutions described in this section may be downloaded for viewing using the *xanim* program from

http://www.damtp.cam.ac.uk/user/smb1001/anim3d/

This is highly recommended as an aid to clarifying exactly what is happening in Figure 5-1- Figure 5-4.

A comparison of Figure 5-4 ($Q = 5500$) and Figure 5-3 ($Q = 5000$) shows that the solution in Figure 5-3 may be considered as two copies of the convective cell in Figure 5-4 with additional mirror symmetry, just as in two dimensions Figure 3-4(c) bifurcates to leave a single convecton (Figure 3-4(d)). Similarly Figure 5-2 can be viewed as an agglomeration of four copies of the cell in Figure 5-4 with D_2 mirror symmetry, which in turn undergoes a symmetry-breaking bifurcation to produce Figure 5-3.

Further increases in Q cause the convection to be swamped by the magnetic field and the entirety of the box tends rapidly to the trivial static solution.

We may thus consider Figure 5-4 to be the three-dimensional analogue of the *convecton* described in Chapter 3, the 'fundamental' unit of convection which make up similar non-isolated states. Further images of this localized state may be seen in Figure 5-5 which show a solution that is essentially identical to Figure 5-4. Figure 5-5 shows a horizontal section very near the surface of both temperature and magnetic field, and vertical sections across the cell. From the vertical sections

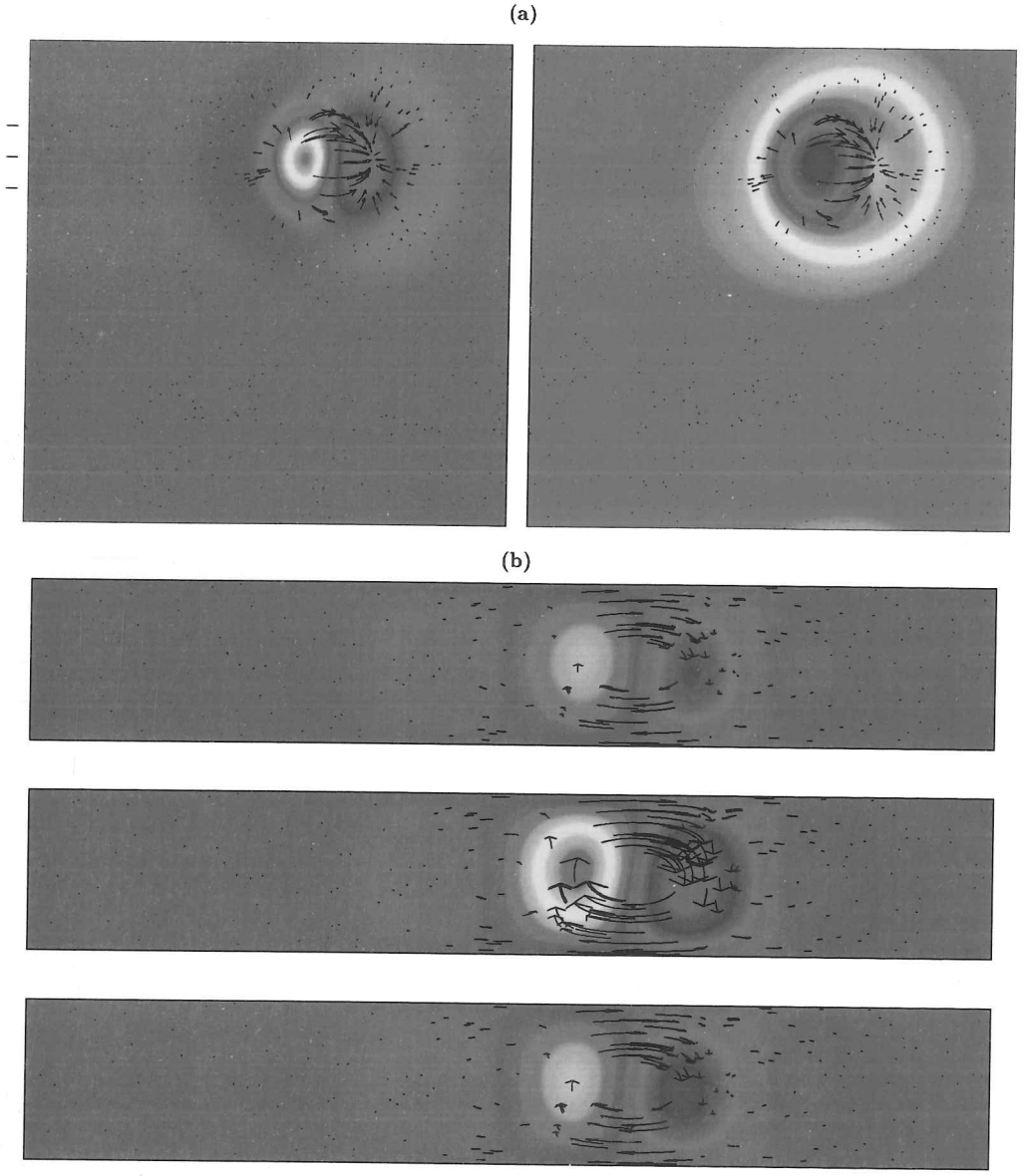

Figure 5-5. $R = 5000$, $Q = 5500$, $\lambda = 6$. *(a) a horizontal section just below the surface showing temperature (left) and magnetic field strength (right), with superimposed velocity arrows; (b) three vertical sections cutting across the isolated cell at* $y = 4.95$, 4.52 *and* 4.12. *The three dashes to the left of (a) indicate where the sections in (b) were taken.*

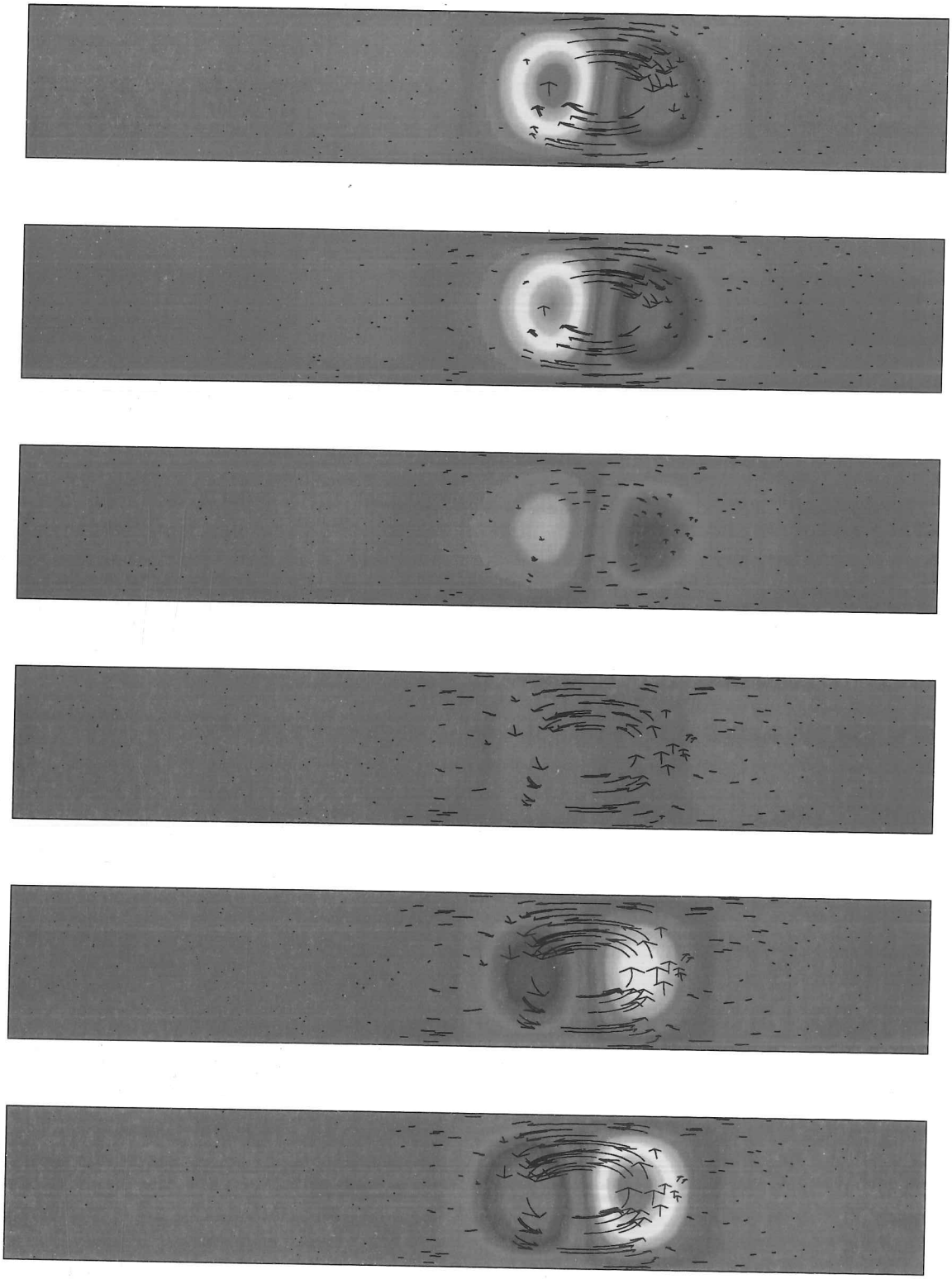

Figure 5-6. $R = 5000$, $Q = 5500$, $\lambda = 6$. *Each image shows a vertical cross-section (in the x-z plane at $y = 4.52$) taken through the centre of the isolated cell shown in Figure 5-5. The shading shows temperature deviations θ and velocity arrows are superimposed. These images were taken at equal time intervals, and the total time that elapses is approximately half a period.*

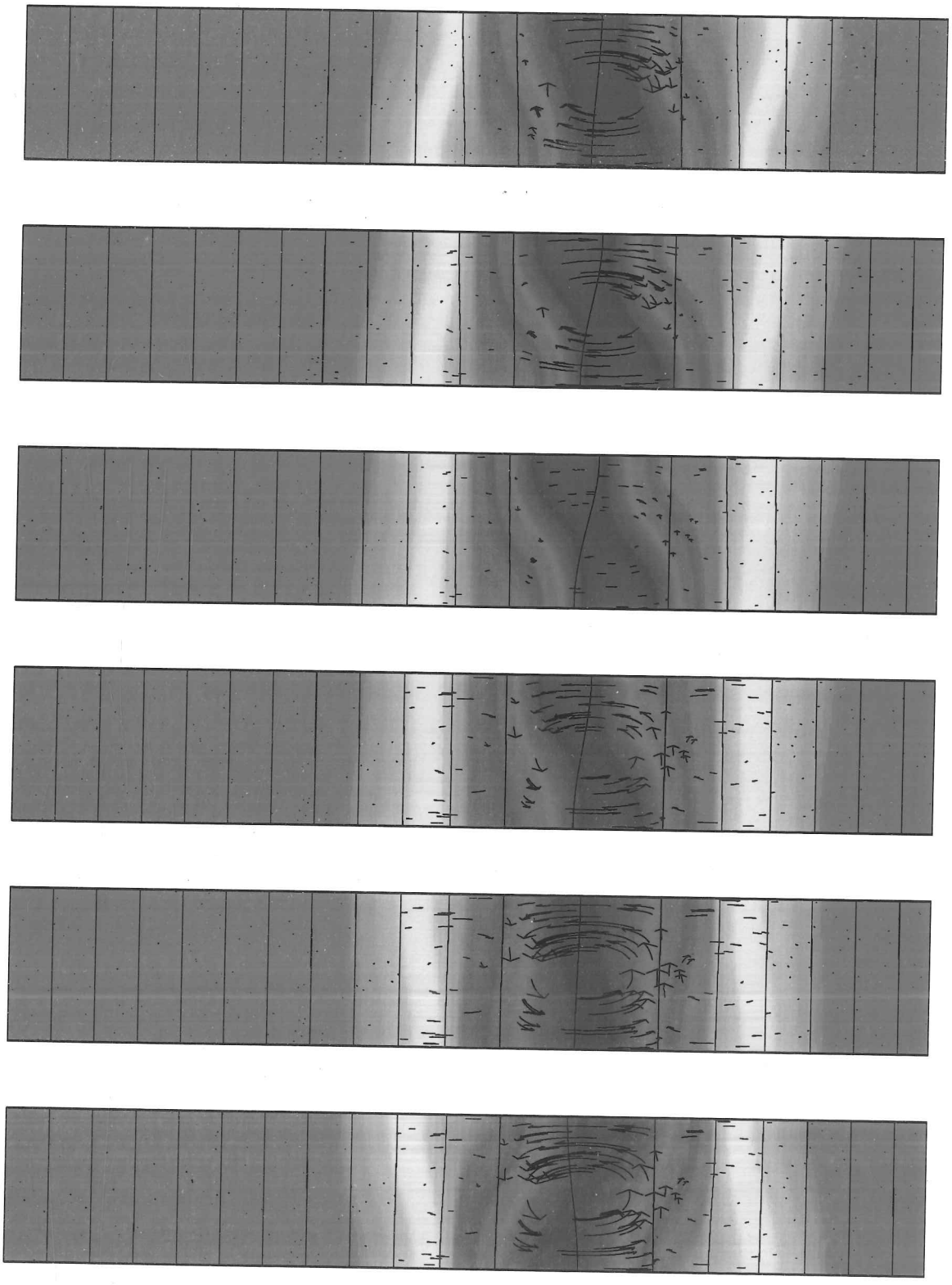

Figure 5-7. *These images represent the same events as Figure 5-6 but the shading now shows magnetic field strength, and the continuous black lines are magnetic field lines.*

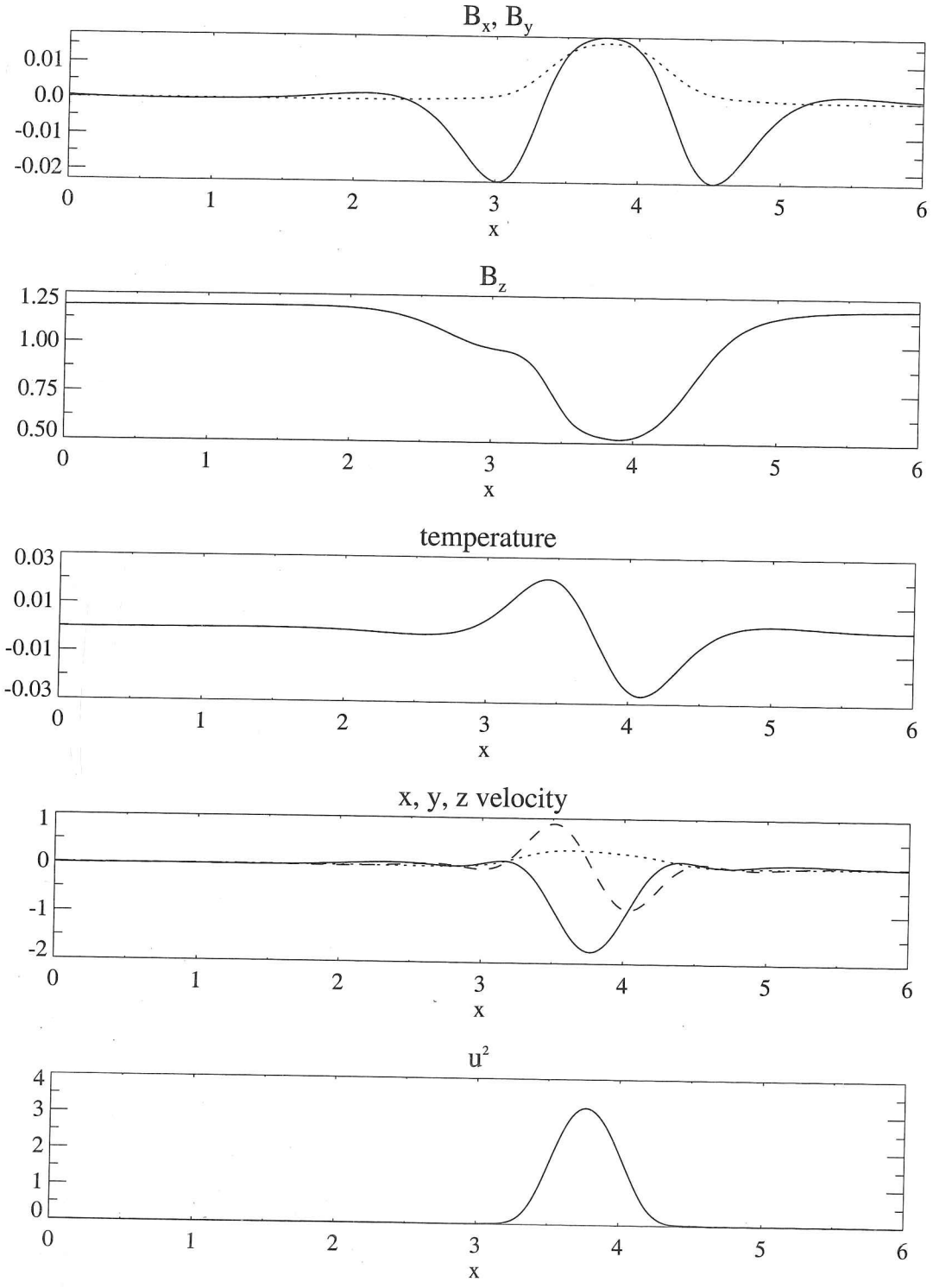

Figure 5-8. $R = 5000$, $Q = 5500$, $\lambda = 6$. *Graphs of various physical quantities as a function of x. Here $y = 4.52$ and $z = 0.875$. These values correspond to a horizontal line just below the surface and passing through the centre of the isolated state in Figure 5-6(a) (from left to right). For the velocity* $\mathbf{u}$ *and magnetic field* $\mathbf{B}$*, the x and y-components are the solid and dotted lines respectively, and for* $\mathbf{u}$ *the dashed line is the z-component.*

(Figure 5-5(b)) we can see that, in addition to the strong circular motion near the centre of the cell, there are also slender counter-cells at either edge. As regards the magnetic field, in Chapter 3 it is noted that the two-dimensional convecton is able to reduce the magnetic field strength within the convective region to around one-thousandth of its original value. In three dimensions, however, the field strength inside the isolated cell is still reduced, but only to around one fifth of the external value. This is most clearly seen in Figure 5-8 which shows how the magnetic field strength, temperature and velocity vary horizontally across the centre of the localized solution shown in Figure 5-6(a).

The discovery of such localized states provides confirmation that the two-dimensional convecton seen in §3.6 is indeed stable to three-dimensional perturbations. It seems extremely likely that many of the conclusions drawn from the studies in two dimensions will still apply here, and this suggests that the results of Chapter 3 are more robust than one might initially have thought. For example, given an arbitrarily wide box ($\lambda \gg 1$) solutions could be found in which any number of the three-dimensional isolated states described above could be found, scattered within the box as desired (*cf.* §3.5). Furthermore, §3.12 proved that the range of isolated solutions was not a result of inadequate vertical resolution, and as such I can be confident that the three-dimensional states shown here will also be found in a fully-resolved simulation. The implications of these results are far-reaching: this is the first time that any simulation has succeeded in creating solutions of this kind, and they are sure to engender a great deal of study. The work presented here is preliminary, and studies are ongoing to try to develop a more complete understanding of the origin and nature of such isolated three-dimensional states. It is a little premature to say that such states explain the phenomenon of umbral dots – the small, isolated bright features observed in the region of high magnetic field strength in the centre of sunspots – but there is certainly reason to be optimistic that a more systematic study will assist in resolving many of the unanswered questions in the area.

Chapter 6.

Concluding Remarks

What is the Sun? If the science of astronomy could solve this great problem, it would be nearly capable of solving that of the entire Universe.

Amedée Guillemin, 1870

In this dissertation I have attempted to model the many different regimes of the solar photosphere, from the kinematic domain of granulation to the magnetically dominated umbrae in the centre of sunspots. In doing so I have located many different convective patterns and have tried to indicate their possible relevance in helping to explain recent solar observations.

In Chapter 2 I investigated the case of compressible, fully-resolved convection in a two-dimensional box in the presence of an imposed vertical magnetic field. The aims of my studies were twofold. The first aim was to perform a rough parameter sweep, in order to locate the full range of dynamical behaviour that is possible under the different circumstances that may be encountered in a late-type star such as our Sun. The second aim was to investigate how robust these and many preceding results (Hurlburt & Toomre 1988; Weiss *et al.* 1990; Weiss *et al.* 1996) are to changes in the over-simplified boundary conditions that are imposed as standard.

This second motivation turned up many useful results applicable to all models of magnetoconvection. The most important of these demonstrated the significance of ensuring that the size of the computational box is appropriate to the situation under study. In §2.2 I showed that a solution obtained in a simulation will be representative of the chosen parameter values *only* if the box is sufficiently large. For the systems considered in this dissertation this corresponds to a box which is at least 6 times as wide as it is high. Other boundary conditions proved to have a less marked effect: replacing the usual magnetic boundary condition of constraining the field to be vertical at the surface with the more realistic approach of matching

it to a potential field did not change the sequence of patterns, but merely shifted the bifurcation points in parameter space. In addition it was found that if the temperature is no longer held constant at the surface and is instead matched to black-body radiation according to Stefan's Law (2.14), the solution is essentially unchanged. These results justify the use of such idealized boundary conditions and suggest that continued use will not unduly affect studies of theoretical convection.

In varying the parameters many convective patterns were discovered. Steady convection gave way to spatially modulated oscillations which in turn became irregular as the system was given more freedom (either by increasing the box size, or reducing the magnetic field strength). Finally, a new state was discovered in which the flow was able to collect the magnetic field into a single region, leaving a single large convective plume in which the field strength had effectively been reduced to zero (§2.2.3).

This unfamiliar dichotomy motivated the investigations of Chapter 3 in an attempt to understand how such a state is formed. Accordingly, a model was derived for two-dimensional Boussinesq magnetoconvection in which the equations were truncated to only one or two modes in the vertical. This simplification was crucial in allowing detailed examination of the range of available solutions, and it became possible to follow a particular solution branch in order to locate the parameter range over which it is stable. In doing so, many states were found which mirrored the behaviour of the 'flux-separated' states of Chapter 2. Of these the most fundamental was a single steady roll, isolated in a sea of high magnetic field. This 'convecton', as I have named it, represents an important new state in which a crucial symmetry-breaking has occurred, and further investigations have revealed much about its nature. For example many such convectons may occur isolated from one another and scattered across a box. Moreover, experiments conducted in the fully-resolved case proved that the results are not merely an artifice of the vertical truncation, with only the positions of the bifurcations being altered and not the order.

In Chapter 4 preliminary results were given for models in which the equations had been further simplified. This was undertaken in the hope that any similar localized solutions discovered might yield to application of the tools of modern theory of dynamical systems. The advantage here is that the behaviour of models such as the Swift-Hohenberg equation (4.25) already has an extensive literature devoted to it, and if it could be shown that the processes involved there are the same as those in magnetoconvection then many important results could be extracted.

Only after having covered the theory of convective patterns in two dimensions is it desirable to take the additional step to modelling convection in three spatial dimensions. In Chapter 5 I derived a truncated model, similar to that in Chapter 3, for the three-dimensional case, building on what was learnt from earlier investigations. Analogous localized solutions were located that may go some way towards explaining the phenomenon of umbral dots – small bright localized regions of convection seen in the region of high magnetic field strength in the centre of sunspots (Sobotka 1997). It is important to acknowledge that such isolated solutions would not have been located were it not for the studies that were first conducted in two dimensions. As in all branches of science, investigators must indeed learn to walk before they can run.

This lesson applies equally well to comparisons of our idealized models to observations of the solar photosphere: despite their limitations such investigations permit the most important features of the system to be located more easily, for the robust results to be extracted and the model-dependent behaviour rejected. As Galileo wrote in 1623:

> *Philosophy is written in this grand book – I mean the universe – which stands continuously open to our gaze, but which cannot be understood unless one first learns to understand the language in which it is written. It is written in the language of mathematics ... without which it is humanly impossible to understand a single word of it.*

The theoretical models presented here are important tools for investigating convective behaviour in the outer layers of the Sun, but give only hints as to where such behaviour may occur. For quantitative predictions we must rely on detailed simulations (Spruit 1997). As numerical techniques and computing power improve, these two approaches are gradually converging and coming closer to the reality that is revealed by observations.

Barany E., Dellnitz M. and Golubitsky M. (1993) "Detecting the symmetry of attractors." *Physica D* **67**, 66.

Bayliss A., Matkowsky B.J. and Riecke H. (1994) "Structure and dynamics of modulated traveling waves in cellular flames." *Physica D* **74**, 1.

Blanchflower S.M., Rucklidge A.M. and Weiss N.O. (1998) "Modelling photospheric magnetoconvection." *MNRAS* **301**, 593.

Blanchflower S.M. (1999) "Magnetohydrodynamic convectons." *Phys. Lett. A* **261**, 74.

Brummell N.H., Cattaneo F. and Toomre J. (1995) "Turbulent dynamics in the solar convection zone." *Science* **269**, 1370.

Brummell N.H., Hurlburt N.E. and Toomre J. (1996) "Turbulent compressible convection with rotation. 1. Flow structure and evolution." *ApJ* **473**, 494.

Busse F.H. and Clever R.M. (1981) "An asymptotic model of two-dimensional convection in the limit of low Prandtl number." *J. Fluid Mech.* **102**, 75.

Cattaneo F. (1994) "Magnetoconvection," in *Solar Magnetic Fields*, p. 261. Schüssler M., and Schmidt W. (eds.). Cambridge University Press: Cambridge.

Cattaneo F., Brummell N.H., Toomre J., Malagoli A. and Hurlburt N.E. (1991) "Turbulent compressible convection." *ApJ* **370**, 282.

Chandrasekhar S. (1961) *Hydrodynamic and Hydromagnetic Stability*. Clarendon Press: Oxford.

Cox S.M. and Matthews P.C. (1997) "A pseudospectral code for convection with an analytical/numerical implementation of horizontal boundary conditions." *Int. J. Num. Meth. in Fluids* **25**, 151.

Crawford J.D. and Knobloch E. (1991) "Symmetry and symmetry-breaking bifurcations in fluid-dynamics." *Ann. Rev. Fluid Mech.* **23**, 341.

Cross M.C. and Hohenberg P.C. (1993) "Pattern formation outside of equilibrium." *Rev. Mod. Phys.* **65**, 851.

Curry J.H., Herring J.R., Loncaric J. and Orszag S.A. (1984) "Order and disorder in two- and three-dimensional Bénard convection." *J. Fluid Mech.* **147**, 1.

Danielson R. (1964) "The structure of sunspot umbras. 1. Observations." *ApJ* **139**, 45.

Dennin M., Cannell D.S. and Ahlers G. (1998) "Patterns of electroconvection in a nematic liquid crystal." *Phys. Rev. E* **57**, 638.

Foukal P. (1990) *Solar Astrophysics*. Wiley: New York.

Galloway D.J. and Weiss N.O. (1981) "Convection and magnetic fields in stars." *ApJ* **243**, 945.

Groisman A. and Steinberg V. (1997) "Solitary vortex pairs in viscoelastic Couette flow." *Phys. Rev. Lett.* **78**, 1460.

Hurlburt N.E., Proctor M.R.E., Weiss N.O. and Brownjohn D.P. (1989) "Nonlinear compressible magnetoconvection. Part 1. Travelling waves and oscillations." *J. Fluid Mech.* **207**, 587.

Hurlburt N.E. and Toomre J. (1988) "Magnetic fields interacting with nonlinear compressible convection." *ApJ* **327**, 920.

Hurlburt N.E., Toomre J. and Massaguer, J.M. (1984) "Two-dimensional compressible convection extending over multiple scale heights." *ApJ* **282**, 557.

Cattaneo F. (1984) "Compressible magnetoconvection." University of Cambridge, Ph.D. thesis.

Jones C.A., Roberts P.H. and Galloway D.J. (1990) "Compressible convection in the presence of rotation and a magnetic field." *GAFD* **53**, 145.

Knobloch E. and Proctor M.R.E. (1981) "Nonlinear periodic convection in double-diffusive systems." *J. Fluid Mech.* **108**, 291.

Knobloch E., Weiss N.O. and da Costa L.N. (1981) "Oscillatory and steady convection in a magnetic field." *J. Fluid Mech.* **113**, 153.

Lites B.W., Bida T.A., Johanneson A. and Scharmer G.B. (1991) "High-resolution spectra of solar magnetic features. 2. Magnetic fields of umbral brightenings." *ApJ* **373**, 683.

Lorenz E.N. (1963) "Deterministic nonperiodic flow." *J. Atm. Sci.* **20**, 130.

Manneville P. (1990) *Dissipative Structures and Weak Turbulence.* Perspectives in Physics: San Diego.

Matthews P.C. (1999) "Asymptotic solutions for nonlinear magnetoconvection." *J. Fluid Mech.* **387**, 397.

Matthews P.C., Proctor M.R.E., Rucklidge A.M. and Weiss N.O. (1993) "Pulsating waves in nonlinear magnetoconvection." *Phys. Lett. A* **183**, 69.

Matthews P.C., Proctor M.R.E. and Weiss N.O. (1995) "Compressible magnetoconvection in three dimensions: planforms and nonlinear behaviour." *J. Fluid Mech.* **305**, 281.

Mollenauer L.F., Stolen R.H. and Gordon J.P. (1980) "Experimental observation of picosecond pulse narrowing and solitons in optical fibers." *Phys. Rev. Lett* **45**, 1095.

Moore D.R. and Weiss N.O. (1973) "Two-dimensional Rayleigh-Bénard convection." *J. Fluid Mech.* **58**, 289.

Muller R. (1994) "Properties of small magnetic elements," in *Solar Surface Magnetism*, p. 55. Rutten R.J. and Schrijver C.J. (eds.). Kluwer: Dordrecht.

Niemela J.J., Ahlers G. and Cannell D.S. (1991) "Localized traveling-wave states in binary-fluid convection." *Phys. Rev. Lett* **64**, 1365.

Nordlund Å. (1984) "Magnetoconvection: The interaction of convection and small scale magnetic fields," in *The Hydromagnetics of the Sun.*, p. 37. Guyenne T.D. (eds.). ESA SP–220: Noordwijk.

Nordlund Å. (1985) "The dynamics of granulation and its interaction with the radiation field," in *Theoretical Problems in High Resolution Solar Physics*, p. 1. Schmidt H.U. (eds.). Max Planck Inst. Astrophys. MPA 212: Garching.

Nordlund Å. and Stein R.F. (1989) "Simulating Magnetoconvection," in *Solar and Stellar Granulation*, p. 453. Rutten R.J. and Severino G. (eds.). Kluwer: Dordrecht.

Or-Guil M., Bode M., Schenk C.P. and Purwins H.-G. (1998) "Spot bifurcations in three-component reaction-diffusion systems: The onset of propagation." *Phys. Rev. E* **57**, 6432.

Ponty Y., Passot T. and Sulem P.L. (1997) "Pattern dynamics in rotating convection at finite Prandtl number." *Phys. Rev. E* **56**, 4162.

Proctor M.R.E. and Weiss N.O. (1982) "Magnetoconvection." *Rep. Prog. Phys.* **45**, 1317.

Proctor M.R.E. and Weiss N.O. (1990) "Normal forms and chaos in thermosolutal convection." *Nonlinearity* **3**, 619.

Proctor M.R.E., Weiss N.O., Brownjohn D.P. and Hurlburt N.E. (1994) "Nonlinear compressible magnetoconvection. Part 2. Streaming instabilities in two dimensions." *J. Fluid Mech.* **280**, 227.

Rast, M.P. (1995) "On the nature of 'exploding' granules and granule fragmentation." *ApJ* **443**, 863.

Rast, M.P., Nordlund, Å., Stein R.F. and Toomre, J. (1993) "Ionization effects in 3-dimensional solar granulation simulations." *ApJ* **408**, L53.

Riecke H. (1998) "Localized structures in pattern-forming systems," in *Pattern Formation in Continuous and Coupled Systems*, p. . M. Golubitsky, D. Luss and S. Strogatz (eds.). IMA: .

Riecke H. and Granzow G.D. (1998) "Localization of waves without bistability: worms in nematic electroconvection." *Phys. Rev. Lett* **81**, 333.

Rimmele T.R. (1997) "Evidence for magnetoconvection in a sunspot light bridge." *ApJ* **490**, 458.

Rotermund H.H., Jakubith S., von Oertzen A. and Ertl G. (1991) "Solitons in a surface reaction." *Phys. Rev. Lett* **66**, 3083.

Rucklidge A.M. (1991) "Chaos in models of double convection." University of Cambridge, Ph.D. thesis.

Rucklidge A.M., Schmidt H.U. and Weiss N.O. (1995) "The abrupt development of penumbrae in sunspots." *MNRAS* **273**, 491.

Sakaguchi H. and Brand H.R. (1996) "Stable localized solutions of arbitrary length for the quintic Swift-Hohenberg equation." *Physica D* **97**, 274.

Sakaguchi H. and Brand H.R. (1997) "Stable localized squares in pattern-forming nonequilibrium systems." *Europhys. Lett* **38**, 341.

Sakaguchi H. and Brand H.R. (1998) "Localized patterns for the quintic complex Swift-Hohenberg equation." *Physica D* **117**, 95.

Sobotka M. (1997) "Sunspots seen at high spatial resolution," in *Advances in the Physics of Sunspots*, p. 155. Schmieder B., del Toro Iniesta J.C. and Vázquez M. (eds.). P.A.S.P. Conference Series: San Francisco.

Sobotka M., Bonet J.A., Vázquez M. and Hanslmeier A. (1995) "On the dynamics of bright features in sunspot umbrae." *ApJ* **447**, L133.

Sobotka M., Brandt P.N. and Simon G.W. (1997) "Fine structure in sunspots. I. Sizes and lifetimes of umbral dots." *A&A* **328**, 682.

Sobotka M., Brandt P.N. and Simon G.W. (1997) "Fine structure in sunspots. II. Intensity variations and proper motions of umbral dots." *A&A* **328**, 689.

Spruit H.C. (1997) "Convection in stellar envelopes: a changing paradigm." *Mem. Soc. Astron. It.* **68**, 397.

Spruit H.C., Nordlund Å. and Title A.M. (1990) "Solar convection." *Ann. Rev. Astr. Ap.* **28**, 263.

Stanchfield D.C.H., Thomas J.H. and Lites B.W. (1997) "The vector magnetic field, Evershed flow, and intensity in a sunspot." *ApJ* **477**, 485.

Steffen M., Ludwig H.-G and Krüss A. (1989) "A numerical simulation study of solar granular convection in cells of different horizontal dimension." *A&A* **213**, 371.

Steiner O., Grossman-Doerth U., Knölker M. and Schüssler M. (1996) "Polarized radiation diagnostics of magnetohydrodynamic models of the solar atmosphere." *Solar Phys.* **164**, 223.

Steiner O., Grossman-Doerth U., Knölker M. and Schüssler M. (1998) "Dynamical interaction of solar magnetic elements and granular convection: Results of a numerical simulation." *ApJ* **495**, 468.

Stewartson K. and Stuart J.T. (1971) "A nonlinear instability theory for a wave system in plane Poiseuille flow." *J. Fluid Mech.* **48**, 529.

Swift J. and Hohenberg P.C. (1977) "Hydrodynamic fluctuations at the convective instability." *Phys. Rev. A* **15**, 319.

Tao L., Weiss N.O., Brownjohn D.P. and Proctor M.R.E. (1998) "Flux separation in stellar magnetoconvection." *ApJ* **496**, L39.

Thual O. and Fauve S. (1988) "Localized structures generated by subcritical instabilities." *J. Phys. France* **49**, 1829.

Umbanhowar P.B., Melo F. and Swinney H.L. (1996) "Localized excitations in a vertically vibrated granular layer." *Nature* **382**, 793.

Umemura A. and Busse F.H. (1989) "Axisymmetric convection at large Rayleigh and infinite Prandtl number." *J. Fluid Mech.* **208**, 459.

Veronis G. (1959) "Cellular convection with finite amplitude in a rotating field." *J. Fluid Mech.* **5**, 401.

Veronis G. (1965) "On finite amplitude instability in thermohaline convection." *J. Marine Res.* **23**, 1.

Veronis G. (1966) "Motions at subcritical values of the Rayleigh number in a rotating fluid." *J. Fluid Mech.* **26**, 49.

Weiss N.O. (1966) "The expulsion of magnetic flux by eddies." *Proc. Roy. Soc. A* **293**, 310.

Weiss N.O. (1981) "Convection in an imposed magnetic field. Part 2. The dynamical regime." *J. Fluid Mech.* **108**, 273.

Weiss N.O., Brownjohn D.P., Hurlburt N.E. and Proctor M.R.E. (1990) "Oscillatory convection in sunspot umbrae." *MNRAS* **245**, 434.

Weiss N.O., Brownjohn D.P., Matthews P.C. and Proctor M.R.E. (1996) "Photospheric convection in strong magnetic fields." *MNRAS* **283**, 1153.

Wilson O.C. (1978) "Chromospheric variations in Main-Sequence stars." *ApJ* **226**, 379.